Jon Kristian Voster

Experimental and Numerical Investigations of Hydrodynamic Loads on Perforated Plates Subjected to Irregular Forced Oscillations

Master's thesis in Marine Technology

Supervisor: Trygve Kristiansen

July 2020

Master's thesis

NTNU
Norwegian University of Science and Technology
Faculty of Engineering
Department of Marine Technology

NTNU
Norwegian University of
Science and Technology

Jon Kristian Voster

Experimental and Numerical Investigations of Hydrodynamic Loads on Perforated Plates Subjected to Irregular Forced Oscillations

Master's thesis in Marine Technology
Supervisor: Trygve Kristiansen
July 2020

Norwegian University of Science and Technology
Faculty of Engineering
Department of Marine Technology

NTNU
Norwegian University of
Science and Technology

Abstract

Experimental and numerical studies were done on two models. The models were perforated plates with different perforation ratios. They were subjected to regular, bi-chromatic, and irregular motions deeply submerged in water.

Regular forced oscillations were done to establish KC (Keulegan–Carpenter number) dependent curves for the hydrodynamic added mass and damping for both models. A laminar 2D viscous flow solver developed by Mentzoni (2020) was used to validate the lab results for one model. The calculations and the experiments were in close agreement. The hydrodynamic coefficients were found to have a strong dependence on the KC number for both models. This agrees well with previous results by Mentzoni (2020) and Molin (2011). The third harmonic force was also investigated. It was found that in the KC range of 0.2 and 3, the Morison load model should be used with caution. For small KC numbers, a large part of the third-harmonics was in phase with the acceleration. The semi-analytical method by Mentzoni and Kristiansen (2019) for perforated plates was compared to the experiments, and there was found good agreement for the damping for both models in the KC range of 0.2 and 2. The added mass was underestimated by the semi-analytical method for both models. The tested plates have a higher thickness than the plates the semi-analytical method is based on, which is a possible explanation of the differences.

Bi-chromatic time series were tested in order to provide data for the irregular tests. There was a strong dependency for the damping on the KC number for the previous half-cycle and the KC number of the present half-cycle. The damping was higher if the previous half-cycle had a larger amplitude of motion than the half-cycle under consideration. The damping was smaller if the previous half-cycle had a smaller amplitude than the present half-cycle. There was no particular pattern for the added mass, but the added mass from the bi-chromatic tests was scattered lower or close to the regular tests' added mass curve.

The data from the bi-chromatic forced oscillations were used to calculate the forces from time series with irregular motions generated by a Pierson-Moskowitz spectrum. There was close agreement between the calculated and measured forces from the experiments, which confirms that bi-chromatic tests are appropriate for providing hydrodynamic coefficients for irregular time series. Since the damping coefficient depends on the KC number of the present and the previous half-cycle, a simple rule is proposed, which makes it possible to use the coefficients provided by the semi-analytical method by Mentzoni and Kristiansen (2019). By using the semi-analytical method, the measured and calculated force were in close agreement when the force is dominated by damping. Based on these results, Equation 9.43 in the book "Sea Loads on Ships and Offshore Structures" by Faltinsen (1990), is proposed to be used in irregular seas with KC dependent coefficients from the semi-analytic method when the forces are dominated by damping. However, this equation should be tested with experiments, as the interaction effect of waves and motions in irregular seas is not investigated in this thesis.

Sammendrag

Eksperimentelle og numeriske studier er utført på to modeller. Modellene er perforerte plater med ulike perforeringsgrader. De ble utsatt for tvungne svingninger, både regulære, bikromatiske og irregulære. De tvungne svingningene ble utført når modellene var dypt neddykket.

Regulære tvungne svingninger ble gjort for å etablere KC-avhengige (Keulegan Carpenter tall) kurver for hydrodynamisk tilleggsmasse og demping, for begge modellene. En numerisk løser, utviklet av Mentzoni (2020), ble brukt til å validere labresultatene. Numeriske og eksperimentelle resultater stemmer godt overens. De hydrodynamiske koeffisientene ble funnet å ha en klar avhengighet av KC-tallet for begge modellene. Dette stemmer overens med tidligere resultater av Mentzoni (2020) og Molin (2011). De tredjeharmoniske kreftene ble også undersøkt. Det ble funnet at for KC-tall mellom 0.2 og 3 så må Morisons lastmodell bli brukt med forsiktighet. For små KC-tall er en stor del av de tredjeharmoniske kreftene i fase med akselerasjonen. Den semianalytiske metoden av Mentzoni og Kristiansen (2019) for perforerte plater ble sammenlignet med resultater fra eksperimentene. Det ble funnet god overenstemmelse for dempingskraften for begge modellene for KC-tall mellom 0.2 og 2. Den hydrodynamiske tilleggsmassen ble underestimert for begge modellene ved bruk av den semianalytiske metoden. Platene som ble brukt i eksperimentene har en større tykkelse enn platene som den semianalytiske metoden er basert på, noe som kan være en forklaring på forskjellene i tilleggsmassen.

Bikromatiske tidsserier ble benyttet i eksperimentene for å samle data som kan bli brukt til de irregulære tidsseriene. Det var en klar sammenheng mellom KC-tallet for den forrige og nåværende halvsyklusen for dempingen. Dempingen var høy om den forrige halvsyklusen hadde en amplitude som er større enn den nåværende amplituden. Demping var lav om amplituden til den forrige halvsyklusen var lavere enn den nåværende. Det ble ikke funnet noe spesielt mønster for tilleggsmassen, men tilleggsmassen var fordelt lavere eller nært kurven for regulære tvungne svingninger.

Dataene fra de bikromatisk tvungne bevegelsene ble brukt til å regne ut kreftene i irregulære tidsserier generert fra et Pierson-Moskowitz spektrum. Det ble funnet god overensstemmelse mellom de utregnede kreftene og de målte kreftene, noe som bekrefter at bikromatiske tidsserier egner seg godt til å gi hydrodynamiske koeffisienter for irregulære tidsserier. Siden dempingen er avhengig av både KC-tallet til den forrige og den nåværende halvsyklusen, er en enkel regel foreslått slik at det er mulig å bruke de hydrodynamiske koeffisientene fra den semianalytiske metoden av Mentzoni og Kristiansen (2019). Ved å benytte den semianalytiske metoden var de utregnede kreftene i god overenstemmelse med de målte, så lenge kreftene er dominert av dempingskrefter. Ligning 9.43 i boken "Sea Loads on Ships and Offshore Structures" av Faltinsen (1990), er foreslått til å bli brukt sammen med KC avhengige koeffisienter, til å regne ut kreftene i irregulær sjø i kombinasjon med tvungne svingninger. Siden interaksjonseffektene mellom tvungne svingninger og bølger ikke er studert i denne oppgaven bør denne ligningen bli testet ved hjelp av fremtidige eksperimenter.

Acknowledgments

There are many people that deserve sincere thanks regarding this thesis. First of all, I want to thank my supervisor, Professor Trygve Kristiansen, for excellent guidance throughout the semester. It has not been a few questions and emails he has answered. Even though the state of the current time made it impossible to have ordinary meetings, Trygve provided excellent guidance throughout the semester. Trond Innset and Ole Erik Vinje made the new model, and they were always helpful if help was needed in the lab. Torgeir Wahl was especially important in making measurements of the lab experiments as precise as possible. Whenever the measurement program, the test rig or whatever stopped working, Torgeir was there within a blink of an eye helping us. A special thanks goes to Fredrik Mentzoni, which let me use the numerical solver that he developed during his doctoral dissertation. The use of computational fluid dynamics in this thesis would not have been possible without his help. There were some long hours in the lab. Luckily fellow students, Karoline Vottestad and Marius Robsahm, did experiments in Ladertanken as well. The lab experience would certainly not have been the same without their company.

I will also use this chance to thank my family and friends for all their love and support.

Jon Kristian, July 2020

Contents

Nomenclature

$\ddot{\eta}$	Vertical acceleration
$\dot{\eta}$	Vertical velocity
$\dot{u}$	Horizontal water particle velocity
$\dot{w}$	Vertical water particle velocity
η	Vertical motion
η_a	Vertical motion amplitude
η_s	Significant vertical motion amplitude in irregular time series
$\eta_{a,i}$	Vertical motion amplitude for half-cycle "i"
λ	Wavelength
ν	Kinematic viscosity
ω	Oscillation frequency
ω_i	Oscillation frequency for half-cycle "i"
ϕ	Velocity potential
ρ	Fluid density
τ	Perforation ratio
A	Added mass
A_0	Reference added mass, $\frac{1}{4}\pi\rho D^2 L$
B	Damping
B_w	Wave-radiation damping
C_A	Added mass coefficient, $\frac{A}{A_0}$
C_D	Drag coefficient (Quadratic damping)
$C_{A,i}$	Added mass coefficient for half-cycle "i"
$C_{B,i}$	Damping coefficient for half-cycle "i"
C_B	Damping coefficient, $\frac{A}{\omega A_0}$
D	Plate width
h	Water depth
KC	Keulegan–Carpenter number
KC_i	Keulegan–Carpenter number for half-cycle "i"

KC_s	Significant Keulegan–Carpenter number in irregular time series
L	Plate length
T	Oscillation period
t	Time
T_i	Oscillation period for half-cycle "i"
CFD	Computational fluid dynamics
CFL	Courant–Friedrichs–Lewy condition

1 Introduction

1.1 Motivation

The installation of subsea structures is an essential part of oilfield development. These structures are often complex and consist of cylinders, plates, perforated structures, tubes, and cables. Calculating the hydrodynamic force acting on the structure during the installation is a complicated task, and often conservative approaches are needed to guarantee safe operations. There are two reasons for investigating the hydrodynamic forces.

- Reduce cost for the installation
- Increase the operability of subsea fields

If a conservative approach is used to determine the hydrodynamic forces, the weather window of operability will be narrower than needed, and the construction vessel will be waiting for a weather window longer than needed. A construction vessel is expensive to operate, and it has a high day rate. If the hydrodynamic forces are calculated more accurately, the operational limit can be increased, so the waiting on weather will decrease. This will save money, and the operations can be performed more effectively.

If the operational limit can be increased, it will also allow the service companies to perform the operations in a larger part of the year. Today, many operations need to be done in the summer months due to that the weather is calmer in this part of the year. The ultimate goal is to reach all-year operability of marine operations for subsea fields, and one part in reaching this goal is to understand the hydrodynamic loads in waves and forces motions.

Mentzoni (2020) divides the lifting operation into five stages when installing a subsea structure on the seabed.

1. The structure is lifted from the deck and positioned over the side of the vessel.
2. The structure is lifted through the sea surface. It experiences water-entry and water-exit loads as it goes in and out of waves.
3. The structure is fully submerged, but close to the free surface. The free surface affects the loads on the structure.
4. The structure is far away from the free surface. The free surface does not affect the loads on the structure, but it experiences loads from the waves and hydrodynamic loads caused by the crane´s motion.
5. The structure is close to the seabed, and the proximity from the seabed becomes important for the hydrodynamic loads.

This thesis focuses on stage 4 when the free surface is far away and can be neglected. The focus has been on forced oscillations of perforated plates. Mentzoni, Abrahamsen-Prsic and Kristiansen (2018) found that for a simplified structure consisting of two parallel latedperforated plates with cylinders in between, the hydrodynamic forces were dominated by the perforated plates. Thus, understanding the hydrodynamic loads on perforated structures is an important step towards understanding more complex subsea structures and also subsea structures like hatch covers and mud mats that are perforated structures.

This thesis is a part of one of the projects of MOVE (Marine Operations in Virtual Environments) that focuses on loads of subsea structures during lifting operations. Fellow students Karoline Vottestad and Marius Robsahm also contributed to the project. Vottestad did experimental studies of perforated plates near the free surface in regular waves and forced regular oscillations without waves. Robsahm did experimental studies on cylinders and perforated plates in the water entry phase in waves. Together, this thesis and the theses of Vottestad and Robsahm deal with stages 2-4 of the lifting operation.

1.2 Previous Work

There is done much work on hydrodynamic loads on perforated plates. Molin (2011) summarizes the work he has done regarding hydrodynamic loads on perforated structures. He uses potential flow theory and applies a quadratic pressure drop boundary condition instead of the impermeable boundary condition as for a solid plate. He finds that the added mass and damping are amplitude-dependent and dependent on the porous KC_{por} number which is

$$KC_{por} = \frac{(1-\tau)\eta_a}{\mu\tau^2 D}, \tag{1.1}$$

where μ is the discharge coefficient.

The equation for the pressure drop is

$$\Delta p = \frac{(1-\tau)\eta_a}{2\mu\tau^2} v_r|v_r|. \tag{1.2}$$

The discharge coefficient is given by

$$\mu = \frac{1-\tau}{K\tau^2}, \tag{1.3}$$

K is the resistance coefficient

$$K = \frac{2\Delta p}{\rho v^2} = \frac{2\rho h_L}{v^2}, \tag{1.4}$$

were h_L is the head loss through the orifice. Said with other words, Molin's results say how much of the flow that flows around the plate compared to what flows through the

perforations. Consequently, the added mass goes to the solid plate added mass, and the damping goes towards zero as KC goes to infinity. As Molin pointed out himself in this paper, the physical validity of these results is questionable when flow separation at the plate edges becomes important. However, these formulas serve as an important contribution in understanding the perforations' effects on the added mass and damping.

Sandvik et al. (2006) proposed a drag correction term to correct the damping in Molin's method inspired by the results for the drag coefficient by Graham (1980). For solid flat plates, Graham found by analytical work that the drag coefficient was proportional to $KC^{-1/3}$ for low KC numbers. The drag term is expressed as

$$F_{sandvik} = \frac{1}{2}\rho\alpha KC^{-1/3} D w_r |w_r|. \tag{1.5}$$

Here, w_r is the mean relative velocity through the plate, and α is an unknown constant but depends on the degree to which the flow is separated.

Molin (2011) used $\alpha = 6$ with good agreement to experimental data on a circular perforated disk. Mentzoni and Kristiansen (2019) points on the difficulties of choosing α. The α that is best for the added mass coefficient is not necessarily the best fit for the damping coefficient. They propose a new semi-analytic method were both the added mass, and the damping coefficient are based on the analytical calculations for solid plates by Graham (1980). They found constants for thin perforated plated by a 2D laminar viscous flow solver. This method represents the state of the art method to determine the forces in planar oscillatory flow for perforated plates. It is described briefly in Section 2.2.3.

Ikeda et al. (1988) did experimental studies of a cylinder and a normal flat plate subjected to regular and bi-chromatic forced oscillations. In regular oscillations, they identified an increase in the added mass in the second half-cycle when the oscillations started from rest. This increase becomes significant for $KC > 11$. For $KC = 18$, the added mass increased by a factor of almost two compared to the steady-state added mass for the same time series. They identified this as a start-up phenomenon. The conclusions that can be drawn from their results for the normal flat plate for the bi-chromatic tests are

- The damping was larger than the damping in the regular steady-state forced oscillations when the amplitude of the previous half-cycle was larger than the present.
- The damping was smaller than the damping in the regular steady-state forced oscillations when the amplitude of the previous half-cycle was smaller than the present.
- The damping was smaller in a start-up situation compared to the damping in regular steady-state forced oscillations.
- The added mass was larger in a start-up situation than the added mass in regular steady-state forced oscillations.
- The effect of the start-up on the added mass was largest for $KC = 18$, that is when the forces are dominated by damping.

- The added mass was close to or lower than the added mass in regular steady-state forced oscillations if the previous amplitude was either larger or smaller than the present. The exception was for half-cycles close to a start-up situation, where the added mass was larger than the added mass in regular steady-state forced oscillations.

If we use the coefficients from this paper for the steady-state case for $KC = 18$, the total force amplitude is 0.93 for a start-up situation, even if the added mass is almost twice the steady-state added mass. This is because the drag term is only is 0.8 of the steady-state value. In other words, the start-up effect can be neglected for plates based on these experiments.

Graham (1980) argues that the forces on sharp-edged cylinders for small KC numbers should be written as

$$F = A_0\ddot{\eta} + F_{vortex}. \tag{1.6}$$

The vortex force F_{vortex} can then be decomposed into components that are in phase with the acceleration and the velocity, as Mentzoni and Kristiansen (2019) did in their semi-analytical method.

Graham (1980) presents the drag force and one component of the added mass as a vortex force. The vortex force can be decomposed into two parts, where one is in phase with the acceleration and the other is in phase with the velocity. The start-up effect represent a phase-shift in the vortex force toward the acceleration in the start-up situation. However, the total force amplitude is smaller than the steady-state case for the KC numbers investigated by Ikeda et al. (1988) for a solid plate. Strictly speaking, Equation 1.6 is not valid for KC numbers higher than approximately 3-5 (Mentzoni, 2020) as the plate end vortices start to interact with each other for larger KC numbers. However, Graham's plate model is valuable in getting insight into how the plate end vortices affect the added mass and damping terms, even for higher KC numbers.

In our experiments, a KC range between 0.2 and 3 is investigated. However, there was seen a start-up effect in our experiments as well, and an increase of 25 % in the added mass was seen. Experiments performed through this thesis indicated that the start-up effect appears for smaller KC numbers than for solid plates, and CFD calculations also confirmed this. However, it was shown in Section 6.4.2 with a time series, and in Section 6.4 by plotting the non-dimensional force amplitude, that if a phase-shift in the calculated force is accepted, the start-up effect could be neglected as the force amplitude does not increase because the damping decreases. This was also valid when the added mass force and the damping force are of similar magnitudes because the damping is smaller in a start-up situation.

The simplified analysis in the recommended practice of DNV-GL (DNV-GL, 2017), recommends calculating the added mass as

$$\frac{A}{A_0} = 0.7 + 0.3\cos\left(\pi\left(\frac{\tau - 0.05}{0.34}\right)\right) \tag{1.7}$$

for perforation ratios $0.05 < \tau < 0.34$.

This yields A/A_0 as 0.78 and 0.54 for model S19 and S28, respectively. From the results in Section 6.1, this is conservative for the smallest KC that is tested. For $KC = 3$, the values from the experiment are close to the added mass from DNV-GL for both plates. Mentzoni (2020) found that for a large range of perforation ratios and KC numbers, the hydrodynamic forces are completely dominated by damping. DNV-GL recommends using $C_D > 2.5$ as a general rule for the simplified analysis for typical offshore structures. If we use the data from Table 2.1 from the semi-analytic method by Mentzoni and Kristiansen (2019) we can find the drag coefficient as

$$C_D = b_1 KC^{-1/3}. \tag{1.8}$$

For a plate with perforation ratio $\tau = 0.2$, we have from the semi-analytical method that $C_D = 6.1$ for KC=2. In the recommended practice, DNV-GL specifies that the drag coefficient is dependent on KC, but they have no recommendation on how to choose this based on the KC number for porous structures in the simplified analysis. Therefore the results on perforated plates by Mentzoni and Kristiansen (2019) closes the gap and provides a simple method for estimating the drag coefficient for perforated plates. In the recommended practice by DNV-GL, they specify that if snap loads in the hoisting wire are likely to occur from the simplified analysis, model tests or CFD calculations should be performed in order to get a better estimation of the hydrodynamic loads. The results from Mentzoni (2020) and Mentzoni and Kristiansen (2019) provides more accurate coefficients for simple calculations, and thus model tests and CFD calculation can, in many situations, be avoided.

1.3 Scope and Thesis Structure

The current thesis aims to investigate the hydrodynamic loads on perforated plates in regular and irregular forced oscillations. The hope before the lab experiments was to find a method to calculate the time series more accurately. Today's methods of calculating time series in irregular seas use constant coefficients, but as mentioned in Section 1.2, the coefficients are strongly dependent on the KC number. The aim was to study irregular time series for perforated plates and to find a method of choosing the added mass and damping coefficient in order to be able to calculate a force time series that agrees with experimental results.

In order to study irregular time series, bi-chromatic motions were used to study the effects the previous half-cycles have on the present half-cycle for the hydrodynamic coefficients. Bi-chromatic motions can be expressed as

$$\eta = z_1 \sin\omega_1 t + z_2 \sin\omega_2 t, \tag{1.9}$$

were z_1 and z_2 are constants. This family of motions is well suited to study the hydrodynamic coefficients, as the pattern will repeat after one beating period. Thus, averages for the hydrodynamic coefficients for each unique half-cycle can be found.

Also, numerical investigations were done for one of the models by the use of CFD. This was done mainly in order to strengthen the validity of the lab-results. Mentzoni (2020) found that 2D laminar CFD codes were well suited to simulate the flow of perforated plates for the KC range of the present experiments. By the use of CFD, some effects in the lab, such as the free-surface effects or the assumption that the forces from the empty rig can be subtracted, can be isolated out. This is because the CFD calculations are done in infinite fluid, and there is no rig that may interfere with the model. Thus, some of the lab's biased error sources can be removed, and the simplifications of the flow that is done in the CFD calculations are likely to be valid if the results agree. CFD calculations and lab results complement each other.

In this thesis, first some important hydrodynamic coefficients and parameters are presented together with different load models. Then, the experimental setup and method are presented. The numerical solver is explained briefly in Section 5. Also, thin vortex sheet theory is explained, which is needed to understand the main characteristics of the flow. The results for the regular oscillations is presented together with the CFD calculations in Section 6.1. Subsequently, results for the bi-chromatic tests are presented and discussed in Section 6.4. Ultimately in Section 7 the knowledge gained from the bi-chromatic time series is applied on two irregular time series. The recently developed semi-analytic method by Mentzoni and Kristiansen (2019) is used to calculate the hydrodynamic forces, and the calculated forces are compared to the experiment. It was found close agreement between these two when the forces are dominated by damping. Because of this close agreement, an equation from Faltinsen (1990) is adapted to take in KC dependent coefficients from the semi-analytic method for damping dominated forces.

The model with the lowest perforation ratio (S19) was made in conjunction with this thesis. Thus, a new model is compared to the semi-analytic method. This model showed close agreement for the damping for $KC < 2$, while the added mass was somewhat underpredicted due to the thickness of the present model.

2 Theory

2.1 Parameters and Coefficients

There are several parameters which are of importance for perforated plates in oscillatory flow. The perforation ratio τ is defined as the plate's ventilated area divided by the total area of the plate. That is

$$\tau = \frac{A_{vent}}{DL}. \tag{2.1}$$

D is the plate width, and L is the plate length, and A_{vent} is the ventilated area of the plate.

Keulegan and Carpenter (1958) defined a parameter which is later called the KC number. This number is important in oscillatory flow, as it contains information on the formed vortices in the wake relative to the size of the body. The KC number can be expressed as

$$KC = \frac{2\pi\eta_a}{D}, \tag{2.2}$$

were η_a is the amplitude of motion.

Relative surface roughness (Sarpkaya, 1976b) and Reynolds number can influence the hydrodynamic coefficients in oscillatory flow, especially for circular cylinders where the separation points are not fixed. The Reynolds number is

$$Re = \frac{ul}{\nu} \tag{2.3}$$

Were u and l are characteristic velocity and length, respectively, and ν is the kinematic viscosity. The Reynolds number contains information of the inertia in the fluid relative to the viscous forces.

Sarpkaya (1976) uses a parameter he calls β and is defined as $\beta = Re/KC$. However, the KC number must be specified in addition to the β parameter. Thus, the β parameter could easily be replaced by the Reynolds number (Faltinsen, 1990). In this thesis, the surfaces on the model are considered smooth, and the separation points are fixed due to sharp corners, such that the influence of Reynolds number and relative surface roughness is not waited to play a major role.

However, there is still necessary to do large scale tests on perforated structures in oscillatory flow to investigate the influence of massive changes in the Reynolds number for perforated plates.

2.2 Load Models

The force can be decomposed into an inertia term proportional to the acceleratiion, and a damping term that is proportional to the velocity as

$$F = -A\ddot{\eta} - B\dot{\eta}. \tag{2.4}$$

If the plate oscillates harmonically as

$$\eta = \eta_a \cos(\omega t), \tag{2.5}$$

the force can be written as

$$\frac{F}{\omega^2 A_0 \eta_a} = \frac{A}{A_0} cos(\omega t) + \frac{B}{\omega A_0} \sin(\omega t). \tag{2.6}$$

A_0 is the reference added mass for a solid flat plate and is

$$A_0 = \frac{\pi}{4}\rho D^2 L, \tag{2.7}$$

where the length is L, width is D, and ρ is the water density. The amplitude of the force can be written as

$$F_a = A_0\omega^2\eta_a\sqrt{\left(\frac{A}{A_0}\right)^2 + \left(\frac{B}{A_0\omega}\right)^2} = A_0\omega^2\eta_a\sqrt{C_A^2 + C_B^2}, \tag{2.8}$$

for a harmonically oscillating plate in an otherwise still fluid. The normalized added mass coefficient is

$$C_A = \frac{A}{A_0} \tag{2.9}$$

and the normalized damping coefficient is

$$C_B = \frac{B}{A_0\omega}. \tag{2.10}$$

For bi-chromatic motions, the force amplitude for half-cycle "i" is approximated by a harmonic equivalent motion, with period and amplitude as defined in Section 4.2. By doing this, we can write the force amplitude for a half-cycle as

$$F_{a,i} = A_0\omega_i^2\eta_{a,i}\sqrt{\left(\frac{A_i}{A_0}\right)^2 + \left(\frac{B_i}{A_0\omega}\right)^2}. \tag{2.11}$$

Since the vortex formation is a quadratic process in the velocity, as shown in Section 5.2.2, it is not possible to decompose the force contribution from each term in the bi-chromatic motion by the superposition principle. Thus, this approximation of the half cycles must be made in order to normalize the force coefficients and force amplitude from the bi-chromatic motions.

2.2.1 Morrison's Equation

Morison et al. (1950) came up with a load model for surface piercing vertical piles in waves. They found that for high KC numbers, the fraction of third harmonic forces was approximately -0.2 of the first harmonic force in phase with the velocity. This means that the third harmonics can be included in a simple equation with a quadratic drag term. The equation they came up with for a surface piecing pile is

$$\frac{dF_x}{dz} = C_m A_0 \dot{u} + \frac{1}{2} C_D \rho D u|u|, \tag{2.12}$$

where A_0 is the potential flow added mass, D the characteristic length, $C_m = (1 + C_A)$, and u the water particle velocity in the x-direction.

For a plate subjected to forced oscillations in an otherwise still fluid, the force becomes

$$F = C_A A_0 \ddot{\eta} + \frac{1}{2} C_D \rho D L \dot{\eta}|\dot{\eta}| \tag{2.13}$$

for a quadratic damping load model. Singh (1979) discusses the load model of Equation 2.13, and argues that it becomes questionable for KC numbers lower than 20. This is because a major contribution to the third harmonics for low KC numbers may come from the vortices that are swept back over the body when the flow is returned. Consequently, the third harmonic does not have to be in phase with the velocity.

2.2.2 Graham's Load Model for Solid Plates at Low KC Numbers

Graham (1980) suggests that the forces on sharp-edged bodies for small KC numbers should be written as

$$F = A_0 \ddot{\eta} + F_v, \tag{2.14}$$

were F_v is a vortex force. Graham then derives the vortex force analytically for a flat plate as

$$Fv = b_v K C^{-1/3} \dot{\eta}_a^2 \psi(t/T) \tag{2.15}$$

The function $\psi(t/T)$ contains the time dependence and a phase shift relative to the velocity. $\dot{\eta}_a$ is the velocity amplitude. The coefficient b_v must be computed or found by experiments. The vortex force can then decomposed by Fourier analysis into a damping term and an inertia term as

$$Fv = A_0 \left(a_1 KC^{2/3} \ddot{\eta} + \frac{b_1}{\pi^2} KC^{2/3} \dot{\eta} \right) \tag{2.16}$$

If a quadratic damping term as in Equation 2.12 is wanted the vortex force can be written as

$$Fv = A_0 a_1 KC^{2/3} \ddot{\eta} + \frac{1}{2} \rho b_1 DLKC^{-1/3} \dot{\eta} |\dot{\eta}|. \tag{2.17}$$

2.2.3 Mentzoni and Kristiansen's Semi-Analytical Method for Perforated Plates

Mentzoni and Kristiansen (2019) utilizes Graham's findings for solid plates and adapts the method for perforated plates. They write the force on the perforated plate as

$$F = A_0(a_0 + a_1 KC^{2/3})\ddot{\eta} + A_0 \omega \frac{b_1}{\pi^2} KC^{2/3} \dot{\eta} \tag{2.18}$$

By curve fitting results from CFD they find a_0, a_1 and b_1 for thin plates as a function of the perforation ratio. Their results are found in Table 2.1 were the coefficients are based on calculations for $0.24 < KC < 2.2$. The plates were thin with sharp-edged openings. Mentzoni and Kristiansen (2020) did experiments of a plate consisting of a row of circular cylinders. He found that the damping and the added mass was lower compared to a plate consisting of square cylinders. This is consistent with the theory of Molin (2011), which says that an increase in the discharge coefficient is equivalent to an increase in the perforation ratio. The circular cylinders are letting more water flow through the plate than square cylinders because there are more losses in the flow through the plate openings if the openings are sharp-edged. Mentzoni also points on the difference in the zero amplitude added mass for circular cylinders and square cylinders as one reason for different added mass for these plates.

Table 2.1: Coefficient used in the semi-analytical method by Mentzoni. Source: (Mentzoni and Kristiansen, 2019a)

τ	a_0	a_1	b_1
0.05	0.748	0.230	10.1
0.10	0.498	0.252	9.58
0.15	0.281	0.271	8.72
0.20	0.132	0.261	7.67
0.25	0.055	0.222	6.57
0.30	0.017	0.181	5.48
0.35	0.000	0.156	4.44
0.40	0.000	0.120	3.49
0.45	0.000	0.087	2.69
0.50	0.000	0.057	2.04

Thus the non-dimensional added mass and damping coefficients are found as

$$C_A = a_0 + a_1 KC^{2/3} \tag{2.19}$$

and

$$C_B = \frac{b_1}{\pi^2} KC^{2/3} \tag{2.20}$$

with a_0, a_1 and b_1 from Table 2.1.

2.3 Load Calculations for Marine Operations

For marine operations, the force impulse for a half-cycle is the most important parameter. It is the response of the structure from the hydrodynamic forces that is the important parameter in a lifting operation. In high seas, the crane tip will move relative to the subsea structure due to the inertia of the structure and the hydrodynamic loads acting on the structure. The impulse from the inertia force of the structure and the hydrodynamic added mass and damping forces determine the stresses in the hoisting wire. Also, slack in the hoisting wire can occur if the sum of the inertia from the structure's mass and the hydrodynamic forces are large.

Section 6.3 shows that the third-harmonic force contribution was not calculated correctly by using a quadratic damping term. A significant portion of the third harmonics is in phase with the acceleration. Figure 4.2 shows an example of the third harmonic force. The contribution to the total impulse from the third harmonic force is small compared to the first harmonic force for one half-cycle. Because of this, the forces in this thesis are calculated with a linear damping term as

$$F = -C_a A_0 \ddot{\eta} - C_b A_0 \omega \dot{\eta}. \tag{2.21}$$

In this thesis, when it is referred to hydrodynamic force coefficients or just hydrodynamic coefficients, it is the normalized added mass and damping coefficients from Equation 2.9 and Equation 2.10 that are meant.

3 Experimental Investigations

3.1 Facilities and Experimental Setup

The experimental tests are conducted in a wave flume at the Marine Technology Center at the Norwegian University Of Science and Technology. The tank is called Ladertanken in Norwegian. Mentzoni (2020) developed an experimental setup for conducting forced oscillation tests on plates in still fluid in conjunction with his doctoral thesis. The main dimensions of the wave flume can be seen Figure 3.1. The model is placed in the middle between the bottom of the wave flume and the free surface, i.e., 50 cm above the tank bottom. Figure 3.1 and Figure 3.2 shows the test rig. There were mounted three accelerometers in order to be able to measure the accelerations in all axis. The velocity and position were found by integration of the acceleration signal. A potentiometer was used to measure the position in the vertical direction, as redundancy for the accelerometer in the vertical direction. A force transducer measured the forces. Wave probes were placed in the flume as shown in Figure 3.1 in order to be able to investigate the free surface effects because there was generated some surface waves when the plate was forced to oscillate. Figure 3.3 is included to show how the wave probes are mounted in the flume. All sensors were calibrated with linear curves and checked every lab day. The force transducer was checked with a known weight, and the wave probes were checked by moving them up and down in known positions. The water temperature varied by some degrees while conducting the experiments. The variation was in the order of 2-3 ^oC with an average of approximately 20^{o}C. The water level also varied with around +- 2 cm on a day to day basis. The average was approximately 1 meter from the tank bottom. The temperature change and water level change affected the wave probes, and thus they were calibrated every lab day. They were also checked in between each new set of tests. Since pressure forces completely dominate the forces, i.e., high Reynolds number flow, the change in viscosity due to the temperate change is not expected to affect the hydrodynamic forces on the model. The density is not changed significantly with these small changes in temperature.

Catman Easy by HBM is used for data acquisition. All tests were sampled at 200 Hz, were the sampled data are filtered by Butterworth filtering at 20 Hz.

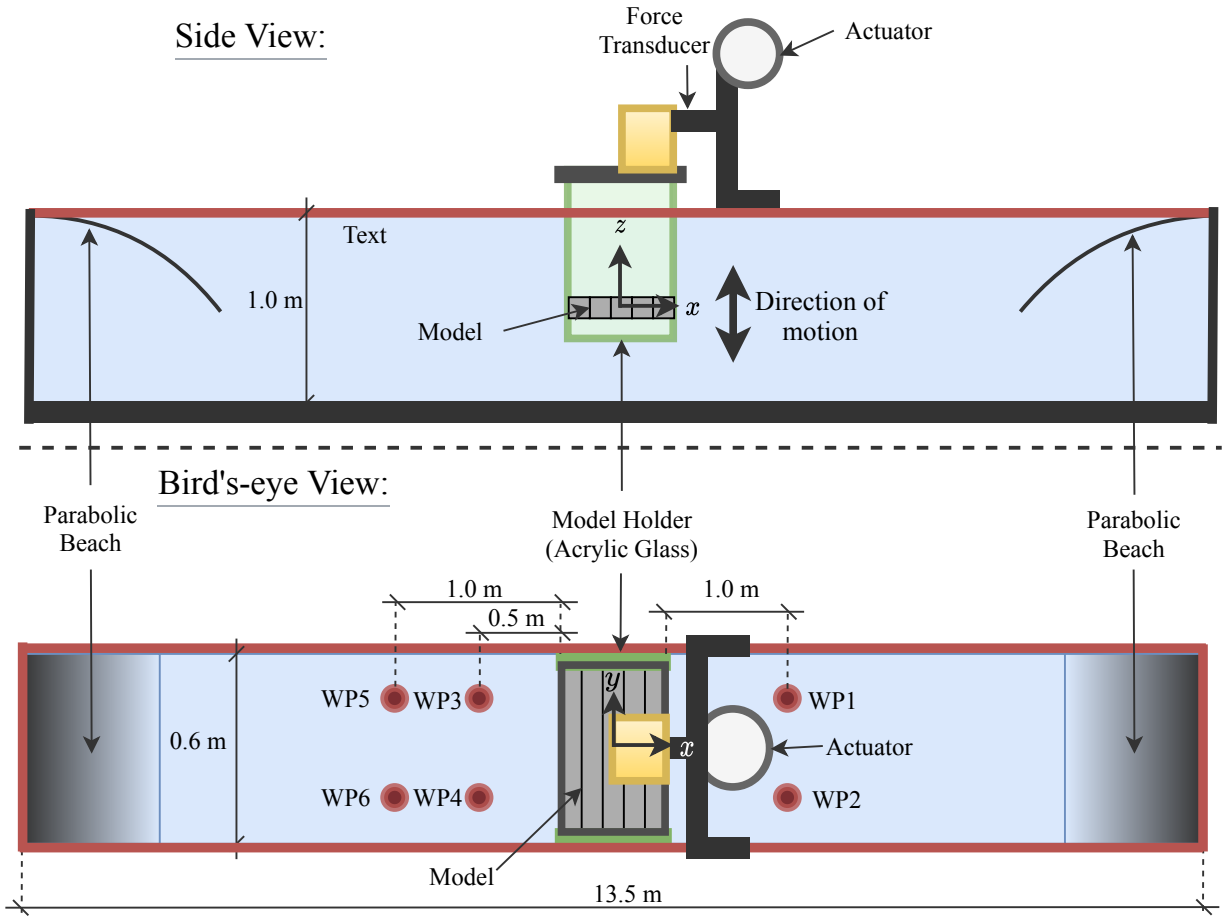

Figure 3.1: The figure shows the test rig in Ladertanken. It also presents the flume's dimensions, the parabolic beaches, and the position of the wave probes (WP1-WP6). The water depth is 1 meter, and the model is placed 0.5 meters over the tank bottom, which is in the middle between the free surface and the tank bottom. The force transducer connects the yellow wooden box and the acrylic glass plate assembly to the rest of the rig where an actuator is placed. A screw connects the actuator with the force transducer. When the force transducer moves the assembly of the yellow wooden box, acrylic glass plates and the model will move, which is how the model is forced to oscillate. Accelerometers are placed at the wooden box that provides position data.

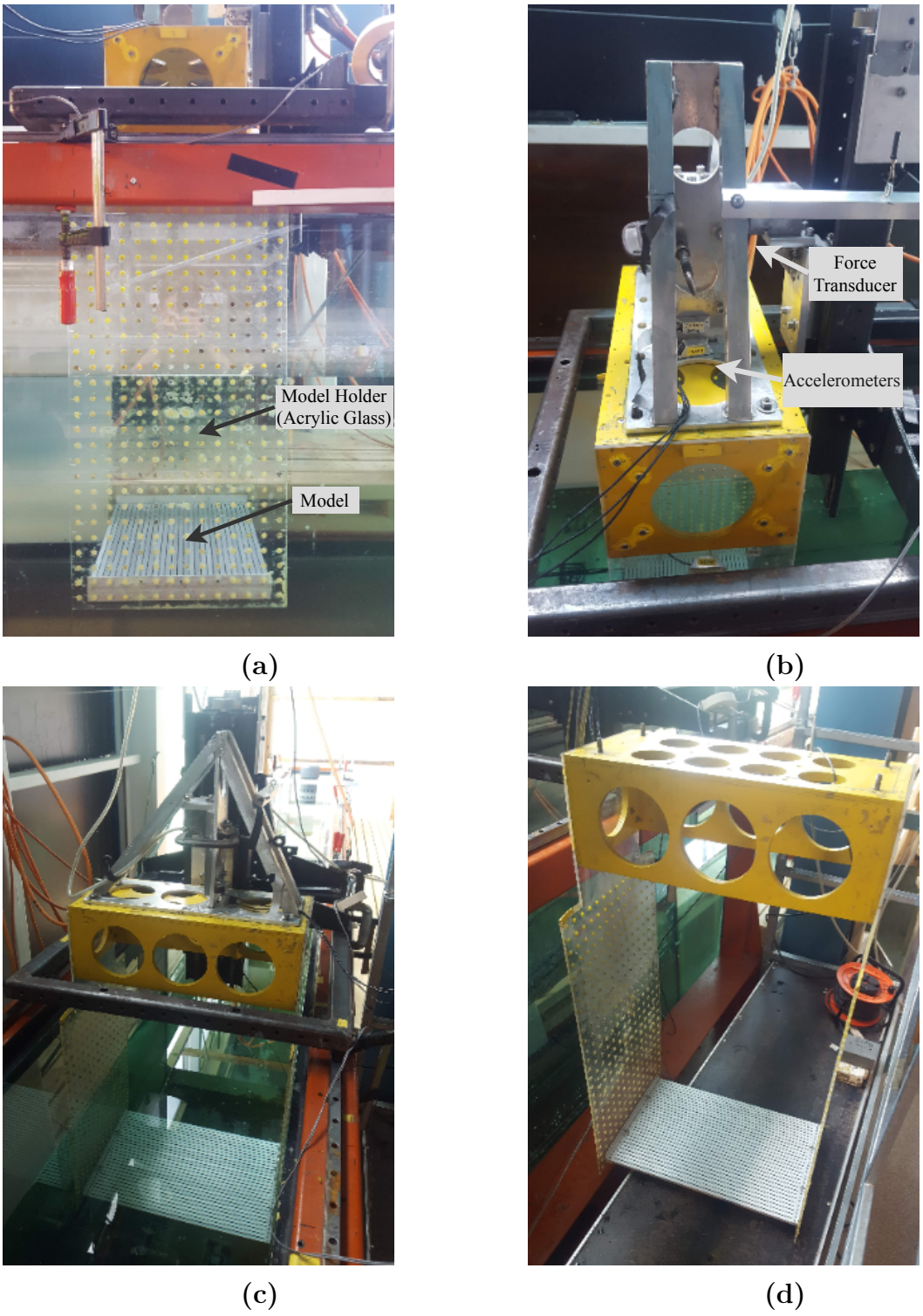

Figure 3.2: ((a) Side view of the model in the flume fastened between the acrylic glass plates. (b) A closer view at where the yellow wooden box is fastened to the rest of the rig via the force transducer. The figure also shows the accelerometers. (c) Perspective view at the complete test rig ready for a new test run. (d) The wooden box and the acrylic glass plate assembly with the model fastened between the acrylic glass plates outside the tank. The assembly must be taken outside the tank whenever the model is to be changed. The screw holes in the acrylic glass plate are filled with yellow putty in order to ensure smoother surfaces.

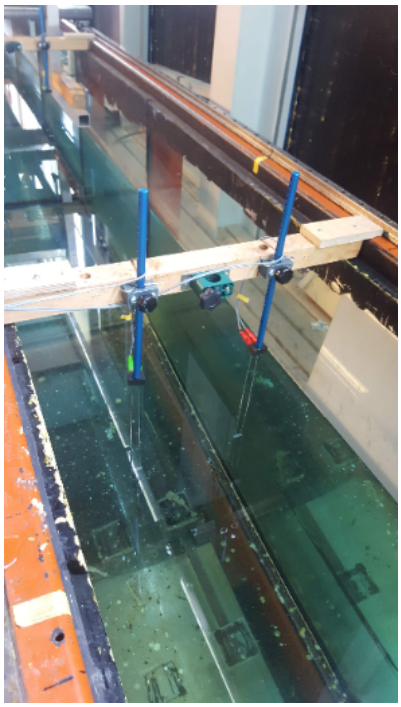

Figure 3.3: The figure shows how the wave probes are mounted in the flume.

3.2 Test Models

Figure 3.4 shows the main dimensions of the models. The models consist of square aluminum cylinders with corners that are regarded as sharp enough to assume fixed separation points. The wall thickness of the square cylinders is 1 mm, and this makes the models very stiff. Thus, the flexibility of the models is not expected to influence the results. The models have the same length, width and thickness, but the perforation ratio is different for the models. The main characteristics of the models are summed up in Table 3.1. The cylinders are sealed to avoid that the cylinders fill with water.

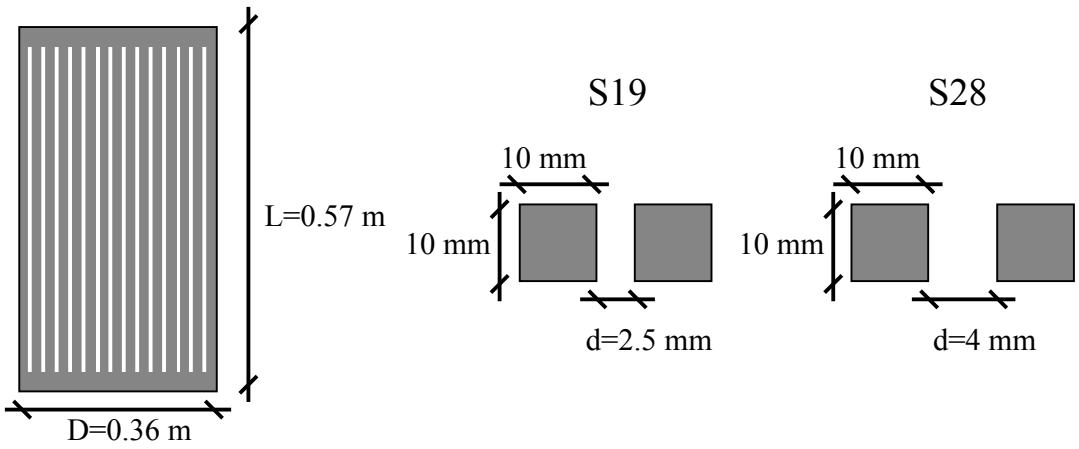

Figure 3.4: Dimensions of the model S19 and S28. They share the same thickness length and width, and the square cylinders also have the same dimensions. The distance between the cylinders is the parameter that differs from the models, and thus the perforation ratio differs. S19 consists of 29 equally spaced square cylinders, and S28 consists of 26. The perforation ratio τ is 0.194 for S19 and 0.278 for S28. They are made of hollow square aluminum cylinders with a wall thickness of 1 mm. They are stiff, such that elasticity is not considered to be a problem in the experiments.

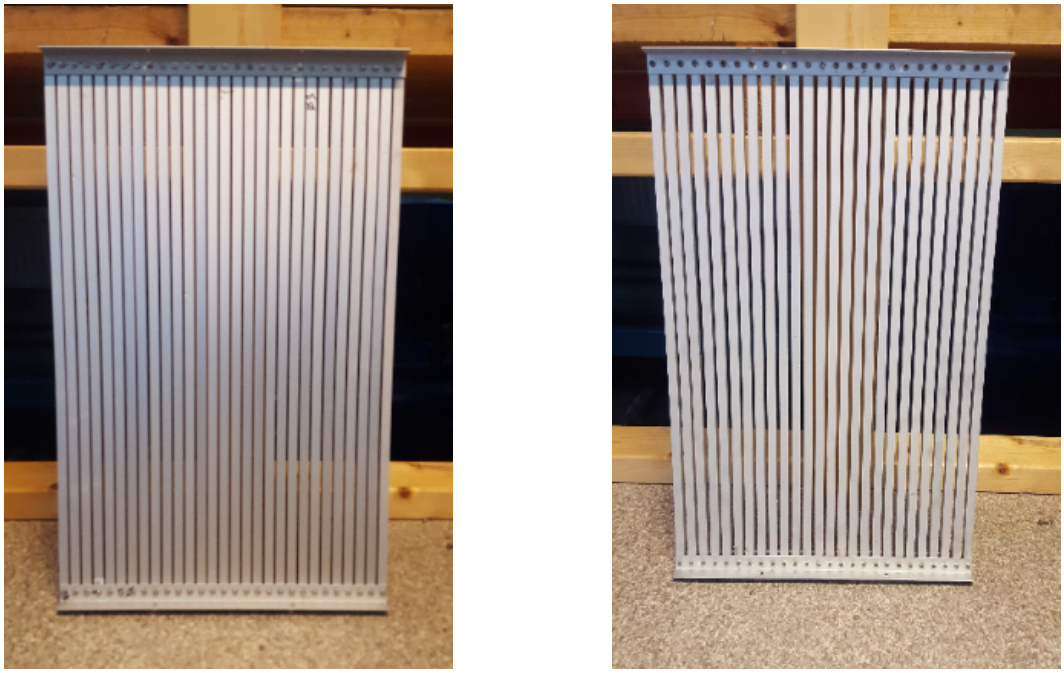

(a) **(b)**

Figure 3.5: (a) Model S19 and (b) Model S28. The models have the same length, thickness and width. The dimentions are given in Figure 3.4. The perforation ratio τ is 0.194 for S19 and 0.278 for S28.

Table 3.1: The table sums up the properties of the models and the weigth of the rig. The total weight of the plate is m, the perforation ratio is τ. The rest of the dimensions is given in Figure 3.4.

Model Name	D	L	Thickness	τ	m	Num. of Cylinders
S19	0.36 m	0.57	10 mm	0.194	2.02 kg	29
S28	0.36 m	0.57	10 mm	0.278	1.75 kg	26
Rig					9.25 kg	

3.3 Test Description

There were conducted experiments on regular motions, bi-chromatic motions, and irregular motions on the two models. The regular tests were done do establish KC dependent curves for the hydrodynamic force coefficients for the models. The bi-chromatic tests were done in order to learn more about what happens with the coefficients when the consecutive amplitudes of motion are changing in a time series.

Three different periods were tested for the regular case, T=1.5 s, T=1.75 s, and T=2 seconds.

The regular motions are expressed as

$$\eta = \eta_a \sin\left(\frac{2\pi}{T}t\right) \tag{3.1}$$

There are done tests for η_a corresponding to KC=0.2 and up to 3. The rig has a limitation for the acceleration, and thus for T=1.5 s, there is not tested for KC higher than approximately 1.9. There were 40 cycles in each test, where the five first is ramp up, and the five last is ramp down. Steady-state was found after just one or two cycles after the ramp-up for all cases. The coefficients for the regular tests are based on the 15 cycles between the ramps where steady-state was found. For the bi-chromatic tests, there were 80 half-cycles in each test were the first ten was a ramp up, and the ten last was a ramp down. Also, for these tests, the hydrodynamic coefficients were calculated based on the 40 half-cycles between the ramps. The rig is programmable, and each set of runs lasted from 3-4 hours. A pause of 60 seconds between each run was found to ensure calm water between each run. For each run, an equal run was done without the model for subtracting the forces.

The bi-chromatic motion has the equation

$$\eta = \frac{X_0}{2}[\sin(\omega t + \phi) + \sin(f_\omega \cdot \omega + \phi)]. \tag{3.2}$$

Six values of f_ω were used, and for each f_ω 14 values of X_0 was tested to obtain a large data set. X_0 raged from 0.0115 m to 0.1719 m, which corresponds to KC from 0.2 to 3. ϕ was zero except for one f_ω, namely the BiChr 7. For f_ω=0.5, there was generated an

interesting time series where there are two consecutive half-cycles with small amplitudes and two half-cycles with large amplitudes. Motion showed to produce interesting results, as a start-up situation was made for the two larger half cycles. There were also done CFD on this bi-chromatic motion. BiChr 7 is shown in Figure 6.12. The rest of the series can be found in Appendix A.

Table 3.2: Data for the bi-chromatic series of Equation 3.2.

Name	X_0 (from-to)	ϕ	f_ω	ω
BiChr 1	0.0115-0.1719 (m)	0	1/1.1	$2\pi/1.75$
BiChr 2	0.0115-0.1719 (m)	0	1/1.2	$2\pi/1.75$
BiChr 3	0.0115-0.1719 (m)	0	1/1.3	$2\pi/1.75$
BiChr 4	0.0115-0.1719 (m)	0	1/1.4	$2\pi/1.75$
BiChr 5	0.0115-0.1719 (m)	0	1/1.5	$2\pi/1.75$
BiChr 6	0.0115-0.1719 (m)	0	1/2	$2\pi/1.75$
BiChr 7	0.0115-0.1719 (m)	$\pi/2$	1/2	$2\pi/1.75$

There were also done two irregular tests. They are described Section 7. The irregular tests were done to test if the knowledge gained from the bi-chromatic tests was applicable to irregularly forced oscillations.

3.4 Error Sources

There are two types of error sources, precision error and biased error. It is not possible to quantify the total error by exact numbers. However, if we succeed in identifying the error sources, they can be used to explain the discrepancies between theory and the experiments. Also, if the error sources are identified, the experiments will be more valuable in the future for comparison to similar experiments.

3.4.1 Precision Error

The sensors that are used are high-quality sensors, and the precision of the accelerometers, potentiometer, and the force transducer is in the order of less than 0.1 percent. The precision of the wave probes is within 1 percent. This is lower than the other biased error sources. The precision error comes from the uncertainty from the measurements. Repeated tests mitigate these errors. In these experiments, this is done by using 15 cycles to find the forces in the regular test. The difference from cycle to cycle is shown in the results by plotting the standard deviation with error bars. This will not only show the precision error, and for the regular tests, they will also show the variation in the flow from cycle to cycle. The deviation is typically 1-3 percent for the regular tests. From this, we can conclude that the precision error is very small, as we expect more variation in the flow from cycle to cycle than precision error in the instrumentation that is used. The variation in the flow from cycle to cycle for regular tests is due to the unstable nature of high Reynolds number flow.

3.4.2 Biased Error

These errors are hard to quantify, and they are a result of the lab setup and human errors while doing the lab. However, several measures are done to mitigate them. The sensors are calibrated carefully and checked every lab day. The accelerometers are cumbersome to check because they are fastened to the rig, and thus they are only calibrated once. The potentiometer is used to check the accelerometers. The potentiometer is checked before every new run. Also, the force transducer was checked with a known weight each lab day. The potentiometer, accelerometer and the force transducer are known to be very robust. They were checked regularly, but there was no need for re-calibration. The wave probe is sensitive to the water temperature and water level in the tank. The water level in Ladertanken varies slightly from day to day and this affected the wave probes. Thus, the wave probes were needed to be re-calibrated every day, and they were checked before every run.

Fourier averaging is used to find the force coefficients for the regular tests. This method for finding the coefficients is very robust and accurate if there is no phase lag between the accelerometer and the force measurement. However, Fourier averaging is very sensitive for a phase lag between the force measurements and the acceleration. If the phase is wrong, the coefficients will be split incorrectly even though the total force will be correct. The sampling frequency must also be high enough to have a good resolution of the time series. Mentzoni (2020) put serious work into this particular lab setup, and he had a focus on reducing errors regarding phase lag between the force and acceleration measurements. A potentiometer was also used as redundancy and to check the accelerometer and the phase. The rig position measurements were in good agreement between these two. The amplitude deviated less than 1 percent, and there was no phase lag. The cure for eliminating the phase lag is to use a high enough sampling rate. A sampling rate of 200 Hz is used in these experiments. The numerical calculations also strengthen the validity of the experiments, because, in the calculations, the problem regarding phase lag does not exist. The results of the experiment and the CFD calculations were in good agreement.

Another source of error is when the least square method is used to find the hydrodynamic coefficients in the bi-chromatic series. Based on the discussion in Section 4.3.2, the method is regarded as a good method of finding the force coefficients.

The last error source is regarding the lab setup. There will be hydrodynamic forces on the acrylic glass plates that hold the model. They are 420 mm wide and 6 mm thick, and it is 9 mm between the acrylic glass plate and the tank wall. The hydrodynamic forces will have one added mass component and one drag component due to friction drag. It was observed that the water between the acrylic plate and the tank wall was oscillating. These forces are subtracted. This is done by doing a run where the model is removed and replaced by thin stiffeners with negligible hydrodynamic force. Then the force from the empty rig is subtracted for each of the time-steps.

Three biased errors occur from this method. The first is that the signals must be aligned so that the empty rig's forces are subtracted correctly. This is done by a code coded in Matlab, and whenever the code found an error in the alignment, it was fixed manually such that the alignment of the signal always is within the sampling frequency. Therefore

this error is considered negligible.

The second error source is that whenever the model is changed, the wooden box-acrylic glass assembly needs to be loosened and taken out of the tank. Thus, there will be some variation in the distance from the tank wall to the acrylic glass plates from time to time. The position was marked on the wooden box such that the distance to the tank wall was equal on each side. A parameter study could have been done to quantify this error, but this was not done in these experiments. However, this error is considered to be small since much caution was done when mounting the wooden bow to the rest of the rig. Also, this error is probably smaller than the third error source.

The third error source regarding the rig is that when the model is present in the test, there will be a pressure field from the model that probably affects the acrylic glass plates' forces. This error is not quantified, and the only way of asses this error is to compare the hydrodynamic load on the model to the hydrodynamic load on the empty rig. A fix on this problem could for future experiments be to use acrylic glass end plates that are longer, such that the model is further away from the acrylic glass plate ends. Thus, the pressure field from the model will not affect the water between the acrylic glass plate and the tank wall.

The force on the empty rig is decomposed as

$$F_{rig} = -(m_{rig} + A_{rig})\ddot{\eta} - B_{rig}\dot{\eta}. \tag{3.3}$$

Figure 3.6 shows the hydrodynamic forces on the rig as defined in Equation 3.3. The hydrostatic pressure is also included in A. The hydrostatic pressure for the acrylic plates is 180 degrees out of phase with the position. This means that the hydrostatic pressure is in phase with the acceleration, which means that the hydrostatic pressure is 180 degrees out of phase with the hydrodynamic inertia force. However, the hydrostatic pressure is independent of the frequency, and it is included in the inertia term for simplicity. The results are in good agreement with the results in Figure 3.10 in the doctoral thesis of Mentzoni (2020). Note that in his figures, he uses the amplitude of motion on the x-axes, and he decomposes the rig force by only one term proportional to the acceleration and one term into damping. The figure suggests that the uncertainty regarding the empty rig forces decreases as the KC number goes up. The hydrodynamic force on the model increases more than the hydrodynamic forces on the acrylic glass plates. Figure 3.6 also shows that the added mass for the empty rig is higher for a lower period of oscillation. Why this is the case is not known, but it is worth mentioning since it is observed that the added mass for the model is lower for higher oscillation frequencies.

Table 3.3 shows the added mass and damping of the rig as a fraction of the added mass and damping found on S28. For small KC numbers, the fraction is larger, and thus the uncertainty is higher for very small KC numbers than for higher KC numbers regarding the forces on the acrylic glass plates. For KC numbers larger than 1, the hydrodynamic forces on the empty rig are smaller than 10 % and decrease to 3.5 % for the damping and 6 % for the added mass. Ideally, a parameter study should be done where the size of the acrylic plates was changed to see the effect of the pressure field from the model on the hydrodynamic forces on the acrylic glass plates. This is much work and expensive, and

maybe even unnecessary as we have shown that the hydrodynamic forces are small on the acrylic glass plates. Also, there are done CFD calculations that are in good agreement with the experiments. The CFD strengthens the validity of the assumption that the empty rig force can be subtracted from the run with the model. Also, it is important to keep in mind that the model's presence is less important for smaller KC numbers because the pressure field from the model is weak. With this, it is argued that the assumption that the rig forces can be subtracted to be valid for small KC numbers because of a negligible pressure field from the model. For high KC numbers, the forces on the acrylic plates are only a small portion of the force on the model, and thus the uncertainty goes down for high KC numbers.

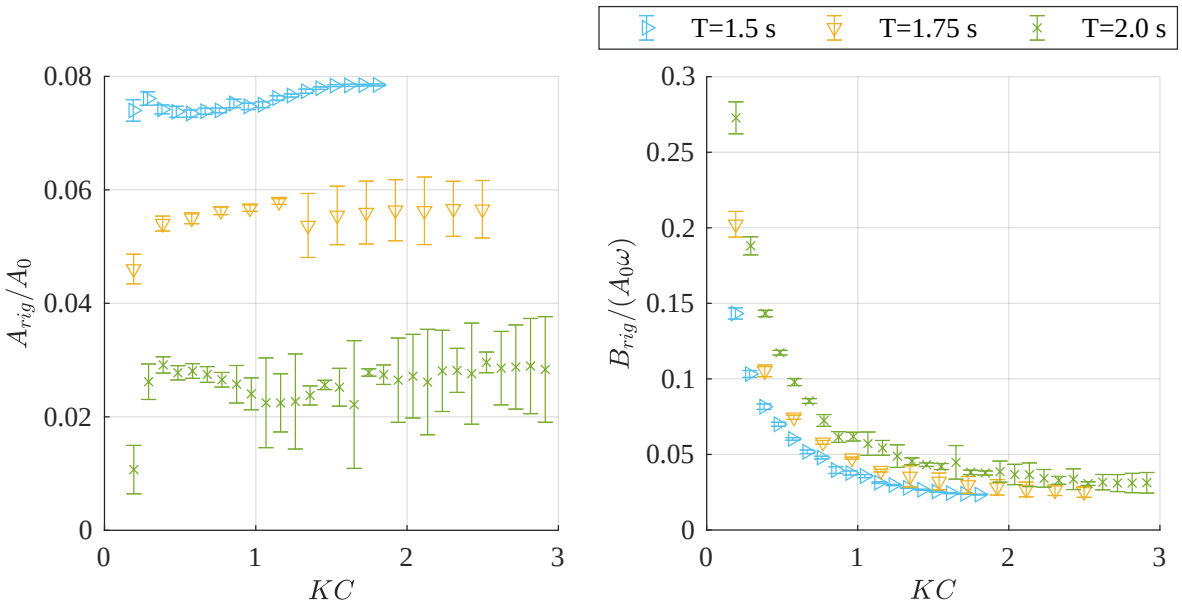

Figure 3.6: (a) The added mass coefficient and (b) the damping coefficient. The hydrodynamic force coefficients are normalized on on the reference added mass (same as for the plates) and the KC is also calculated based on the model width D which are the same for both models. This is done such that the results are directly comparable with the hydrodynamic force coefficients for the models.

Table 3.3: Hydrodynamic force coefficients for the rig as a fraction of the damping and added mass for model S28. This table shows that the rig forces becomes small compared to the hydrodynamic forces on the plate as the KC number increases.

KC	A_{rig}/A_{S28}	B_{rig}/B_{S28}
0.5	0.15	0.30
1.0	0.10	0.10
2.0	0.07	0.05
3.0	0.06	0.04

4 Post Processing

4.1 Filtering

By-pass filtering was used to filter the signals. The force signal is filtered at $10f_{osc}$ to ensure all the harmonics from the hydrodynamics are captures. f_{osc} is the frequency of forced oscillations. This is well below the rig's eigenfrequency, which is seen from the hammer test in Figure 4.1. From the figure, one can see that the frequency of the vibrations from the rig is far from the hydrodynamic forces' frequency. On this basis, it is concluded that no relevant information regarding the hydrodynamics, is filtered out when setting the upper limit at $10f_{osc}$ and that the noise from the rig is filtered out. The low limit was $0.2f_{osc}$. The signal from the accelerometer was filtered around the first-harmonics for the regular tests, and for the bi-chromatic and irregular test, the by-pass filter was set in a range such that all frequencies of the force oscillations are let through.

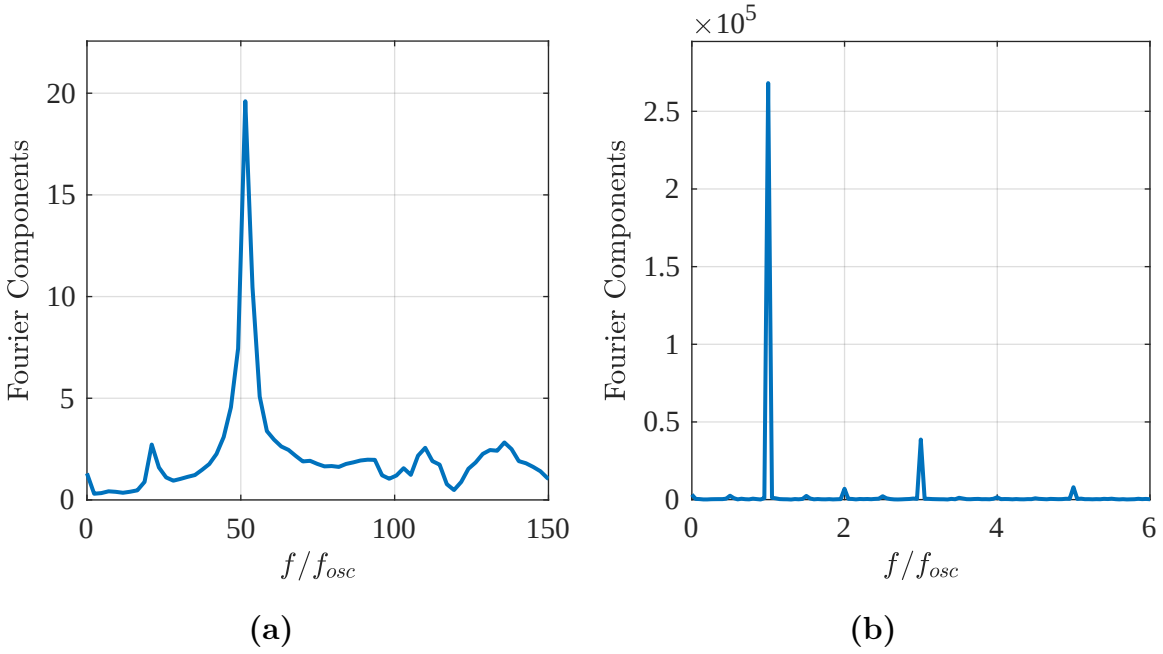

Figure 4.1: (a) Hammer test for S19. (b) Force spectrum for S28 at KC=2.04. The figure shows that most of the force is concentrated at the first and third-harmonics.

Figure 4.2 shows the measured and filtered force time series. It also shows the by-passed first and third-harmonics of the measured force. The third-harmonic force for S19 has a similar magnitude as S28 relative to the first-harmonic, but with a different phase relative to the damping, which can be seen in Section 6.3.

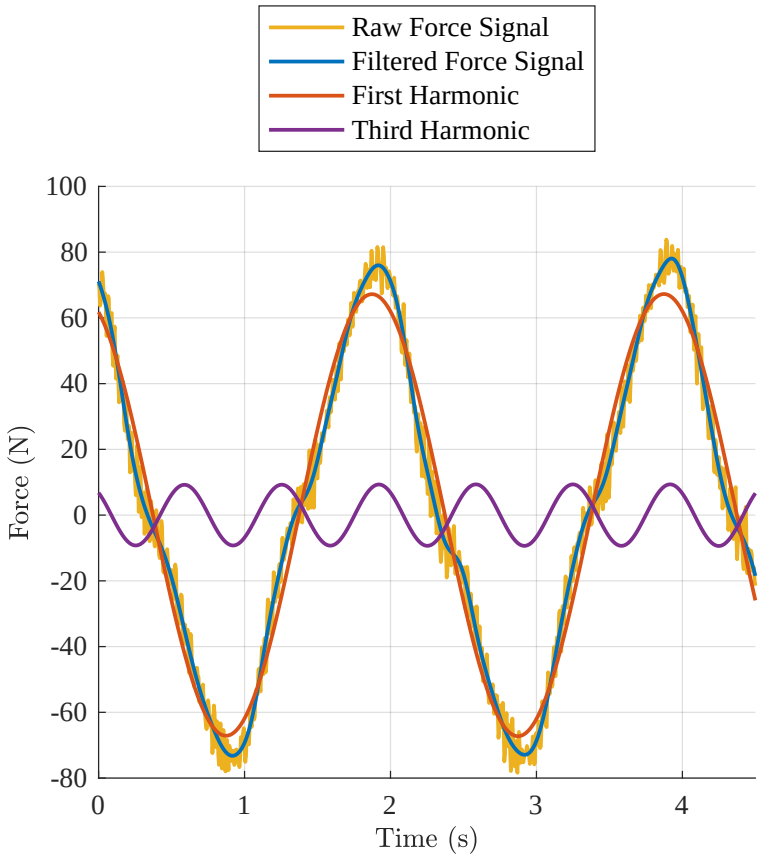

Figure 4.2: Force measurements for S28 for KC=2.04. The period of oscillation is 2 seconds. The figure shows raw data, filtered data (bypassed in the range $[0.2f_{osc}, 10f_{osc}]$), bypassed first-harmonic force and bypassed third-harmonic force. f_{osc} is the frequency of the forced plate oscillations.

4.2 Definitions of the Half-Cycle

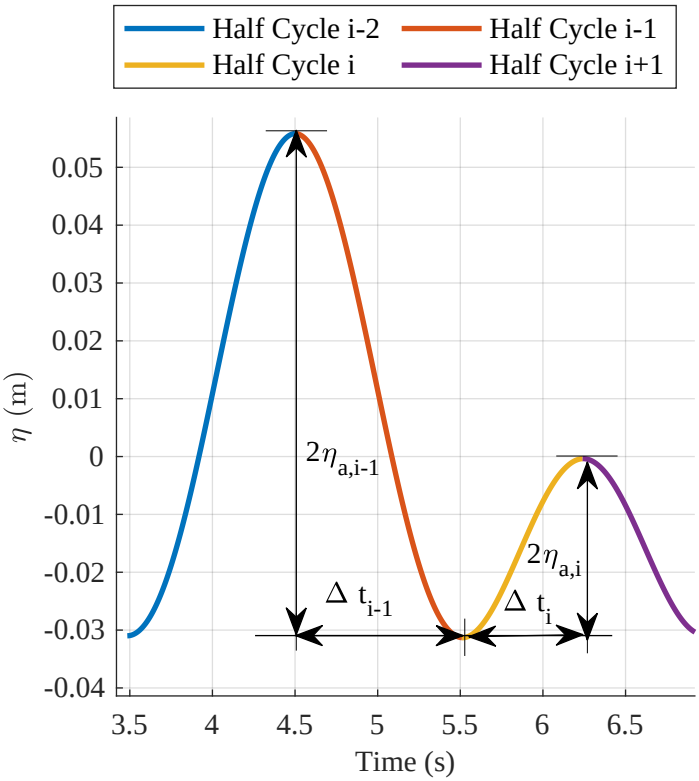

Figure 4.3: Definition of the half-cycle.

When the Bi-Chromatic motions are investigated, there is a need for splitting of the time series into half-cycles. This must be done because the hydrodynamic coefficients will vary with the amplitude of motion for the half cycle. The half-cycle is defined in Figure 4.3. The KC number for the half-cycle depends on the amplitude of motion $\eta_{a,i}$ in the figure. The KC number of the half-cycle, KC_i becomes

$$KC_i = \frac{2\pi\eta_{a,i}}{D} \tag{4.1}$$

In this thesis, the amplitude of the half-cycle refers to the amplitude of motion for the half-cycle if not specified. The period for a half cycle is defined in Figure 4.3. It is found as

$$T_i = 2\Delta t_i \tag{4.2}$$

The circular frequency for the half-cycle becomes

$$\omega_i = \frac{2\pi}{T_i} \tag{4.3}$$

4.3 Hydrodynamic Coefficients

The hydrodynamic force on the plate is decomposed by an inertia term and a damping term as

$$F_{model} = C_a A_0 \ddot{\eta} + C_B A_0 \omega \dot{\eta}. \tag{4.4}$$

To find these coefficients from the lab results, the forces that act on the rig must be subtracted from the measured force.

The forces on the model were found as

$$F_{model} = F_{model+rig} - F_{rig}, \tag{4.5}$$

were F_{rig} was found in the empty rig run without the model. The error sources finding the forces on the model by subtracting the empty rig are discussed in Section 3.4.2.

In the CFD calculations, there is a pressure gradient in the fluid due to that the fluid is forced to oscillate instead of the model. Thus, the contribution from the pressure gradient forces must be subtracted to ensure comparable results with the experiments (Mentzoni and Kristiansen, 2019b). This subtraction can be done since the kinematics in the fluid are equal, as in the case where the plate is oscillating. The only difference in the dynamics in the flow is this pressure gradient (Graham, 1980). The force on the model in CFD is found as

$$F_{model} = F_{CFD} - \rho V \dot{w} \tag{4.6}$$

Here $\ddot{w}$ is the fluid acceleration, and V is the plate volume.

4.3.1 Regular Forced Oscillations

The coefficients for the regular case was found from Fourier averaging as

$$A \int_{mT} \ddot{\eta}^2 dt = \int_{mT} F_{model} \ddot{\eta} dt \tag{4.7}$$

$$B \int_{mT} \dot{\eta}^2 dt = \int_{mT} F_{model} \dot{\eta} dt \tag{4.8}$$

Here mT means that the integration is taken over m cycles. For these experiments, 15 cycles are used.

4.3.2 Curve-Fitting for Bi-Chromatic Motions

The Added mass and damping was found by finding the least-square error of the equation

$$F_{model} = C_a A_0 \ddot{\eta} + C_b A_0 \omega \ddot{\eta}, \tag{4.9}$$

were C_a and C_b is to be determined.

They are found by

$$C_b = \left(\sum_{j=1}^{N} F_{model} F_b \cdot \sum_{j=1}^{N} F_a^2 - \sum_{j=1}^{N} F F_a \cdot \sum_{j=1}^{N} F_b F_a \right) \cdot \frac{1}{C_{det}}, \tag{4.10}$$

and

$$C_a = \left(\sum_{j=1}^{N} F_{model} F_a \cdot \sum_{j=1}^{N} F_b^2 - \sum_{j=1}^{N} F F_b \cdot \sum_{j=1}^{N} F_b F_a \right) \cdot \frac{1}{C_{det}}. \tag{4.11}$$

Here C_{det} is

$$C_{det} = \sum_{i=1}^{N} F_b^2 \sum_{j=1}^{N} Fa^2 - \left(\sum_{j=1}^{N} F_b F_a \right)^2, \tag{4.12}$$

and F_a and F_b is

$$F_a = F_a(t_j) = A_0 \ddot{\eta}(t_j) \tag{4.13}$$

and

$$F_b = F_b(t_j) = A_0 \omega \ddot{\eta}(t_j). \tag{4.14}$$

If this is done for half-cycle "i", ω is ω_i. j=1 is the start of the half-cycle and $j = N$ at last element of half-cycle number "i." The inbuilt Matlab function "lsqcurvefit" is used to solve these equations. In Figure 4.4, the curve-fit method is checked against the Fourier averaging method. The figure shows a larger spread for the different half cycles for the curve-fit, but the averages are the same. The reason for the spread in the added mass is because it was found that the added mass was dependent on the half-cycle, whether the model is moving towards the free surface or towards the tank bottom. The added mass was smaller in half-cycles where the plate was moving towards the free surface than half-cycles were the plate moves towards the tank bottom. The difference between these relative to the average was approximately 10-20% for small amplitudes. The difference is reduced and in absolute value for larger amplitudes, as can be seen in the Figure 4.4. The reason for this is unknown, but the rig-setup and the observed oscillating water between the glass acrylic plates can be an explanation. Also, the free surface could be an explanation. However, then one should expect that the absolute value of the standard deviation increases when the amplitude increases, due to that the effect of the free surface becomes more important (but still small) for larger amplitudes

as is discussed in Section 6.2. There was found a large added mass for one half-cycle in the series BiChr 7 (half cycle 2 in Figure 6.12) and also this half-cycle was when the plate was moving towards the tank bottom. However, this increase in the added mass also occurred for the highest KC numbers for BiChr 7, and the same trend was found in CFD calculations. Ikeda et al. (1988) found this effect for flat plates in a start-up situation, and thus the increase in the added mass for BiChr 7 at half-cycle 2 is not likely to be a result of the difference for half-cycles moving towards the free surface and tank-bottom. Fourier averaging requires a full cycle to calculate the hydrodynamic coefficient, and because of this, the standard deviation is lower for Fourier averaging. The figures in this section show that even though a large spread is found for some KC numbers, the average is found close to the Fourier average. The variations for the added mass is close to zero if one separates half-cycles were the plate is going toward the free surface from the half-cycles were the plates goes toward the tank bottom. Fourier averaging guaranties that the first-harmonic is isolated, while the curve-fit method does not. However, this test places more confidence in that the curve-fit method also is a suitable method for estimating the first-harmonic hydrodynamic coefficients.

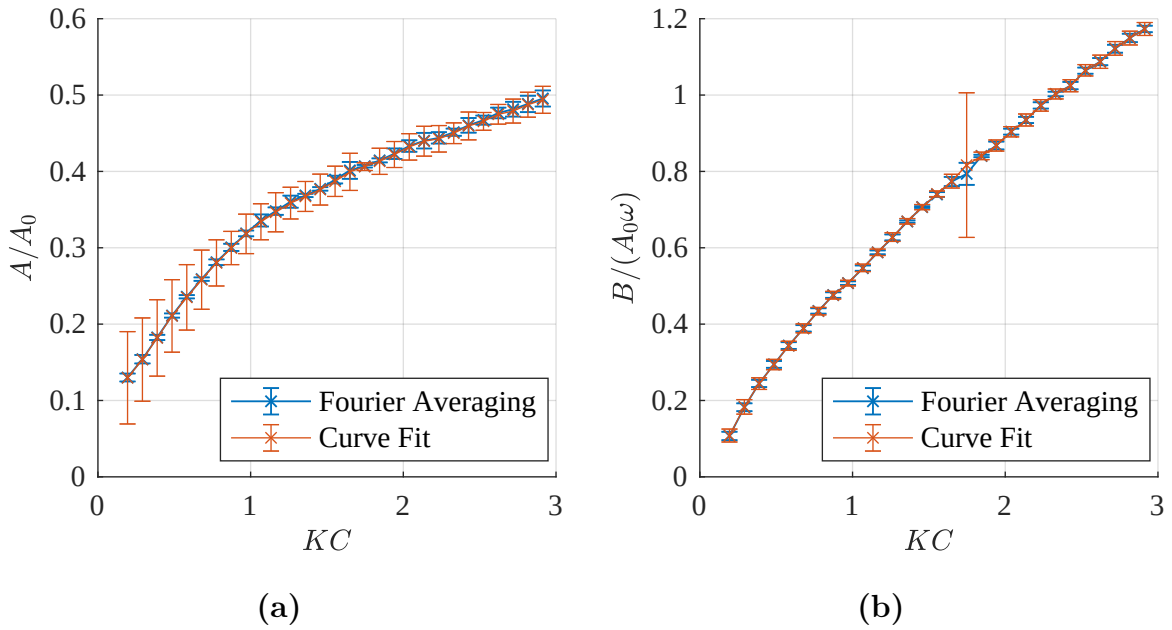

Figure 4.4: Check of the curve-fit method on S28 versus Fourier averaging.T=2s, for plate S28. (a) Normalized added mass and (b) normalized damping.

4.3.3 Third-Harmonic Force Coefficients

Hydrodynamic forces of the tested models consist mainly of first and third-harmonic forces. This is shown in Figure 4.2. If the velocity of the forced oscillations of the plate is

$$\dot{\eta} = \eta_a sin(\omega t). \tag{4.15}$$

The force can be written as a Fourier series of the first and third-harmonics where the second-harmonics, and higher-order harmonic terms are neglected. That is

$$F = a_1 \cos(\omega t) + b_1 \sin(\omega t) + a_3 \cos(3\omega t) + b_3 \sin(3\omega t) \tag{4.16}$$

The first-harmonic coefficients $a1$ and $b1$, relate to the hydrodynamic coefficients as

$$C_A = -\frac{a_1}{\omega^2 A_0 \eta_a} \tag{4.17}$$

and

$$C_B = -\frac{b_1}{\omega^2 A_0 \eta_a} \tag{4.18}$$

The Fourier coefficients a_3 and b_3 can be found by finding a starting point where the velocity is zero, and the derivative is positive, such that Equation 4.15 is valid for the velocity signal. Then by evaluating an integer number of full cycles, the Fourier coefficients can be found. Figure 4.5 is included to show that the method of aligning the signal and by use of the inbuilt function fourier8 from Matlab to find the Fourier coefficients yielded results similar as for Fourier averaging for the first-harmonics, but it is not as accurate. The fourier8 function in Matlab is based on a non-linear least-square scheme. The method was tested for some known analytic cases and it was found to be very robust in finding the correct Fourier coefficients. However, the method is very sensitive to the alignment of the signal. If the position signal is not sinusoidal, the hydrodynamic coefficients will not be found correctly as added mass and damping because of the phase difference. The code that was made for this purpose sometimes failed when aligning the signal. Thus, these points were removed. The success of the method depends on if it finds the first-harmonics correctly due to that it is sensitive to the alignment.

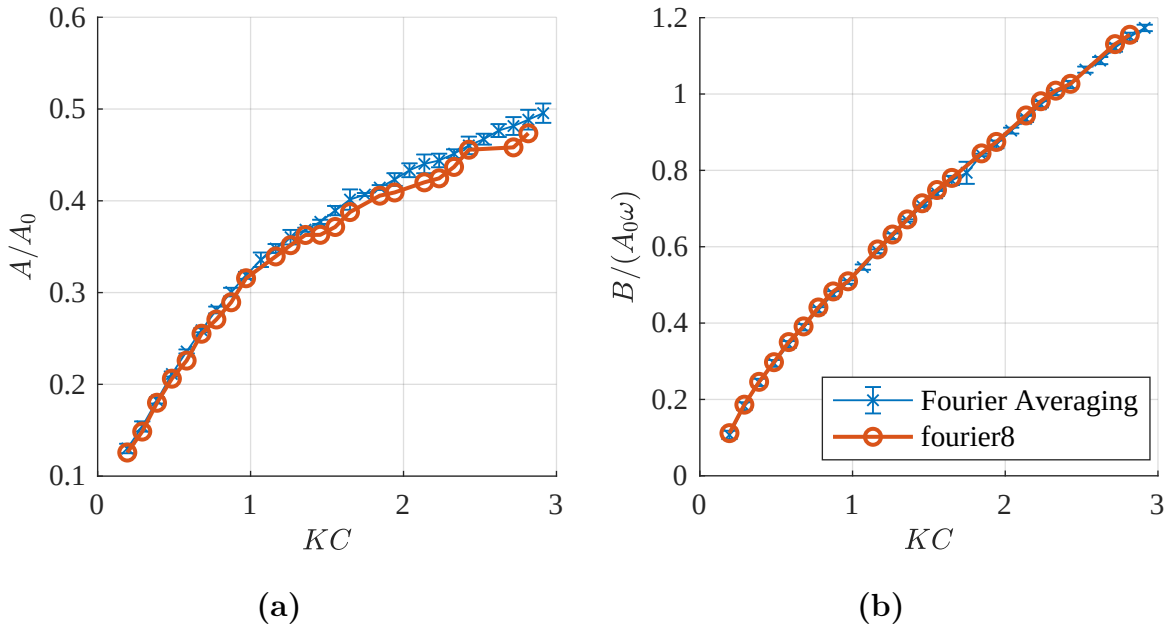

(a) **(b)**

Figure 4.5: Check of fourier8 (inbuilt matlab function) versus Fourier averagig on plate S28 for regular forced oscillations (T=2s). (a) Normalized added mass and (b) normalized damping.

5 Numerical Simulation

5.1 Solver

The solver used in this thesis is developed and programmed by Fredrik Mentzoni and is described in detail and validated in his doctoral theses (Mentzoni, 2020). The CFD code supports orbital flow, free surface, oscillatory flow, and a hybrid-flow formulation. The hybrid flow divides the flow into regions where the diffusion and advection terms are omitted, and thus these regions have the same properties as a potential flow. The function used in this thesis is the oscillatory flow. The governing equations are solved with a fractional-step method, as described by Chorin (1968).

The computational domain and the boundaries are defined in Figure 5.1. The code utilizes that the same kinematics (velocities) in the flow can be obtained by oscillating the fluid instead of the model. The only difference in the dynamics (pressure) in the flow is the linear pressure gradient due to that the fluid is accelerated, but this contribution can be subtracted after(Graham, 1980). The boundary conditions for the velocity for boundary 1-4 in Figure 5.1 is for the regular runs:

$$u = 0, \qquad w = \frac{D}{T} KC \sin(\omega t), \tag{5.1}$$

where u and w is the velocity in the x- and z-direction, respectively.

The bi-chromatic motion that was tested is BiChr 7 which mean that the boundary conditions for boundary 1-4 becomes:

$$u = 0, \qquad w = \frac{X_0 \omega}{2} \left(\cos(\omega t + \frac{\pi}{2}) + \frac{1}{2} \cos(\frac{\omega}{2} t + \frac{\pi}{2}) \right) \tag{5.2}$$

The boundary conditions for the pressure is

$$\frac{\partial p}{\partial x} = -\rho \frac{\partial u}{\partial t} = 0 \quad \text{and} \quad \frac{\partial p}{\partial z} = -\rho \frac{\partial w}{\partial t} \tag{5.3}$$

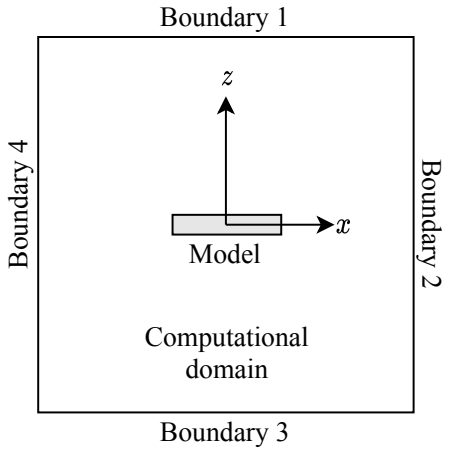

Figure 5.1: The figure defines the axis system and names the boundaries of the computational domain.

No-slip condition is applied on the model's boundaries, together with the impermeable wall condition, which means that

$$u = 0, w = 0, \quad \frac{\partial p}{\partial x} = 0, \quad \text{and} \quad \frac{\partial p}{\partial z} = 0 \tag{5.4}$$

Figure 5.2 shows a cell and the staggered grid system for the velocities and the pressure. The grid needs to be staggered to ensure coupling between the velocity components and the pressure.

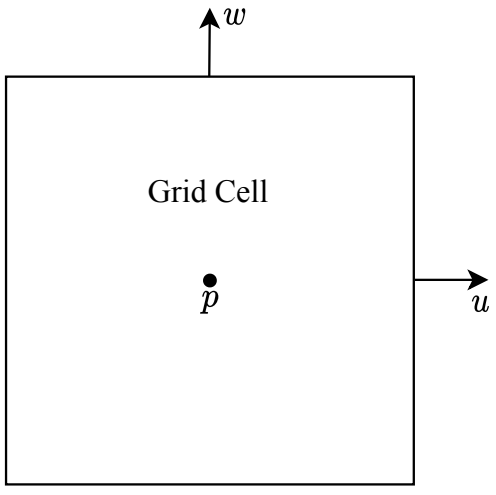

Figure 5.2: The velocities and pressure are solved on a staggered grid to ensure coupling between them.

To simplify the problem the following assumptions about the fluid is done:

- Constant viscosity
- Incompressible fluid
- No gravity
- Laminar flow
- Isothermal flow

The equations that need to be solved are the continuity equation and the Navier-Stokes equation. With the given assumptions about the fluid and Einstein notation, the continuity equation can be written as

$$\frac{\partial u_i}{\partial x_i} = 0, \tag{5.5}$$

and the incompressible Navier-Stokes equation can be written as

$$\frac{\partial u_i}{\partial t} + u_j \frac{\partial u_i}{\partial x_j} = -\frac{1}{\rho}\frac{\partial p}{\partial x_i} + \nu \frac{\partial^2 u_i}{\partial x_j^2}. \tag{5.6}$$

These equations are solved using a numerical scheme. The viscous flow solver is based on a fractional-step method where the Navier-Stokes equation is split into two steps as

$$\frac{u_i^* - u_i^n}{\Delta t} = -u_j \frac{\partial u_i}{\partial x_j} + \nu \frac{\partial^2 u_i}{\partial x_j^2} \tag{5.7}$$

and

$$\frac{u_i^{n+1} - u_i^*}{\Delta t} = -\frac{1}{\rho}\frac{\partial p}{\partial x_i}. \tag{5.8}$$

Since the requirement of no divergence at the new time step the continuity equation at the new time step is

$$\frac{\partial u_i^{n+1}}{\partial x_i} = 0. \tag{5.9}$$

By taking the divergence of Equation 5.8 and by combining it with Equation 5.9, a new equation for the pressure is obtained as

$$\frac{\partial^2 p}{\partial x_i^2} = \frac{\rho}{\Delta t}\frac{\partial u_i^*}{\partial x_i}. \tag{5.10}$$

This equation is a Poisson equation for the pressure and needs to be solved for each time step in order to ensure the flow is divergence-free.

Equation 5.7, Equation 5.8 and Equation 5.10 need discretization in both time and space.

The diffusion term in Equation 5.7, the pressure gradient in Equation 5.8 and both sides of Equation 5.9 is discretized in space using second order accurate central difference scheme. For the advection term on the right-hand side of Equation 5.7 a first order upwind scheme is used.

To solve Equation 5.7 implicit Euler scheme is used. A first-order forward scheme is used to find the new velocity in Equation 5.8. The advection term is linearly discretized in time on the left-hand side of Equation 5.7.

5.2 Convergence Study

A convergence study is done to make sure the result from the CFD simulations has converged. This means that we will make sure that we have reached a fine enough grid and time step such that further refinement of the mesh of time will not affect the results much. If this state is reached, we say that the results have converged, and the result is not sensitive to a further refinement of the mesh. However, this is not a guarantee that the solved flow corresponds with the real flow. Examples, where the computed results do not converge to the true results, are if physical phenomena like shock or turbulence are important for the real flow and are not supported or captured by the numerical scheme or the equations that are solved. Thus, it is important to have a priori knowledge of the flow or verify the CFD results by experiments.

Even simple flow problems like a uniform flow about a circular cylinder at low Reynolds numbers can be challenging to solve correctly without knowledge about the problem. Critical parameters for the case of a cylinder is that the boundary layer is properly refined and that there are enough cells around the cylinder to get the correct separation point.

In the case of model S28 that is used in these calculations, there are only sharp corners. This simplifies the analysis and the need for a fine mesh. The reason for this is mainly because of the points of separation are fixed. The separation point is fixed due to a geometrical singularity at the sharp corner. The vorticity flux into the wake is not sensitive to the refinement of the boundary layer, because it is determined by the velocity outside the boundary layer at the point of separation. Separation and vorticity generation is described more in the two following sections.

5.2.1 Separation

Steady viscous fluid-flows always separate at corners with a geometrical singularity. In an accelerated fluid from rest, Pullin (1978) found that the roll-up of the vortex sheet starts immediately in a self-similar manner. This means that the boundary layer is not attached to the body but rolls up as a vortex at the sharp edge even at very small time instances due to the vorticity in the boundary layer. The flow separates because of irreversible losses due to viscosity. The entropy rises in the flow and causes loss in the mechanical energy, as some of the energy goes to heat. This means that the pressure cannot reach infinite values at the corner as in potential flow. Consequently, the fluid parcel cannot have infinite acceleration around the corner, and due to the inertia of the fluid, the flow separates. The condition that the flow separates at geometrical singularities is called the Kutta-condition. The Kutta-condition states that a fluid always leaves tangentially from the surface before the corner. The Kutta-condition is a widely used engineering tool and is used in inviscid flow modeling were separation must be considered, as in vortex tracking methods (Kristiansen and Faltinsen, 2008). The losses in the flow couples the continuity equation to the momentum equation, which makes them complicated to solve, and numerical tools are needed.

5.2.2 Vorticity Generation

The vorticity generation is important because the vorticity is shed into the wake and forms vortices. The velocity profile of the boundary layer and the vorticity flux into the wake is generally of importance. For bluff bodies with rounded corners, the velocity profile is of importance in order to be able to determine the correct adverse pressure gradient in the boundary layer, which in turn is important to determine the correct location of the separation point. However, for sharp-edged bodies, the separation points are fixed at the sharp edges. Consequently, the most important parameter that defines the wake is the flux of vorticity that is shed into the wake. The theory in this chapter is a combination of lecture notes from the course "Hydrodynamic Aspects of Marine Structures 2", which is taught by Trygve Kristiansen, and theory from the book "Sea Loads on Ships And Offshore Structures" by Faltinsen (1990), page 181-184. This theory is necessary to include to be able to understand why good force prediction can be obtained on a relatively coarse mesh for sharp-edged objects even though the boundary layer is not fully resolved.

Let the velocity field of an potential be described by

$$\nabla\phi = \overrightarrow{V}, \tag{5.11}$$

were

$$\overrightarrow{V} = u\hat{\boldsymbol{\imath}} + v\hat{\boldsymbol{\jmath}} \tag{5.12}$$

and

$$\nabla = \frac{\partial}{\partial x}\hat{\boldsymbol{\imath}} + \frac{\partial}{\partial y}\hat{\boldsymbol{\jmath}}, \tag{5.13}$$

and $\hat{\boldsymbol{\imath}}$ and $\hat{\boldsymbol{\jmath}}$ are the unit vectors in the x- and y-direction, respectively.

Since the flow is irrotational, the only contribution to the circulation is the discontinuity in the vector field introduced by the vortex sheet. The separation is introduced by a Kutta-condition. The circulation over a curve surrounding the vortex, as the green curve c in Figure 5.3, can be found by taking a closed curve integral over the curve

$$\Gamma = \oint_c \nabla\phi \cdot \hat{s}\, ds = \oint_c \frac{\partial \overrightarrow{V}}{\partial s}\, ds = \phi^+ - \phi^- \tag{5.14}$$

The pressure is impressed from both sides of the sheet as

$$p^+ = p^- \tag{5.15}$$

This holds, even if the vortex sheet is curved if we assume that the vortex sheet is very thin. The unsteady Bernoulli equation without the gravity term is

$$-\frac{1}{\rho}p = \frac{\partial\phi}{\partial t} + \frac{1}{2}\nabla\phi\cdot\nabla\phi = \frac{\partial\phi}{\partial t} + \frac{1}{2}\left(\frac{\partial\phi}{\partial x}\right)^2 + \frac{1}{2}\left(\frac{\partial\phi}{\partial y}\right)^2. \tag{5.16}$$

By using Equation 5.15 and Equation 5.16 the pressure difference of the upper- and lower side of the vortex sheet can be written as

$$0 = \frac{1}{\rho}(p^- - p^+) = \frac{\partial \phi^+}{\partial t} - \frac{\partial \phi^-}{\partial t} + \frac{1}{2}\left(\frac{\partial \phi^+}{\partial x}\right)^2 - \frac{1}{2}\left(\frac{\partial \phi^-}{\partial x}\right)^2 + \frac{1}{2}\left(\frac{\partial \phi^+}{\partial y}\right)^2 - \frac{1}{2}\left(\frac{\partial \phi^-}{\partial y}\right)^2 \quad (5.17)$$

At stagnation point A, at the corner in Figure 5.3, the velocity in the y-direction is zero such that

$$\frac{\partial \phi^+}{\partial y} = \frac{\partial \phi^-}{\partial y} = 0. \quad (5.18)$$

At the upper side of the vortex sheet at the stagnation point, the velocity in the x-direction is zero, which means that $\partial \phi^- / \partial x = 0$.

If the vortex sheet is thin, i.e. $\delta \to 0$, we get that

$$\frac{\partial \phi^+}{\partial x} = U_s, \quad (5.19)$$

where U_s is the velocity of the flow just outside the boundary layer. U_s is found, for instance, from the inviscid velocity potential together with a Kutta-Condition.

By combining the knowledge of the velocities at the stagnation point, Equation 5.17 reduces to

$$0 = \frac{\partial}{\partial t}(\phi^+ - \phi^-) + \frac{1}{2}(\frac{\partial \phi^+}{\partial x})^2 \quad (5.20)$$

By using Equation 5.14 and Equation 5.19 we get that the vorticity flux that is shed into the wake is

$$\frac{\partial \Gamma}{\partial t} = -\frac{1}{2}U_s^2. \quad (5.21)$$

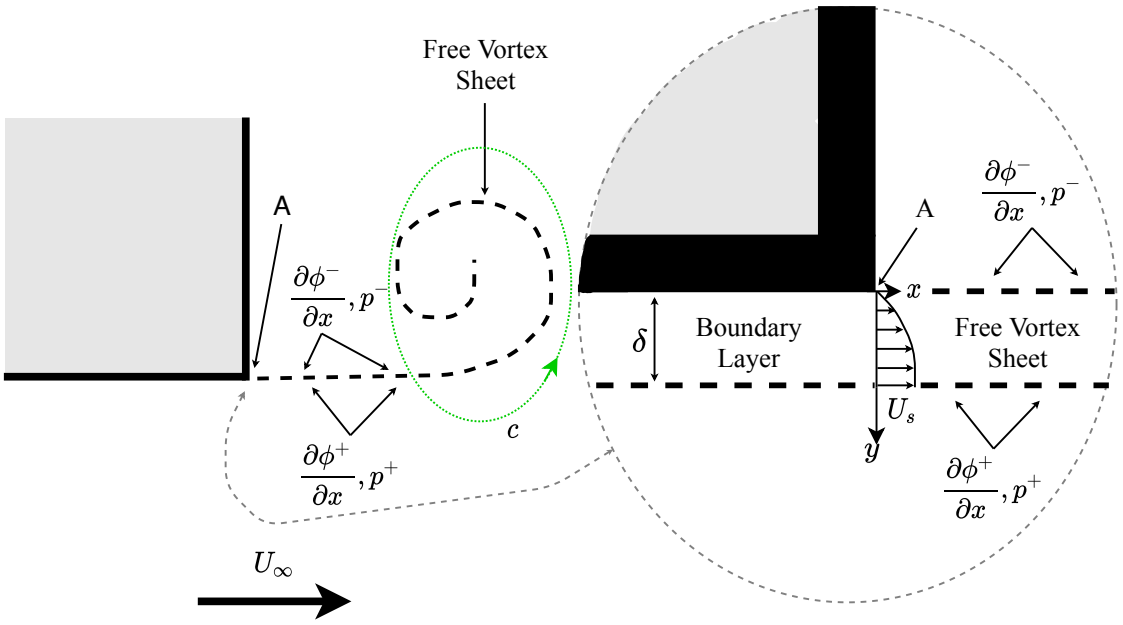

Figure 5.3: Example of a boundary layer that is separated from a sharp corner, called A. The vorticity flux is given by the Bernoulli equation, is only dependent on the velocity just outside the boundary layer U_s. ϕ is the velocity potential, p is the pressure. The axis is defined in the close-up part of the figure. The positive and negative superscripts for p and ϕ are introduced to show the discontinuity over the vortex sheet.

The vorticity shed into the wake can also be found by evaluating the boundary layer. The rate of change in the circulation of the vortex formed at the corner is

$$\frac{\partial\Gamma}{\partial t} = -\int_0^\delta (\frac{\partial u}{\partial y} - \frac{\partial v}{\partial x})udy = -\int_0^\delta \frac{\partial u}{\partial y}udy = -\frac{1}{2}[u^2]_0^\delta = -\frac{1}{2}U_s^2, \tag{5.22}$$

which is the same result as when a vortex sheet is introduced in the velocity potential. It is worth noting that the vorticity flux is not dependent on the shape of the boundary layer's velocity profile. This means that the two boundary layers in Figure 5.4 generate the same amount of circulation as long U_s is the same. Thus, a full resolution of the boundary layer is not needed if the separation point is fixed, and U_s is correctly computed.

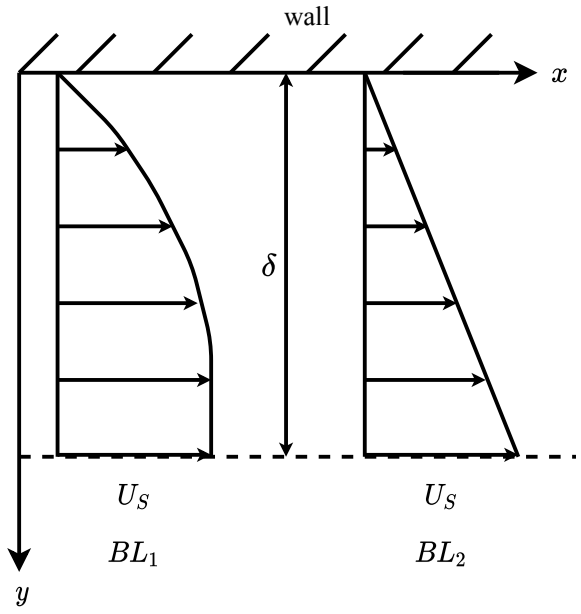

Figure 5.4: The figure shows examples of two different boundary layers, BL_1 and BL_2. Even if the shape of the boundary layer if different, the vorticity flux is equal if the velocity just outside the boundary layer U_s is equal for both. BL_2 is the shape of the boundary layer if there is only one cell in the boundary layer in the CFD calculations. BL_1 is the real boundary layer.

Three conditions still need to be fulfilled to capture the behavior of the flow:

1. The cells in the wake close to the plate is small enough, to resolve the large-scale vortices behind each cylinder.
2. The cell size is in the same order as the thickness of the boundary layer. This is required in order to obtain correct velocity outside the boundary layer at the corner.
3. A minimum of two cells between the cylinders to allow fluid flow through the openings in the plate.

5.3 Mesh Sensitivity Analysis

A mesh parameter sensitivity analysis was done. The domain size, cell stretching, and cell size were varied. A minimum of 2 cells between each cylinder is required to have a fluid flow between the cylinders. The different meshes that were tested are summarized in Table 5.1. Figure 5.5 and Figure 5.6 show small dependency of the mesh parameters. The mesh that is the most different from the others is mesh 1, which is the finest of the meshes. It was found that calculations carried out on this mesh was in the closest agreement with the experiment. However, the computational cost of this mesh is too high, and the other meshes yield good results. Mesh 7 is chosen as the mesh where the results for the bi-chromatic motions are calculated. The mesh is shown in Figure 5.7

and Figure 5.8. Mesh 4 yielded similar results as Mesh 1, and one reason for this can be that that the plate-end vortices are better resolved due to less cell stretching. Thus Mesh 4 has a finer mesh in the region closer to the plate compared with the meshes that have a higher stretch. The number of cells is larger on Mesh 4 compared to Mesh 7, and the precision that is gained is not enough to justify the extra computational time that is needed with the limited time frame of this thesis. The results are done on Mesh 7, both for the solid plate and the perforated plate. A large domain is needed in order to make sure that the boundary conditions of the domain boundaries do not affect the flow close to the plate.

Table 5.1: Mesh details for the different meshes. The first column to the left contains the names of the meshes. The column "Min. Cell Size" contains the size of the cells close to the plate. "Domain Size" is the total dimension of the computational domain. "Num. of Cells" is the total number of cells in the computational domain. "Max Aspect Ratio" is the maximum aspect ratio of the cells in the domain, and "Stretch" is how much a cell is stretched from one cell to another when moving in the domain away from the plate. The cell is stretched until the maximum allowed aspect ratio is reached.

Name	Min. Cell Size	Domain Size	Num. of Cells	Max Aspect Ratio	Stretch
Mesh 1	1x1 mm	3x3 m	167 478	25	1.2
Mesh 2	2x2 mm	3x3 m	112 666	12.5	1.2
Mesh 3	2x2 mm	3x3 m	59 894	25	1.1
Mesh 4	2x2 mm	3x3 m	85 486	25	1.05
Mesh 5	2x2 mm	2x2 m	31 270	25	1.2
Mesh 6	2x2 mm	4x4 m	69 190	25	1.2
Mesh 7	2x2 mm	3x3 m	48 630	25	1.2

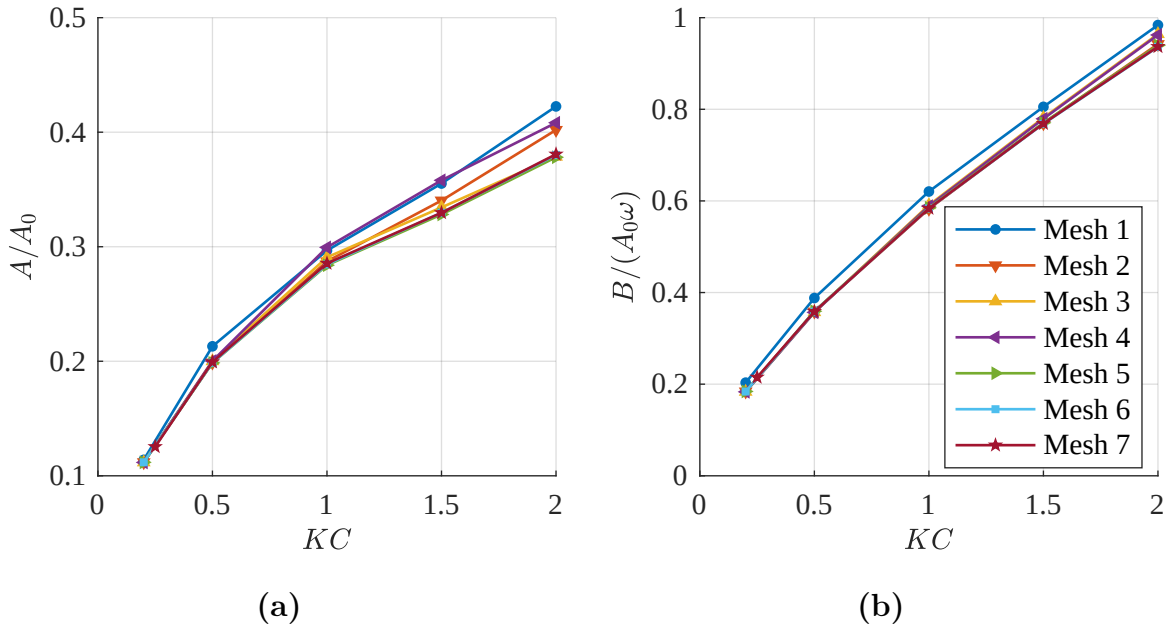

Figure 5.5: Mesh convergence for the added mass and the damping coefficients. Figure (a) is the added mass as a function of the KC number for the different meshes. Figure (b) is the dimensionless damping. Figure (a) and (b) share the same legends. Details of the different meshes are found in Table 5.1.

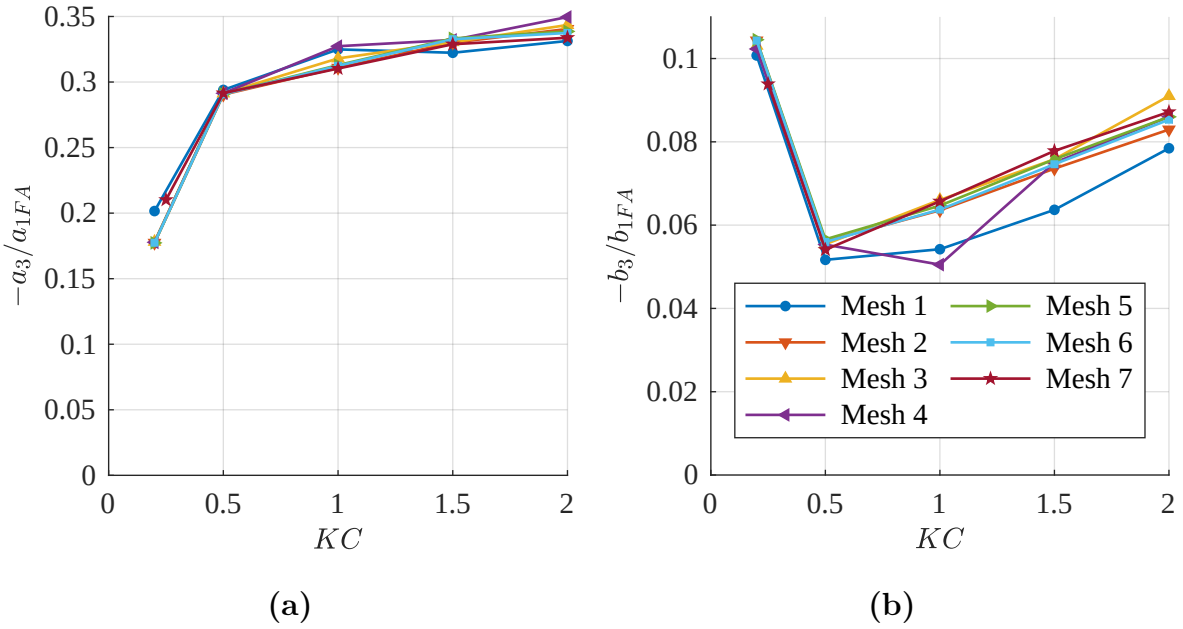

Figure 5.6: Higher order force coefficients. Figure (a) shows the Fourier coefficient fraction a_3/a_1, and Figure (b) shows $b3/b1$. The coefficients are the Fourier coefficients for the force and are defined in Section 4.3.3.

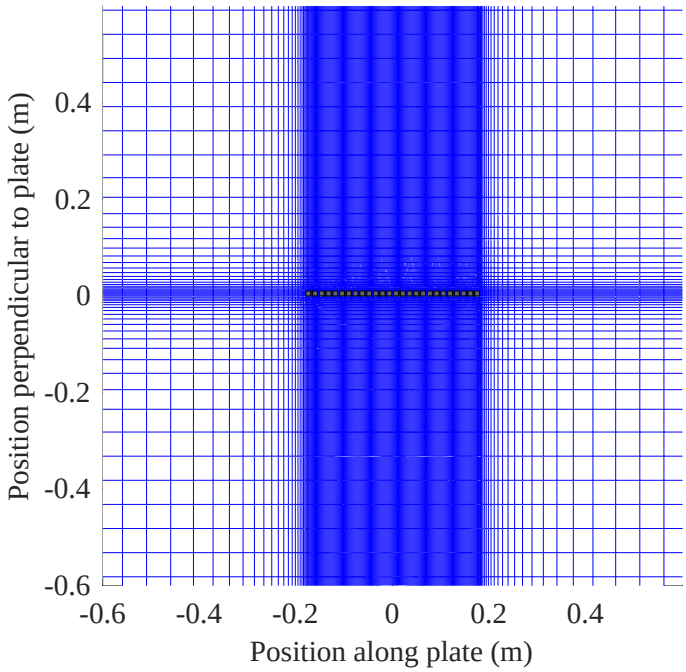

Figure 5.7: The figure shows a distant view of the final mesh to show the mesh further out in the computational domain (Mesh 7 in Table 5.1). The cross-section of the plate is placed in the center of the computational domain. Note that the whole domain is 3x3 meters. In the digital version, it is possible to zoom in for more details.

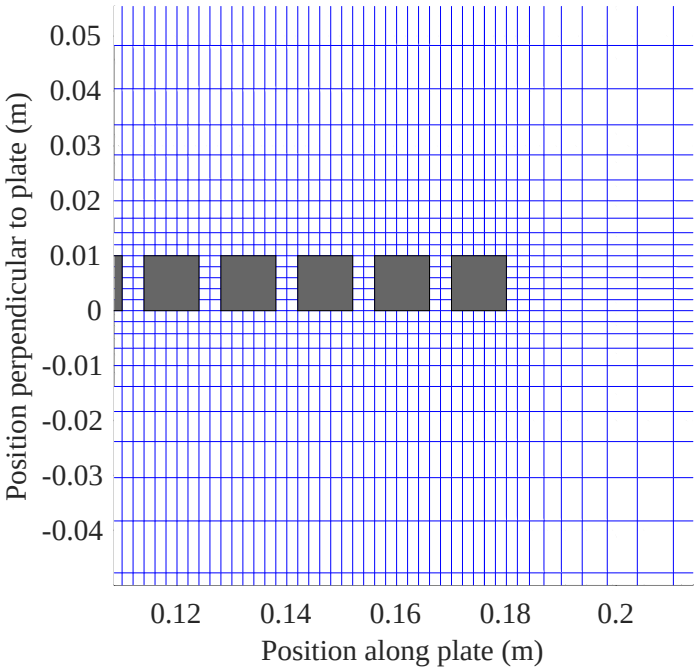

Figure 5.8: Close-up view of the final mesh (Mesh 7) at the right edge of the plate. Details about the mesh and domain can be found in Table 5.1.

5.4 Time Step Convergence

An important parameter regarding the time step is the CFL number (Courant Friedrichs Lewy number). It can be written as

$$CFL = \frac{U_{max}\Delta t}{\Delta l_{min}}, \tag{5.23}$$

were U_{max} is $\max(\sqrt{u^2 + w^2})$ in the simulation, and Δl_{min} is the length of the shortest side of the smallest cell in the simulation. U_{max} is not known a priori of the simulation. Thus, a simulation needs to be done by taking an educated guess of the maximum velocity for the first run and then checking with the simulation. Since the time marching scheme is an implicit scheme, the simulation is stable, even if the CFL number is larger than one. However, the accuracy needs to be checked, and one way of doing that is a convergence test of the CLF number. Figure 5.9 shows a small dependency of the CLF number, and convergence is reached if the CFL number is kept smaller than one. In all simulations, the time step is chosen conservatively such that the CFL number is always between 0.3 and 0.6. To ensure the high resolution of the time series is, a minimum of 200 steps per second is chosen, which is the same as the sampling frequency in the experiments.

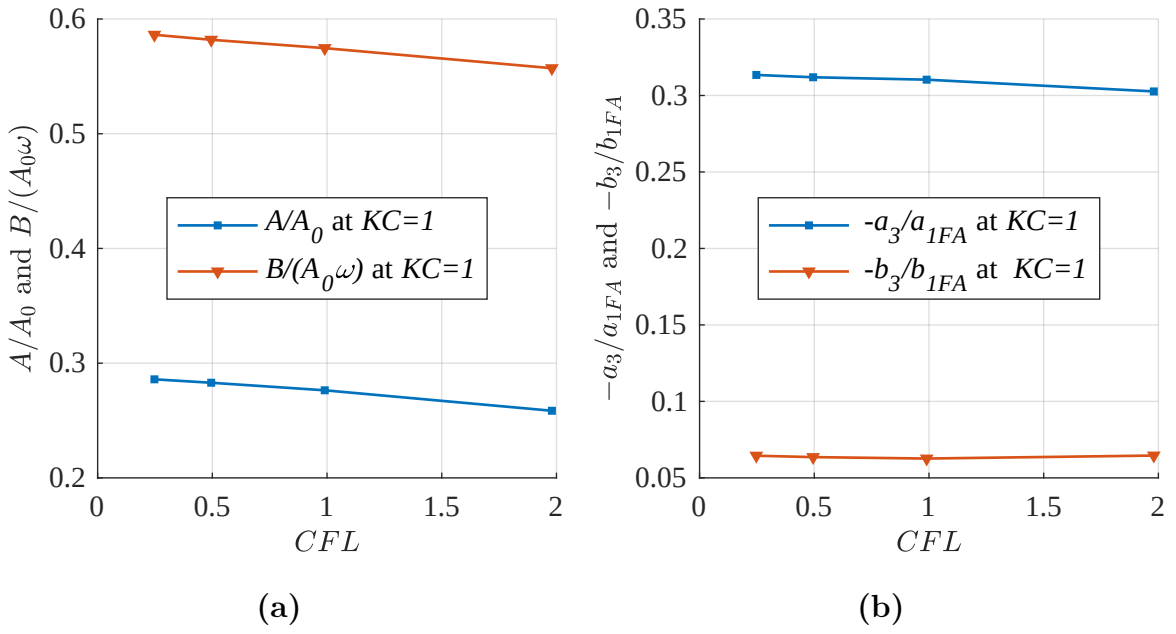

Figure 5.9: CFL sensitivity study. The CLF number is changed for Mesh 7 at KC=1. Figure (a) shows the Added Mass and Damping as a function of the CLF number. Figure (b) shows the higher-order force coefficients that are defined in Section 4.3.3. Both figures show very little sensitivity of the CLF number at KC=1. The figures show, in general, little sensitivity of the CLF number. The CLF number is defined in Equation 5.23.

5.5 Solid Plate Convergence Study

The solid plate simulations were done for KC=0.78 to see if the larger added mass for the bi-chromatic motion named BiChr 7 in Table 3.2 was an effect of plate perforation. A convergence test was done for KC=1 for the domain size and KC =0.78 for the cell size. The solid plate has the same dimensions as S28, but the perforation ratio is 0. Figure 5.11 and Figure 5.12 shows that the results are not sensitive for changing the mesh. Thus, Mesh 7 is also used for solid plate simulations. The time step is the same as in the perforated plate simulations. Velocities for the solid plate are smaller than for perforated plates because the highest velocities are through the plate openings. Thus, the time step will be conservative for solid plates. Figure 5.10 shows the mesh for the solid plate.

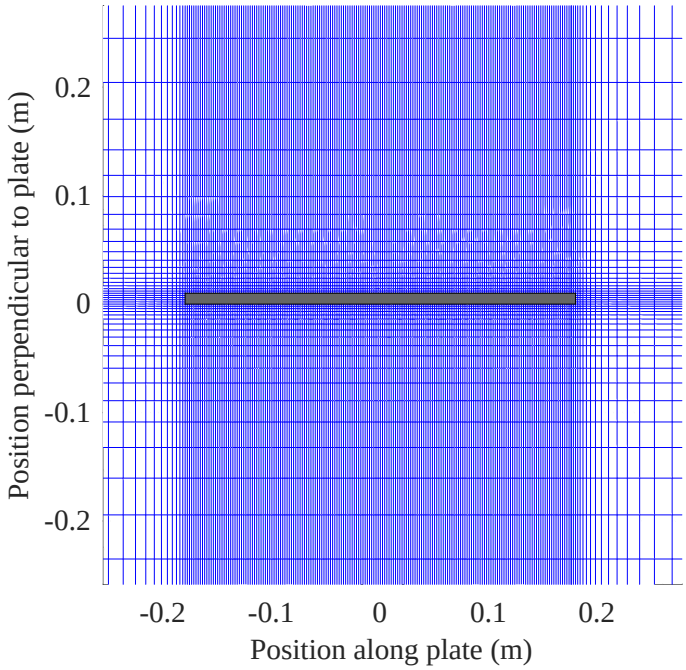

Figure 5.10: The figure shows a distant view of the final mesh and solid plate that is used to perform the CFD analysis on the solid plate. The mesh that is used is also Mesh 7. For more details of this mesh see Table 5.1

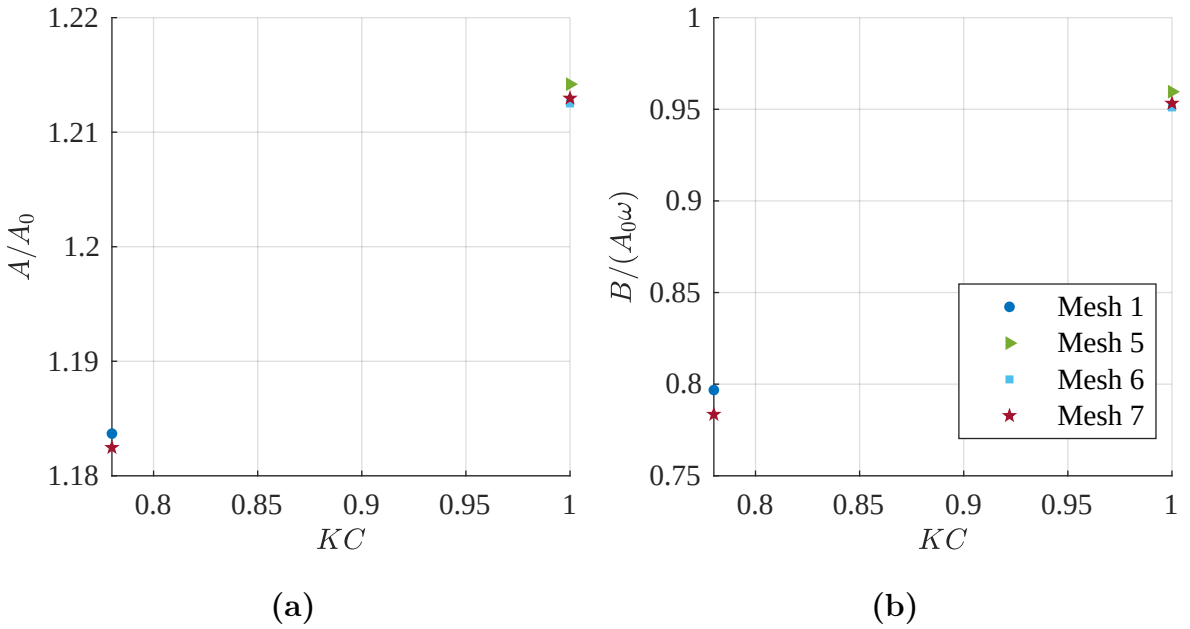

(a) **(b)**

Figure 5.11: Mesh convergence for the added mass and the damping coefficients for the solid plate. Figure (a) is the added mass for the different meshes. The x-axis shows for which KC number it was tested. Figure (b) is the dimensionless damping. Figure (a) and (b) share the same legends. Mesh 5,6 and 7 have equal cell size but different domain sizes of 2x2m,4x4m, 3x3m, respectively. Mesh 1 and 7 have equal domain size but a minimum cell size of 1x1mm and 2x2mm, respectively. More details of the different meshes are found in Table 5.1. The figure shows that the coefficients are almost independent of the mesh. Mesh 1 was tested on KC=0.78. Mesh 5, Mesh 6 was tested on KC=1. Mesh 7 was tested on both KC numbers.

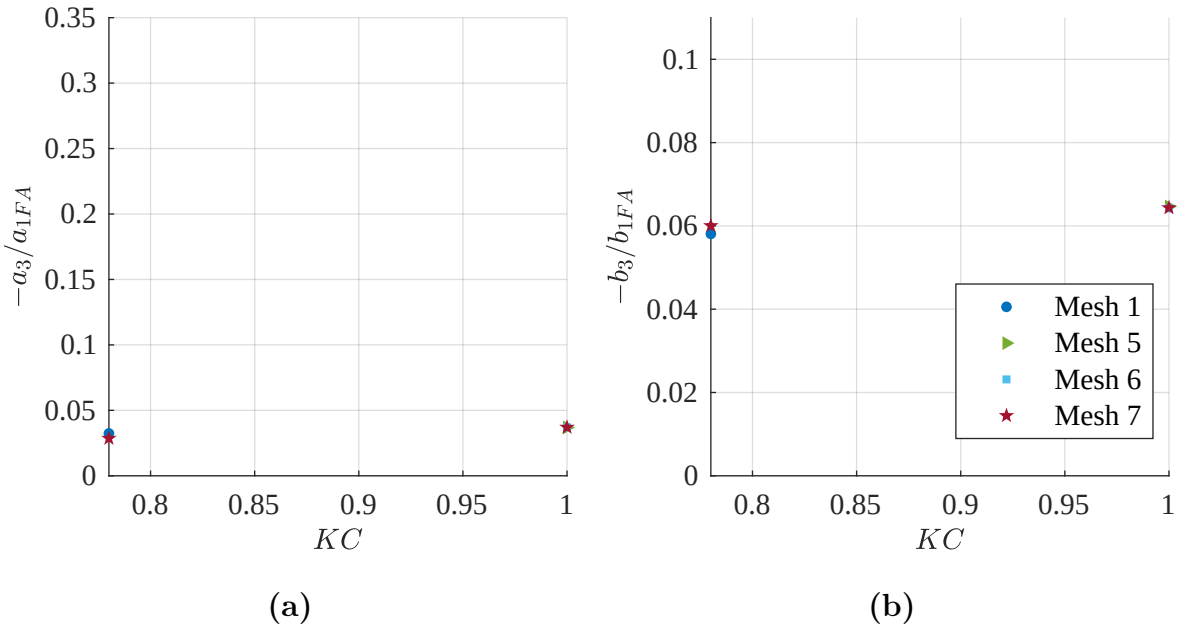

Figure 5.12: Mesh convergence for the higher-order force coefficients, which is defined in Section 4.3.3. Figure (a) and (b) share the same legends. The figures show that the coefficients are almost independent of the mesh. It also shows that higher-order harmonics are not important for a solid plate for tested KC numbers.

5.6 CFD Visualization

Some flow visualization is done for plate S28 to understand the major differences between Mesh 1 (1mm cells) and Mesh 7 (2mm cells) from Table 5.1. The added mass was slightly underpredicted for Mesh 7 compared to Mesh 1 and the experiments for KC=2, which Figure 6.2 shows. Figure 5.13 suggests that a candidate for this underprediction is that the vortices behind each cylinder are not fully resolved for Mesh 7 at KC =2. However, the damping is expected to be dominated by the plate-end vortices, which can be seen in Figure 5.14 Consequently, the damping is less sensitive to the mesh size because the plate-end vortices are much larger than the vortices behind each cylinder. The results of Mesh 4 (2 mm cells and less stretching compared to Mesh 7) also suggests that less stretching of the cells yields more accurate results for the added mass. However, the gain in accuracy is considered less than the extra computational cost. Mesh 7 yields results that agree well with the experiments in the computed KC range.

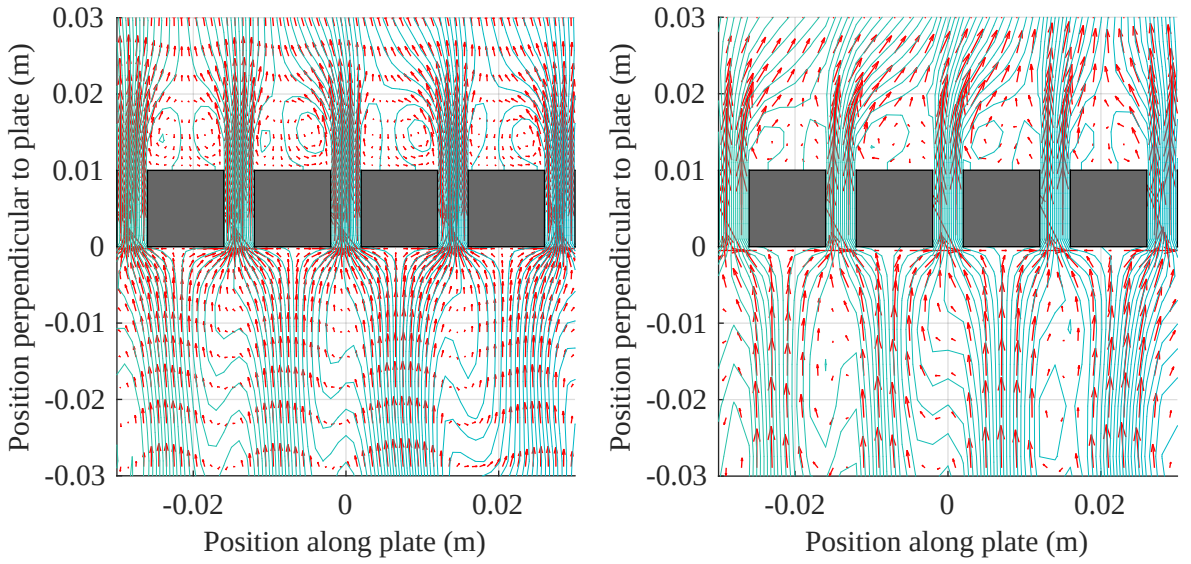

(a) Mesh 1 **(b)** Mesh 7

Figure 5.13: Visualization of the flow near the square cylinders when the acceleration is at its maximum, and the velocity is zero. Some details are lost for the coarsest mesh (mesh 7), and it is a candidate for why the added mass is underestimated for the coarser mesh at $KC = 2$. (a) Mesh 1 and (b) Mesh 7. Figure (a) and (b) shows equally spaced levels for the stream function were the same levels are plotted in both figures, such that they compare.

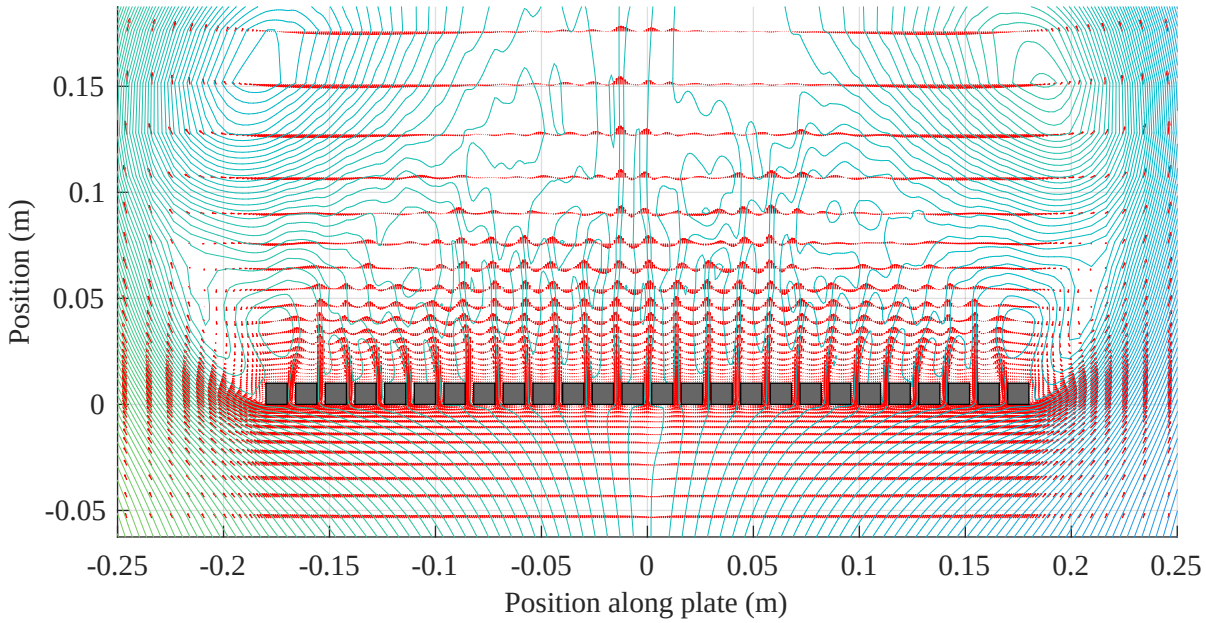

Figure 5.14: The figure shows streamlines for KC=2. Large plate-end vortices dominate the damping, and thus the damping is less sensitive to the mesh size. The time is 0.4T into a regular oscillation cycle of a cycle where the velocity is at its maximum at 0.25T and 0.75T.

5.7 Turbulence

The code is a 2D laminar code and does not take the effect of turbulence into account. Turbulence is a 3D phenomenon in fluid flows. The transition into turbulent flow is due to the unstable nature of high Reynolds number flow. However, turbulence in the flow can be important. Turbulence will have two major contributions that will change the flow:

1. Change of the boundary layer velocity profile and boundary layer thickness
2. Increase of the energy dissipation rate

Since the corners are sharp, item number 1 is not waited to be of importance. However, the wake is turbulent, and because of the oscillatory flow, the wake will return over the plate. Thus, the turbulence level in the wake can influence the forces on the plate. The Reynolds number is an important parameter, also in turbulent flow and is

$$Re = \frac{ul}{\nu}, \tag{5.24}$$

where u and l are characteristic velocity and length, respectively. For $KC = 2$ with T=2, the Reynolds number becomes 1.3e5 if the characteristic length is the plate width, and the characteristic velocity is the free stream velocity amplitude. For model S28, the local Reynolds number for the cylinders will be approximately $1/\tau = 3.57$ larger than the free stream velocity. $1/\tau = 3.57$ is based on a mass balance though the plate and neglecting that the water is allowed to flow around the plate. If the characteristic length is based on the cylinder members and the local flow between the cylinders, we get a Reynolds number of approximately 1.2e4. Since the Reynolds number is high, it is expected that the wake becomes turbulent.

In turbulence theory, it is common practice to use scaling laws in order to get some insight into the effect of turbulence. Two important scaling laws are viscous- and turbulent energy dissipation in the flow. Turbulent dissipation is also due to viscous effects, but the processes of turbulent dissipation are due to energy transfer from larger to smaller vortices, where the kinetic energy ultimately transforms into heat due to viscosity. An important parameter in the cascade of turbulent energy is the so-called vortex stretching, which is a fully 3D effect (Tennekes and Lumley, 1972). The turbulent dissipation rate of the vortices in the wake scales as u^3/l while the viscous dissipation scales as ν^2/l^2 (Tennekes and Lumley, 1972). Here u and l are characteristic length and velocity in the wake. This means that an estimate of the ratio of turbulent and viscous dissipation rate scale as

$$\frac{E_{turbulent}}{E_{viscous}} = Re \tag{5.25}$$

For the case of the tested perforated plates, the ratio of turbulence and viscous dissipation, even for the small vortices behind each cylinder, is in the order of many thousands. This

dissipation due to turbulence is not taken into account in the solver. Thus, experimental results are important to validate the results from the CFD and to see if the assumption to neglect the effect turbulence has on the flow field holds for the KC numbers under consideration. Mentzoni (2020) did a sensitivity analysis on the viscosity, and from this analysis, he found that the solver was not sensitive to the value of the kinematic viscosity unless for very small Reynolds numbers where wall friction started to be of importance.

Also, the assumption of 2D flow needs to be validated by experiments. Even though the experimental setup is close to 2D, 3D effects in the flow due to instabilities and turbulence may occur. The experiments and CFD agree well for both plates. Thus, the assumption of negligible influence of turbulence and 3D effects in the flow holds for these models and scales. However, large scale experiments of perforated structures lack in the literature and is an area of further research. An interesting parameter regarding large scale tests for the perforated plate is the turbulent dissipation rate. This parameter can be assessed by assuming that the kinetic energy of the large scale vortices in the wake scales as ρu^2 per unit volume, and the rate of transfer of energy to the smaller vortices, called the energy cascade, is proportional to u/l for a turbulent flow. As an estimate, the length scale l is assumed to be the width of the flow (Tennekes and Lumley, 1972). Over one period, the large scale vortices in the wake have lost an amount of energy to smaller vortices as $\rho u^3 T/l$ per unit volume. By dividing this by the kinetic energy of the large scale vortices in the wake, we obtain a parameter that is uT/l. This is recognized as the KC number. This simple analysis suggests that an estimate for the turbulent dissipation rate also scales as the KC number. However, this is an estimate under several assumptions, and thus the only way to investigate the effect of turbulent wakes of very large Reynolds numbers is to perform large scale experiments.

6 Results and Discussion for Regular and Bi-Chromatic Tests

6.1 Results for Regular Forced Oscillations and Comparison with CFD

The hydrodynamic coefficients from the regular experiments and CDF calculations are presented in Figure 6.2 and Figure 6.3. The regular forced oscillation tests were done to obtain curves that were later used in the irregular calculations. Error bars are included in the figure. The error bars are the standard deviation of the hydrodynamic coefficient under consideration and a measure of the variation from cycle to cycle. The coefficients are obtained by the use of Fourier averaging. The coefficients are close to independent of the period of oscillation, and the larges difference was seen in the added mass. The difference in the period is considered small. Both the free surface and the rig setup are candidates for this period dependence in the added mass.

Generally, good agreement is found between the lab experiments and the CFD calculations. The damping is somewhat overestimated in the CFD, and the added mass is underestimated in the CFD, especially for the coarsest mesh. The differences are small, so it is hard to point on specific reasons for this. However, one important difference from the experiments is that CFD calculations are done in 2D without turbulence modeling. The wake is expected to be turbulent in the model tests as the Reynolds number is high. Thus, we expect the wake to have some degree of turbulence, which could affect the results. However, the CFD results show that good results are obtained from CFD by neglecting the turbulence and 3D effects of the flow for plate S28. This means that the CFD results strengthen the lab results for both plates. The lab results confirm that turbulence can be neglected for the investigated KC numbers and Reynolds numbers.

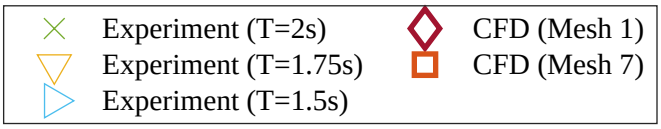

Figure 6.1: Legend for Figure 6.2 and Figure 6.3. Mesh 1 has a minimum cell size of 1x1mm and mesh 7 has a minimum cell size of 2x2mm.

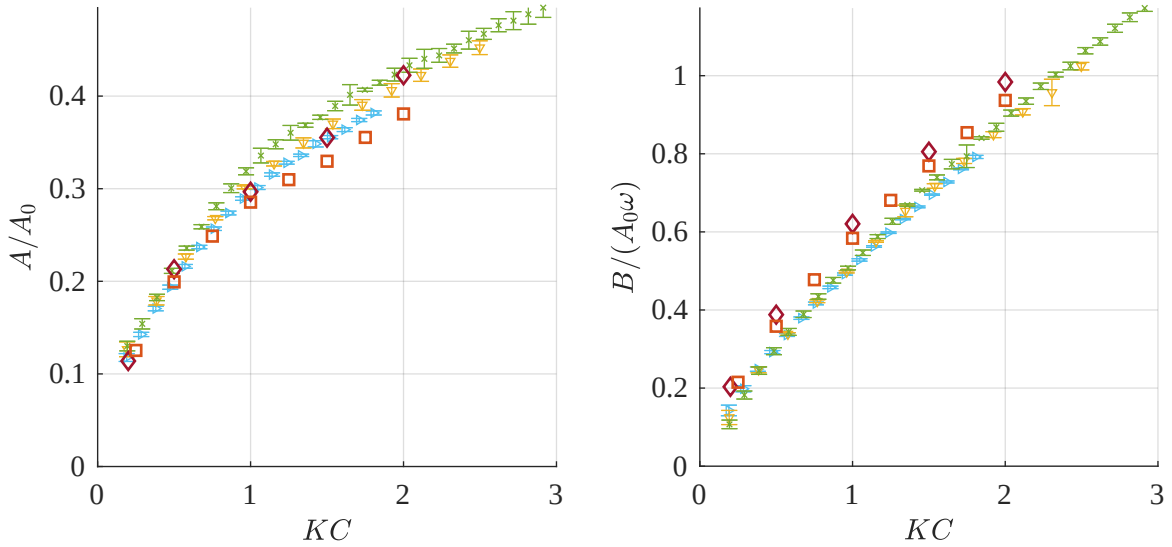

(a) **(b)**

Figure 6.2: Normalized hydrodynamic force coefficients for S28. (a) Normalized added mass and (b) normalized damping.

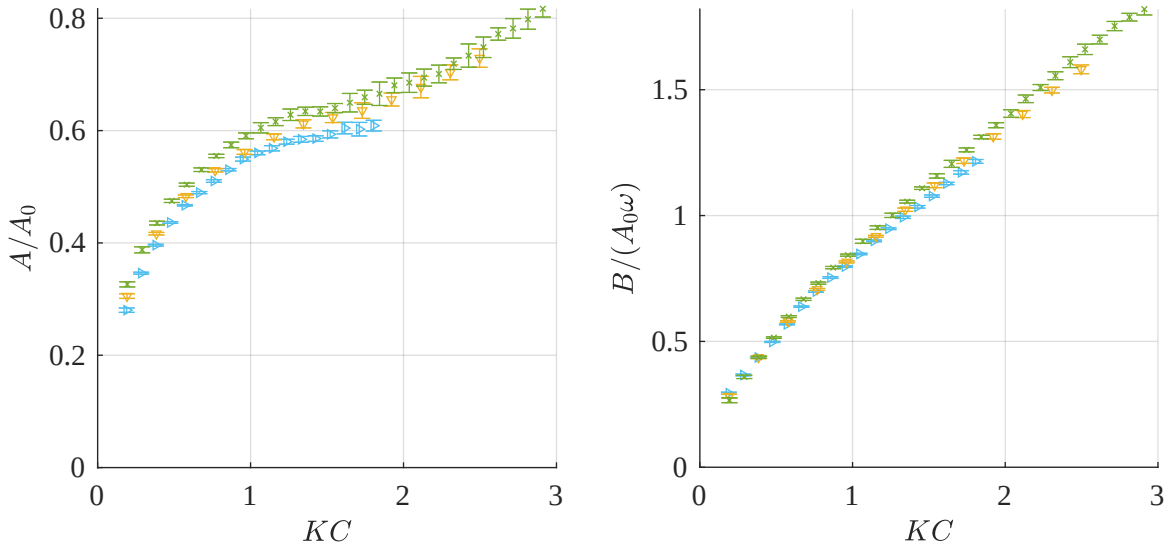

(a) **(b)**

Figure 6.3: Normalized hydrodynamic force coefficients for S19. (a) Normalized added mass and (b) normalized damping.

6.2 Wave Radiation Damping

Since there were observed radiated waves during the experiments, the damping from the waves is calculated to be ensure they can be neglected. This is done for the regular tests. The damping can be found by time-averaging the far-field radiated waves and the force on the body due to the radiated waves (Faltinsen, 1990). By doing this, the wave radiation damping becomes

$$B_w = \frac{4c_g E_w}{\omega_{osc}^2 \eta_a^2}, \tag{6.1}$$

were c_g is the group velocity, ω_{osc} is the circular frequency of the force oscillations, and η_a^2 is the amplitude of the oscillation.

Newman (1977) gives the equations for water waves at the intermediate water dept, and all the equations regarding the water waves in this section are found from his book. The mean energy in the waves in the tank is not dependent on the water depth, and is

$$E_w = \frac{1}{2}\rho g \zeta_a^2 L \tag{6.2}$$

were ζ_a is the amplitude on the radiated waves, and L is the plate length.

For a wave with period 2 seconds, the wavelength in deep waters is 6.25 meters, but the tank is only 1 meter deep. Thus, deep water wave approximation does not hold, and the equations for intermediate water depth need to be used. The group velocity is dependent on the wavelength, λ, and since we have intermediate wave dept for the waves that are radiated the group velocity is

$$c_g = \frac{1}{2}c_p \left(1 + \frac{4\pi h}{\lambda} \frac{1}{\sinh\left(\frac{4\pi h}{\lambda}\right)}\right) \tag{6.3}$$

were

$$c_p = \frac{\lambda \omega_w}{2\pi}. \tag{6.4}$$

Here ω_w the circular frequency for the wave and h is the depth. For intermediate waters, Equation 6.5 has to be solved numerically to find the wave length.

$$\lambda = \frac{g}{2\pi}\left(\frac{2\pi}{\omega}\right)^2 \tanh\left(\frac{2\pi}{\lambda}\right) \tag{6.5}$$

The wave height was found by using the fast Fourier transform of the wave signal of wave probe 6 (WP6 in Figure 3.1).

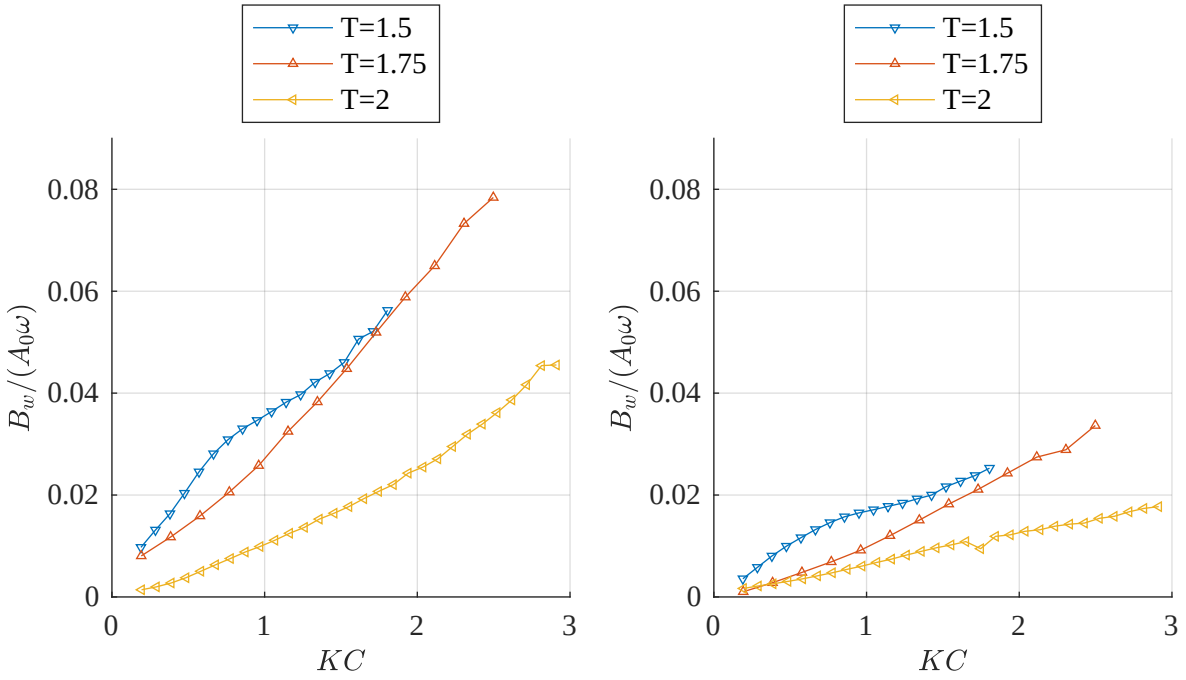

(a) Plate S19. **(b)** Plate S28.

Figure 6.4: Normalized wave radiation damping for regular plate oscillations, and normalized with respect to the plate dimensions. (a) Plate S19 and (b) Plate S28.

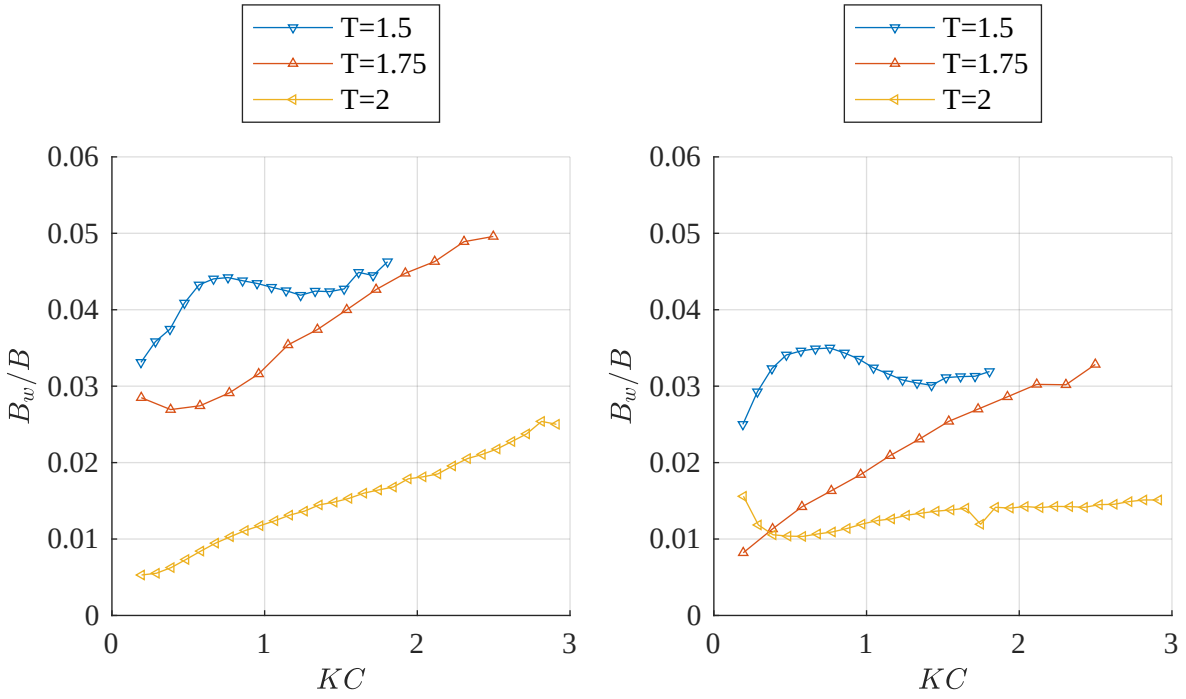

(a) Plate S19 **(b)** Plate S28

Figure 6.5: Wave radiation damping for regular forced oscillations as fraction of the total damping B for both models. The figure shows that a very small portion of the damping is from radiated waves. (a) Plate S19 and (b) Plate S28.

Figure 6.4 shows the wave radiation damping normalized to the plate dimensions and the frequency of oscillation. Figure 6.5 shows the wave radiation damping as a fraction of the total damping. The figures show that the damping from the waves is small for both models and that the wave radiation damping never becomes larger than 5% of the total damping. Thus, the assumption that the plate is far enough from the free surface to assume deep water oscillations is considered valid for these experiments in the tested KC range.

The far-field wave approximation needs some attention since the wave probes are placed close to the plate. There was found a $3\omega_w$ wave component in the signal. However, the amplitude of this signal was always less than one half of the ω_w waves' amplitude. Also, the group velocity of the $3\omega_w$ wave is approximately $1/3$ of the ω_w waves' group velocity. Consequently, the energy transportation rate of the $3\omega_w$ wave will always be lower than $1/12$ of the ω_w wave. With these arguments, the results from these tests are considered valid even though the wave probes were placed close to the model.

6.3 Third-Harmonic Forces

Morison et al. (1950) suggested that the forces of vertical piles in waves can be decomposed into an inertia term proportional to the acceleration and a drag term proportional to the square on the velocity. The Morrison load model is used with great success in a large range of KC numbers, both for normal flat plates and cylinders. However, the Morrison load model is built on the assumption that the forces' third-harmonics are in phase with the velocity. For the definition of the coefficients in this section, see Section 4.3.3.

For regular motions, the Morrison load model will yield very close results to the measured data when a_3=0 and b_3/b_1=-0.2. This can be shown by evaluation the Fourier series of $sin(\omega t)|sin(\omega t)|$. This will yield a_n=0 for all n, $b_1 = 8/(2\pi)$, $b_2 = 0$ and $b_3 = -8/(15\pi)$. There is some small contribution from higher-order odd numbers b_n, but they are small compared to the first and third-harmonics. From Figure 6.7, we can conclude that a quadratic damping model, as in Morrisons load model, should not be used uncritically, especially for the lowest KC numbers in the figure. For the tested perforated plates, a large part of the third-harmonics is in phase with the acceleration, especially for S28. However, it is interesting to see that the third-harmonic for S19, $-b3/b3$ goes towards 0.2, which is the factor that is assumed in the Morrison load model. The same trend can be seen for S28, but it goes slower towards 0.2. The figure shows that CFD calculations for S28 are in agreement with the results from the experiments and show the same trend for the third-harmonics.

For marine operations, the force impulse is the crucial parameter. It is the impulse that determines the responses of the lifted object. The third-harmonic force impulse is small due to their narrow peaks. The third-harmonics can be significant if fatigue is a concern. However, fatigue from hydrodynamic forces is not considered as a problem for marine operations. In the rest of this thesis, the forces are calculated by only assessing the first-harmonic hydrodynamic coefficients, i.e., the damping B and the added mass A.

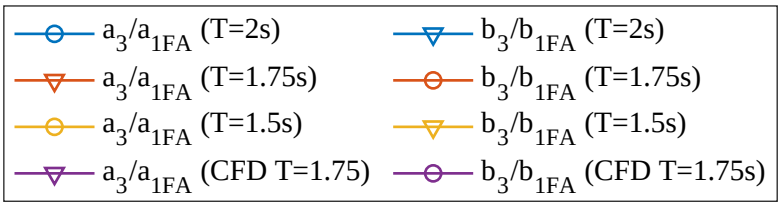

Figure 6.6: Legend for Figure 6.7

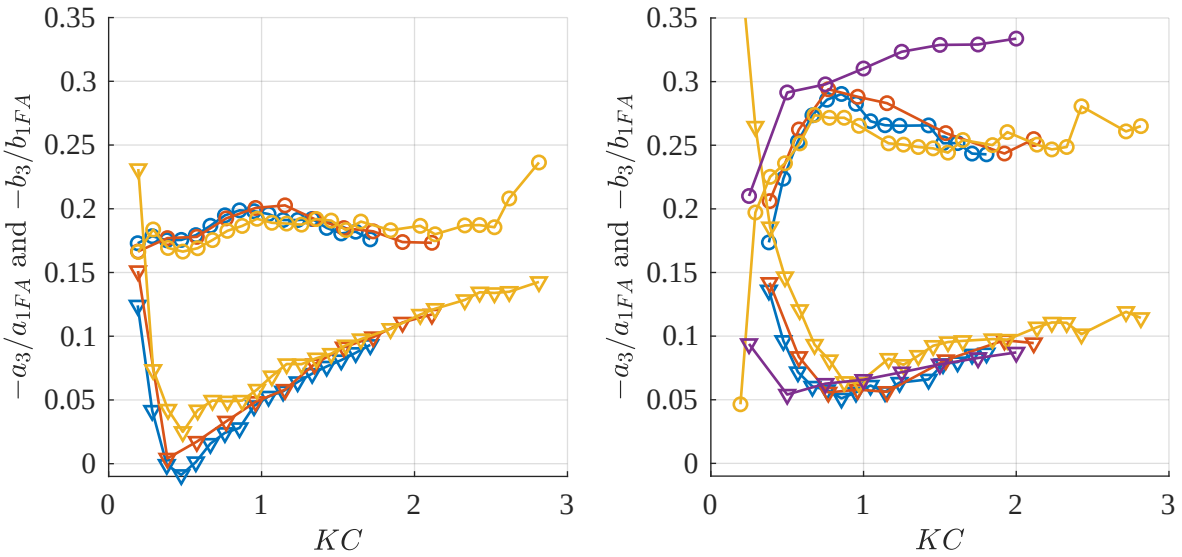

(a) S19 **(b)** S28

Figure 6.7: The third-harmonic Fourrier coefficient as a fraction on the first-harmonic Fourier coefficient. a_{1FA} and b_{1FA} is found from Fourier averaging, while a_3 and b_3 is found from a function in Matlab called fourier8. The time series are aligned such that $-a_1/(\omega^2 A_0 \eta_a)$ corresponds to C_A and $-b1/(\omega^2 A_0 \eta_a)$ becomes C_B. The CFD calculations are in good agreement with the experiments, although they are somewhat higher. (a) Plate S19 and (b) Plate S28.

6.4 Results for Bi-Chromatic Motions

In this section, the hydrodynamic coefficients for the bi-chromatic motions are presented. Figure 6.9 contains the normalized damping coefficients for the bi-chromatic runs. The damping coefficients show a clear pattern when sorted for KC_i/KC_{i-1} and plotted against the KC number for the present half-cycle, which is KC_i on the x-axis. The damping is smaller than for regular cycles for half cycles when the previous amplitude of the half-cycle is smaller than the present. The damping is larger if the previous amplitude is smaller than the previous. This was found for all the tested bi-chromatic motions. No clear pattern was found for the added mass, but the added mass is always close to or lower than for regular oscillations, with one exception, and this is recognized as a start-up effect. The start-up effect is discussed in detail in Section 6.4.2.

KC_i/KC_{i-1} was chosen as the parameter to sort the data, because the KC number is connected to the circulation of the free shear layer that is shed during a half cycle, and thus this parameter will be a measure of the velocity that is included from the vortices from the previous half cycle. Also, there was an attempt to sort the data as $KC_i^2/KC_{i-1}^2 \cdot \omega_i/\omega_{i-1}$ to take the change of the period from one cycle to another into account. Generally, the period should be taken into account since the period changes the circulation of the previously formed vortex, and the rate of change of the vortex circulation is proportional to U_s^2 as shown in Section 5.2.2, were U_s is the velocity just outside the boundary layer at the point of separation. If a single half-cycle is evaluated where the vortices from the previous half cycles are neglected, the circulation of the shed vortex during a half cycle is proportional to $U_a^2 T$. This also assumes the high Reynolds number approximation, which means that we can use potential flow outside the boundary layer, which in turn means that U_s is proportional to U_a, were U_a is the free stream velocity. Thus, we can imagine that a measure of the circulation of the plate-end vortex shed for the previous half-cycle is KC_{i-1}^2/T_{i-1}. This is a simplification of the reality, because the vortex formed in one half-cycle is also dependent on the induced velocity from the previously formed vortex due to an increase in U_s from the previously formed vortex. However, the simplification serves a qualitative explanation of why the data sorts nicely out for the damping and dimensionless force amplitude by the parameter KC_i/KC_{i-1}. The Figure 6.9 and Figure 6.11 shows that there is a clear trend in this parameter. From these figures, it is concluded that it is enough to only take the previous half cycle into account when the hydrodynamic forces are calculated in a time series.

In Figure 6.9 and Figure 6.10 error bars are included to show the variation on the coefficients for identical half cycles by the standard deviation. This can be done for a bi-chromatic time series since the pattern of motion repeats itself. Generally, the error bars show that there are small variations. For some series, one could only obtain one repeating half-cycle in the position, and these are removed from these figures. The removed data points were not in conflict with any of the conclusions that can be drawn for the figures, but when comparing the method of least squares to Fourier averaging for the regular series, it was found that there can be some spread from half-cycle to half-cycle due to variations in the flow also for the regular oscillations, and thus averages should be used.

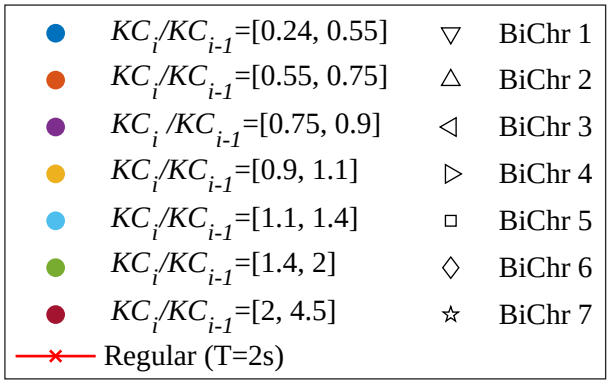

Figure 6.8: Legend for Figure 6.9, Figure 6.10, Figure 6.11 and Figure 7.1. KC_i/KC_{i-1} is divided into intervals and each color denotes one interval. Different markers are also included, mainly to show the start-up affect in the added mass for BiChr 7 in Figure 6.10.

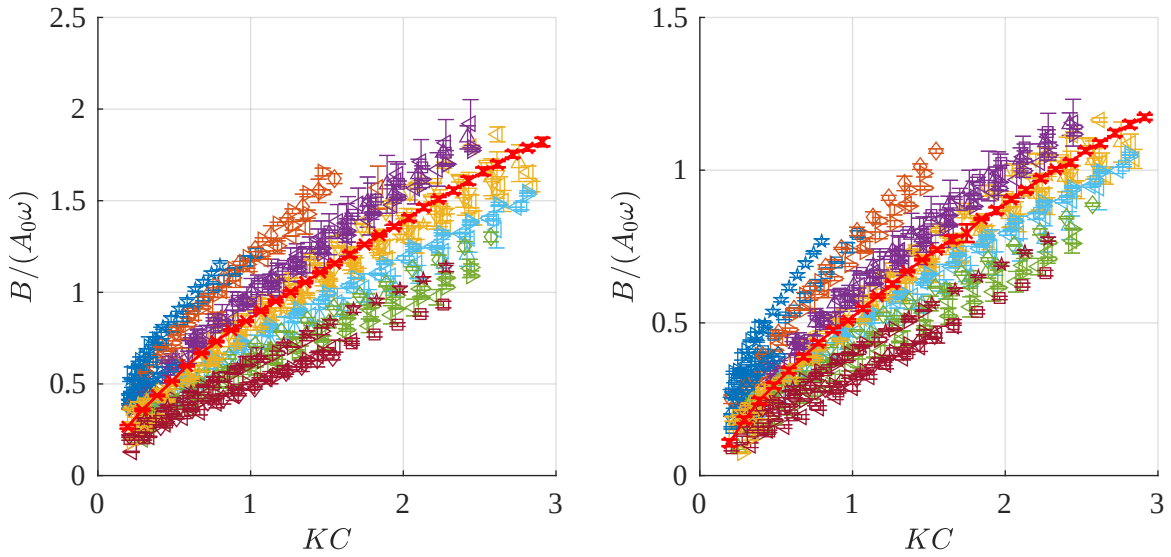

(a) Plate S19 **(b)** Plate S28

Figure 6.9: Normalized damping coefficient for the bi-chromatic tests. This figure is included to show that the coefficients have a clear pattern when sorted by KC_i/KC_{i-1}. This is utilized in Section 7.1.4, where these data is used to calculate irregular time series. (a) Plate S19 and (b) Plate S28.

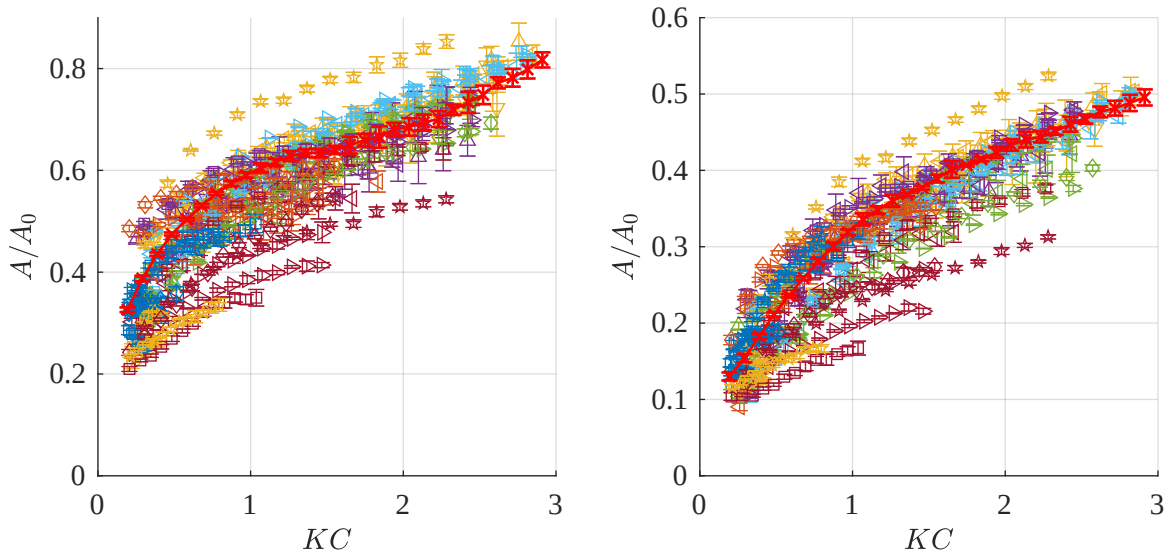

(a) Plate S19 **(b)** Plate S28

Figure 6.10: Normalized added mass coefficient. This figure is included to show that the coefficients are spread, and no particular pattern is found. However, most of the coefficients are close to the regular curve, or below. One exception is the yellow star markers, which are from the BiChr 7 set. This larger added mass is recognized as a start-up effect, which is discussed in Section 6.4.2. (a) Plate S19 and (b) Plate S28.

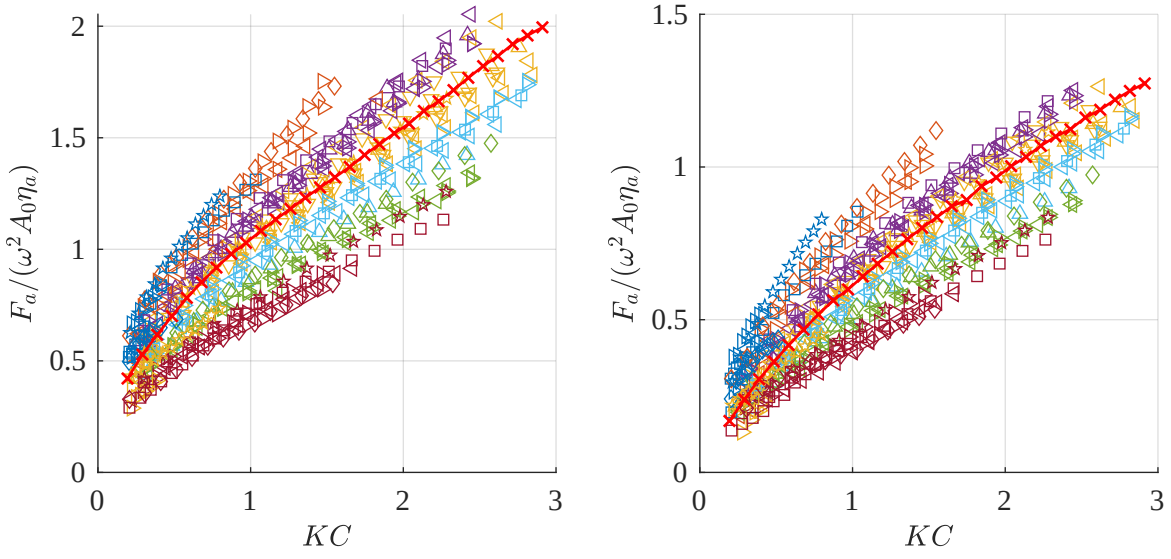

(a) Plate S19 **(b)** Plate S28

Figure 6.11: Normalized force amplitude coefficient. This figure is included to show that the force amplitude sorts even better than the damping when sorted with KC_i/KC_{i-1}. Consequently, the start-up effect in the added mass can be neglected if the important parameter is the force amplitude. Larger figures are provided in Appendix B in order to see that the yellow star markers are close to the regular curve for the force amplitude. (a) Plate S19 and (b) Plate S28.

6.4.1 Comparison of CFD and Experiment

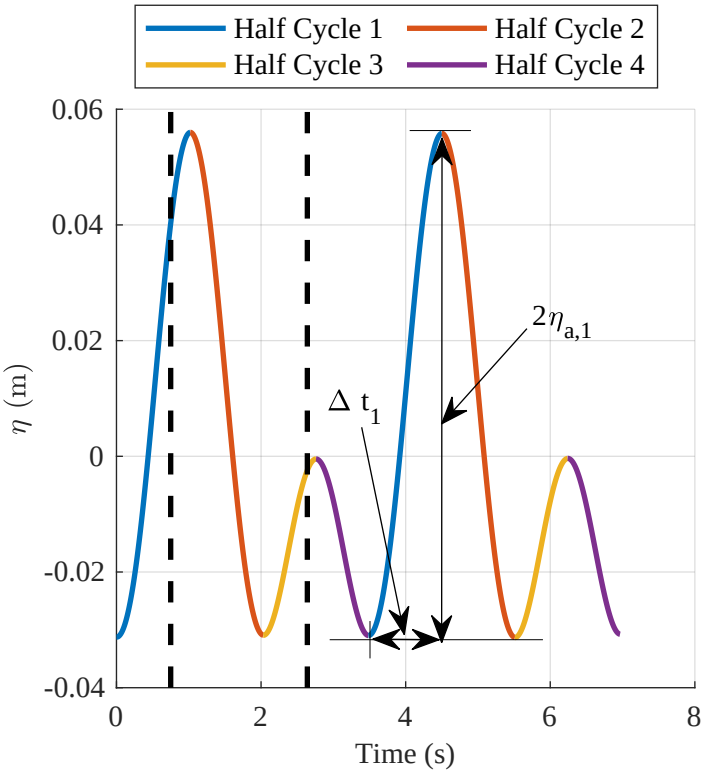

Figure 6.12: Definitions of half cycles for BiChr 7. Each half-cycle is assigned to different colors. The start-up effect for the added mass was identified for half-cycle 2. The vertical dotted lines correspond to the vertical dotted lines Figure 6.15.

Computations were performed for BiChr 7 on Mesh 7 for S28. Mesh 7 was used since it showed results that were in good agreement with the experiments, and it was not as computational demanding as Mesh 1. However, the added mass was found to be slightly smaller for Mesh 7 compared to Mesh 1, but for this project, Mesh 1 was too computationally demanding. Figure 6.14 shows that the same trends can be seen in CFD and experiments for BiChr 7. However, the added mass is underpredicted in the CFD, which is as expected if we are returning to the discussion of mesh convergence in Section 5.3. The CFD results strengthen the assumption that the empty rig can also be subtracted in bi-chromatic and irregular time series. Also, the assumption that the free surface can be neglected for bi-chromatic tests holds.

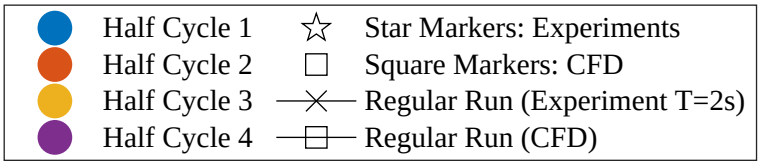

Figure 6.13: Legend for Figure 6.14 and Figure 6.16. The half cycles for BiChr 7 is defined in Figure 6.12

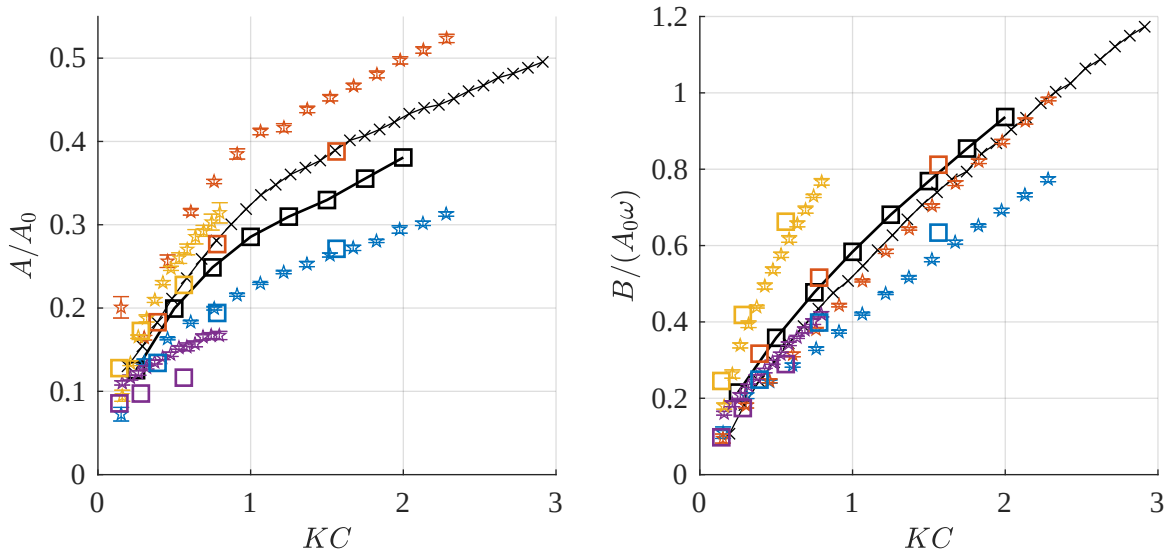

(a) **(b)**

Figure 6.14: Comparison of CFD and experiment for BiChr 7 on plate S28. Legend is found in Figure 6.8. The same trends for CFD and experiments are found for the damping and the added mass for all half-cycles, but the added mass is shifted down, and the damping is shifted up for the CFD results compared to the experiments. The reason for that the added mass is shifted down is because that Mesh 7 underestimates the added mass as discussed in Section 5.6. Legend is found in Figure 6.13. (a) Normalized added mass and (b) normalized damping.

6.4.2 Start-Up Effect for Added Mass

In certain conditions, the added mass increased by 20-25 % in the bi-chromatic tests even if the previous swing had the same amplitude as the present. This happened for all tested KC numbers for one particular bi-chromatic motion, namely BiChr 7. This motion has two small equal half amplitudes and two equally large half-cycle amplitudes. Because of two small half-cycle amplitudes and two large, this motion creates a similar situation when regular motions start in a still fluid. The finding of increased added mass relative to the regular test added mass is consistent with the findings of Ikeda et al. (1988). From the discussion in Section 1.2 of the results of Ikeda et al. (1988), it was found that the

start-up effect did not increase the total force amplitude as the drag force decreased more than the added mass force increased.

A CFD run for a solid plate case was done to ensure that the increase in the added mass was due to the perforation of the plate, not a consequence of the motion. The convergence study for the solid plate can be found in Section 5.5. The simulation was also done on the BiChr 7 motion, with $KC_2 = 0.78$. The result showed that the normalized added mass coefficient for half cycle 2 was 1.29, while the added mass for the regular case where $KC = 0.78$ was 1.23. This means that the increase in the added mass was only 5 % for the solid plate case for $KC = 0.78$ in a start-up situation. This is consistent with the findings of Ikeda et al. (1988), that did not find any significant start-up effect for $KC < 11$ for solid plates.

A time series is shown for plate S19 for $KC_2 = 0.76$ in Figure 6.15. S19 is shown since it has a higher added mass to damping ratio than S28. Figure 6.15 shows the computed time series compares to the measured time series. The corresponding time series for the position is found in Figure 6.12. The red curve is calculated with the coefficients extracted from the regular curve in Figure 6.3 and is calculated as in Section 7.1.3. The yellow curve is calculated with the calculated added mass and damping for this particular force time series by use of the discussed curve fit method. The focus of interest is what happens between the time interval between 1 second and 1.5 seconds. Figure 6.15 shows that the maximum values of the two calculated force time series are approximately equal. This is because coefficients from the regular time series have higher damping than half cycle 2 in BiChr 7. The increased added mass from the start-up effect is thus considered negligible for the case where the added mass and damping forces are approximately equal or when they are damping dominated. This is also shown in Figure 6.11 where the non-dimensional force amplitude is plotted. From this, it is concluded that for KC numbers larger than 0.76, the startup-effect is negligible for S28 and S19.

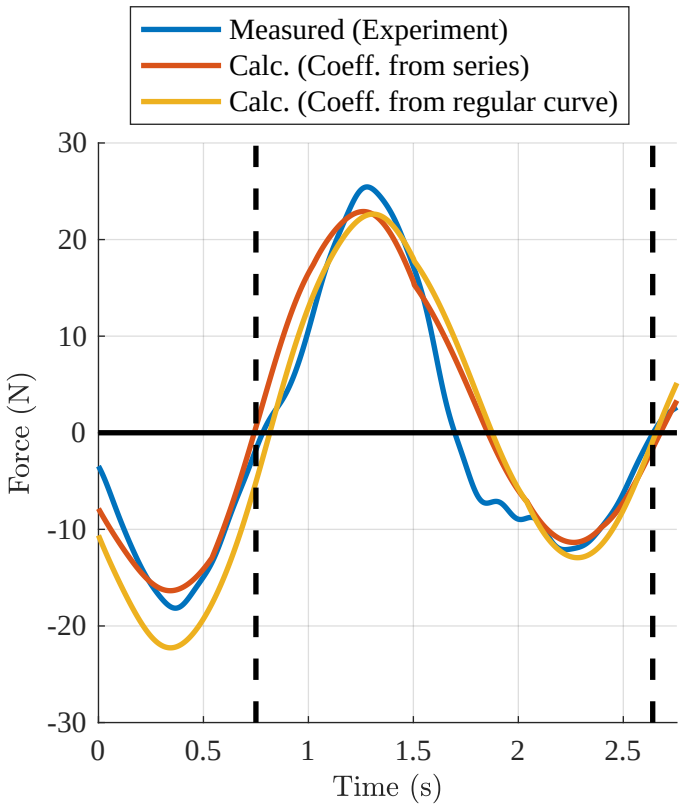

Figure 6.15: Force time series for BiChr 7 for plate S19. The force amplitude does not change much when the calculated force is based on the regular time series, compared to when the coefficients found from this particular force time series. The only change is a shift in phase towards damping when the force is calculated with coefficients from the regular curve. The corresponding position for the plate is found in Figure 6.12. The dotted vertical lines are at the same time instances as in Figure 6.12.

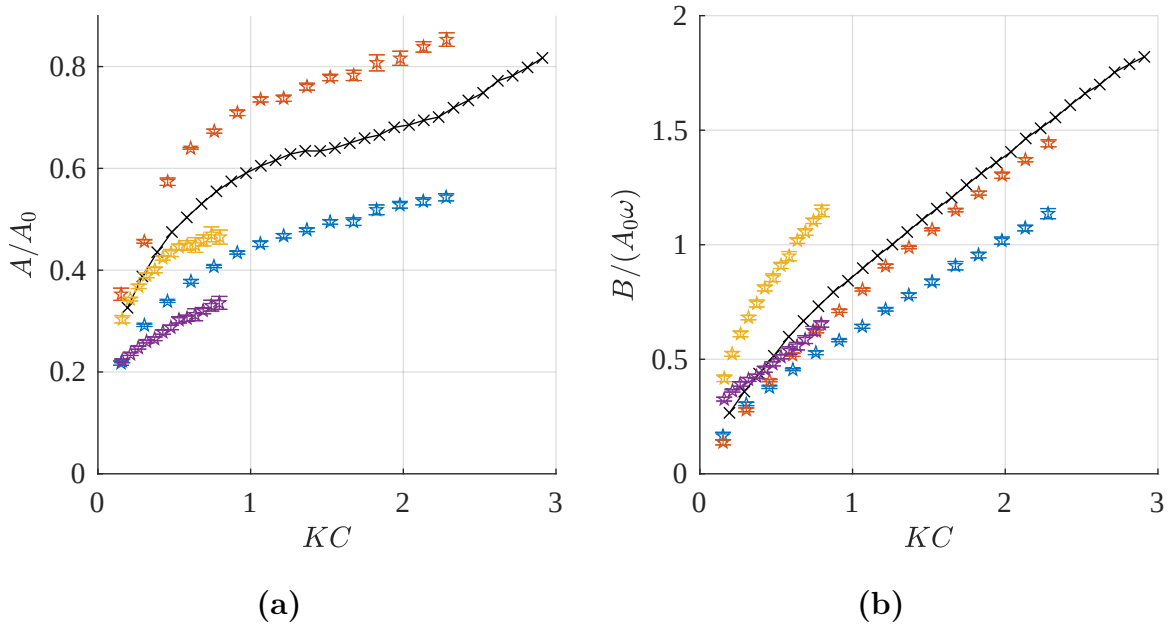

Figure 6.16: Normalized hydrodynamic coefficients for S19 for BiChr 7 run. Legend is found in Figure 6.13. (a) Normalized added mass and (b) normalized damping.

Table 6.1: The coefficients that are used to calculate the force-time series in Figure 6.15 for half-cycle 2. It can be seen that the damping is less for half-cycle 2 than for a regular series, and the added mass is higher due to the start-up effect. $C_{a,2}$ and $C_{b,2}$ are from Figure 6.16 at $KC = 0.76$. $C_{a,reg}$ and $C_{b,reg}$ are taken from Figure 6.3.

Half Cycle nr:	2
KC_2	0.76
$C_{A,reg}$ (from regular curve at KC=0.76)	0.55
$C_{A,2}$ (from present half cycle)	0.67
$C_{B,reg}$	0.72
$C_{B,2}$	0.62
$C_{A,2}/C_{A,reg}$	1.22
$C_{B,2}/C_{B,reg}$	0.86

7 Calculations of Irregular Force Time Series

The knowledge we gained from the bi-chromatic time series is applied to an irregular time series obtained from a Pierson-Moskowitz spectrum. Spectra of the Pierson-Moskowitz type can be expressed as

$$S(\omega) = \frac{A_{PM}}{\omega^5} \exp\left(-\frac{B_{PM}}{\omega^4}\right), \tag{7.1}$$

were

$$B_{PM} = 2^4 \frac{\pi^3}{T_{m0}^4}, \tag{7.2}$$

and

$$A_{PM} = 0.11 \cdot 2\eta_s^2 \omega_1^4 \tag{7.3}$$

and

$$\omega_1 = 1.23 B_{PM}^{\frac{1}{4}}. \tag{7.4}$$

Note that B_{PM} and A_{PM} have nothing to do with added mass and damping, they are just parameters in the spectrum.

η_s is the significant position amplitude (equivalent to one half of the significant wave height if waves are the statistical property) and T_{m0} is the zeroth moment of the period, which corresponds to the expected period in the time series realization.

A time realization can be generated by introducing a random phase angle, ϵ_m, between 0 and 2π, which is uniformly distributed. A number of $M = 100$ components were used, and the spectrum was divided into 100 equally spaced rectangles with height $S(\omega)$ and width $\Delta\omega$. The position of the plate is

$$\eta(t) = \sum_{m=1}^{M} \eta_{am} \sin(\omega_m t + \epsilon_m), \tag{7.5}$$

where

$$\eta_{am} = \sqrt{2S(\omega_m)\Delta\omega}. \tag{7.6}$$

T_m0=1.75 seconds and η_s=0.1 meters. This amplitude corresponds to a significant KC number of KC_s=1.75. Since we are not going to generate statistical data, a run of 4

minutes was found to be enough to find interesting events. However, if statistical data for the forces is desired, a longer run is preferable. However, from a hydrodynamic point of view, details can be analyzed by inspection of the time series. Definitions half-cycles irregular time series are the same as for bi-chromatic time series, which is defined in Section 4.2.

7.1 Strategies of Choosing Hydrodynamic Coefficients

A challenge is to choose wisely the hydrodynamic coefficients, and four strategies are compared in this section. The strategies are

- Constant coefficients through the entire series, chosen based on statistical data.
- A method based on KC_i only.
- A method based on KC_{i-1} and KC_i.
- A method based on the data from the bi-chromatic experiments.

In all methods, we find the hydrodynamic coefficients C_A and C_B from the curves obtained in the regular tests. The hydrodynamic coefficients are functions of the KC number. That is

$$C_A = C_A(KC) \tag{7.7}$$

and

$$C_B = C_B(KC). \tag{7.8}$$

7.1.1 Constant Hydrodynamic Coefficients Coefficients from Statistical Data

In this method, the damping and added mass are constant and chosen based on a characteristic KC value in the time series. The characteristic KC value is chosen to be based on the significant amplitude of motion which was used in the Pierson Moskowitz spectrum and is

$$KC_s = \frac{2\pi}{D}\eta_s \tag{7.9}$$

The constant hydrodynamic coefficients then become

$$C_A = C_A(KC_s) = constant \tag{7.10}$$

and

$$C_B = C_B(KC_s) = constant, \tag{7.11}$$

where $C_A(KC)$ and $C_B(KC)$ are the curves obtained from the regular forced oscillations experiments. The force is then calculated as

$$F(t) = -C_A(KC_s)A_0\ddot{\eta} - C_B(KC_s)A_0\frac{2\pi}{T_m0}\dot{\eta} \tag{7.12}$$

Here T_{m0} is a statistical property used as input in the Pierson Moskowitz spectrum, and it is the mean period of the cycles.

7.1.2 Hydrodynamic Coefficients Based on the Present Amplitude

In this method, the hydrodynamic coefficients are constant for the half-cycle that is under consideration. They are still functions of the KC number and expressed as

$$C_{A,i} = C_A(KC_i) \tag{7.13}$$

and

$$C_{B,i} = C_B(KC_i). \tag{7.14}$$

This notation for the hydrodynamic coefficients is used throughout this thesis. The force for the half-cycle "i" becomes

$$F = -C_{A,i}A_0\ddot{\eta} - C_{B,i}A_0\omega_i\dot{\eta}. \tag{7.15}$$

$\omega_i = 2\pi/T_i$ is the frequency defined in Section 4.2. To calculate a continuous force, the inertia term $C_{A,i}A_0\ddot{\eta}$ needs to change its coefficient 90 degrees before the damping term such that the value of the inertia coefficient, $C_{A,i}$ changes when the acceleration is zero. The inertia term has its maximum 90 degrees before the damping term. Thus the added mass is ahead of the damping. This is always done in this thesis when force time-series are calculated.

7.1.3 Hydrodynamic Coefficients Based on the Previous and Present Amplitude

The method of Section 7.1.2 underestimates the force when the amplitude is decreasing because the circulation of the plate-end vortices is larger from the previous half-cycle

than what is the case for regular steady-state forced oscillations. These vortices induce a higher relative velocity of the water relative to the plate. Higher relative velocity means that U_s (discussed in Section 5.2.2) increases and the circulation of the vortices in the present half-cycle will thus have a higher circulation than for regular steady-state forced oscillations. Thus, the damping coefficient is chosen based on the present KC value, KC_i, if the present position amplitude is larger than the previous, and the previous amplitude, KC_{i-1}, if the present amplitude is smaller than the previous.

There was no clear pattern in the added mass, C_A, based on the previous half-cycle amplitude. However, C_A was distributed close to the regular C_A curve, or lower, except for start-up situations. In these situations, C_A was 20-30 % higher than for regularly forced oscillations, even if the previous half-cycle had the same amplitude as the present. This is discussed in more detail in section Section 6.4.2. However, it was found that the damping decreased in these situations. Because of this, the added mass is chosen based on the present KC value, KC_i.

The force for the half-cycle "i" is given by

$$F_i(t) = -C_{A,i}A_0\ddot{\eta} - C_{B,i}A_0\omega_i\dot{\eta} \qquad \text{if} \qquad KC_i > KC_{i-1}, \tag{7.16}$$

and

$$F_i(t) = -C_{A,i}A_0\ddot{\eta} - C_{B,(i-1)}A_0\omega_i\dot{\eta} \qquad \text{if} \qquad KC_i < KC_{i-1}. \tag{7.17}$$

The notation for the added mass and damping coefficients are defined in Equation 7.13 and Equation 7.14.

7.1.4 Hydrodynamic Coefficients Based on Data from Bi-Chromatic Tests

In this method also, we assume that the added mass is found by assuming that one can use the regular curve and the present KC if KC_s is in the damping dominated regime. The damping coefficient is found by multiplying the damping coefficient that is found from the regular test curve at the present KC value, KC_i by a factor that is a function of the value of the fraction KC_i/KC_{i_1}. This factor is based on Figure 7.1 and is presented in Table 7.1. b_{biBhr} is found by interpolating in the table.

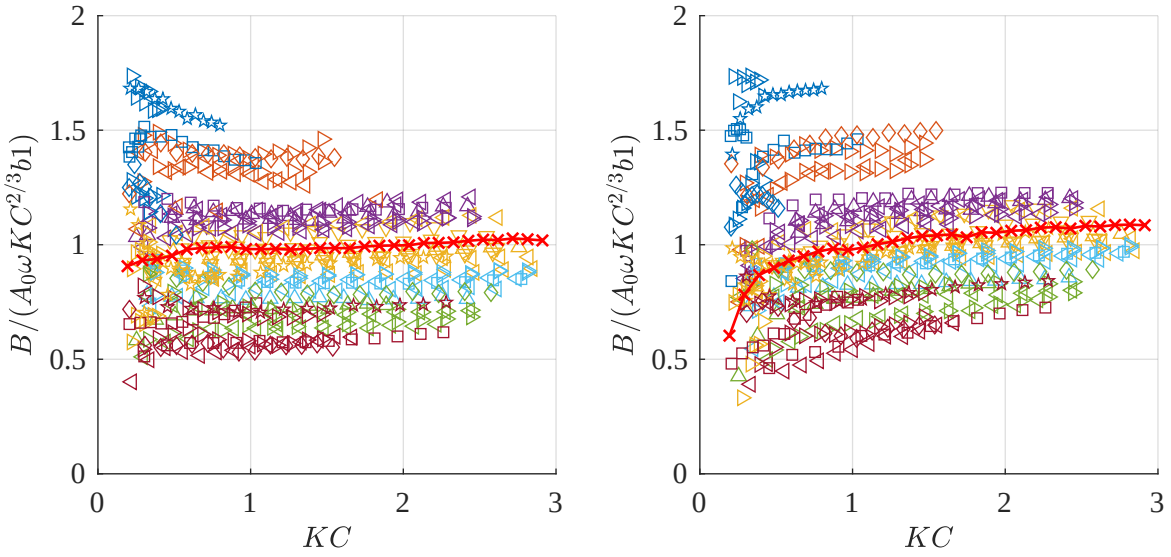

(a) Plate S19 **(b)** Plate S28

Figure 7.1: The legend is found in Figure 6.8. The damping divided by $KC^{2/3}b_1$. b_1 is a constant that is adjusted such that the regular curve is close to 1 in this figure. One can see from the figure that a good approximation for all intervals of KC_i/KC_{i-1} is to multiply the regular curve with constants. These constant, which are from this figure, are found in Table 7.1. (a) Plate S19 and (b) Plate S28.

Table 7.1: The table shows the factor, b_{biChr} that are used in the improved method. The data in the table is base on the bi-chromatic tests in Figure 7.1. S28 and S19 in the parenthesis denotes the plate name.

KC_i/KC_{i-1}	0	0.24	0.55	0.75	0.9	1.1	1.4	2	4.5	∞
b_{biChr} (S19)	1.8	1.8	1.4	1.2	1.1	0.95	0.85	0.8	0.6	0.6
b_{biChr} (S28)	1.8	1.8	1.5	1.2	1.1	0.95	0.9	0.8	0.7	0.7

Physically b_{biChr} is not bounded by an upper value when $KC_i/KC_{i-1} \to 0$ since the circulation from the previous vortex contributes to the production of a new vortex. However, since the present amplitude for the half-cycle is small when $KC_i/KC_{i-1} \to 0$, the forces will be small compare to larger amplitudes of motion. Thus, these forces are not considered to be important in the time series and are limited at 1.8 times the damping found from the curve from the regular steady-state forced oscillations. This value was observed to be the highest in Figure 7.1. When $KC_i/KC_{i-1} \to \infty$, the damping is bounded by the case where the plate is accelerated in still fluid because there are no previous vortices that increase the relative velocity in a still fluid.

The force for half-cycle "i" can then be found as

$$F_i(t) = -C_{A,i}A_0\ddot{\eta} - b_{biChr}C_{B,i}A_0\omega_i\dot{\eta}. \tag{7.18}$$

7.2 Irregular Force Time Series

This section presents a part of an irregular time series for plate S28 and S19. The same time series for the position is used as input for both plates in the experiments. The part of the time series presented is chosen since it contains interesting events like; small amplitude to large amplitude, from large amplitude to small amplitude, similar consecutive amplitudes, and large amplitudes close to the maximum.

There are three figures for each plate with different ways of calculating the force, which are presented in Section 7.2.1 and Section 7.2.3. The computed force is based on the methods presented in Section 7.1. The measured force and the calculated force from the method of Section 7.1.3 are plotted in all figures. The method in Section 7.1.3 is plotted in all figures, because it is simple to use, and it seems like it computes conservative results for both increasing and decreasing half-cycle amplitudes. The improved method in Section 7.1.4, which is based on the bi-chromatic time series, yielded the best results. However, the method complicates the problem, and the coefficient is specific only for these models. The simplest method, based on the statistical data, yielded the most inaccurate results and over-predicted the force for small half-cycle amplitudes and underpredicted the force for large half-cycle amplitudes. An improvement is seen for the method that only takes the present KC number, KC_i, into account. However, the method underpredicts the force if the half-cycle amplitude is going from a large to a small amplitude. The method that uses both KC_i and KC_{i-1} fixes this problem, and it seems to yield conservative results with an exception in the event that is discussed in Section 7.2.2. The improved method based on the bi-chromatic results fixes some of the overshooting for the method, of KC_i and KC_{i-1}. However, the improvement is not considered significant, taking into account the added complexity.

The measured force's maxima are expected to be somewhat larger than the calculated force since we are only considering the first-harmonic hydrodynamic coefficients in the calculations. Since we are interested in crane operations and lowering structures towards the seabed, the force's impulse is the important parameter. The force peak from the third-harmonics does not contribute much to the impulse since the third-harmonic peak is narrow.

7.2.1 Irregular Force Time Series for Plate S28

In this section, a part of the time series for model S28 is presented for KC_s=1.75. The methods that are discussed in Section 7.1 are compared to each other. Note that all figures contain the measured force from the experiments and the calculated force from the method in Section 7.1.3. The methods that are compared are given in the figure texts.

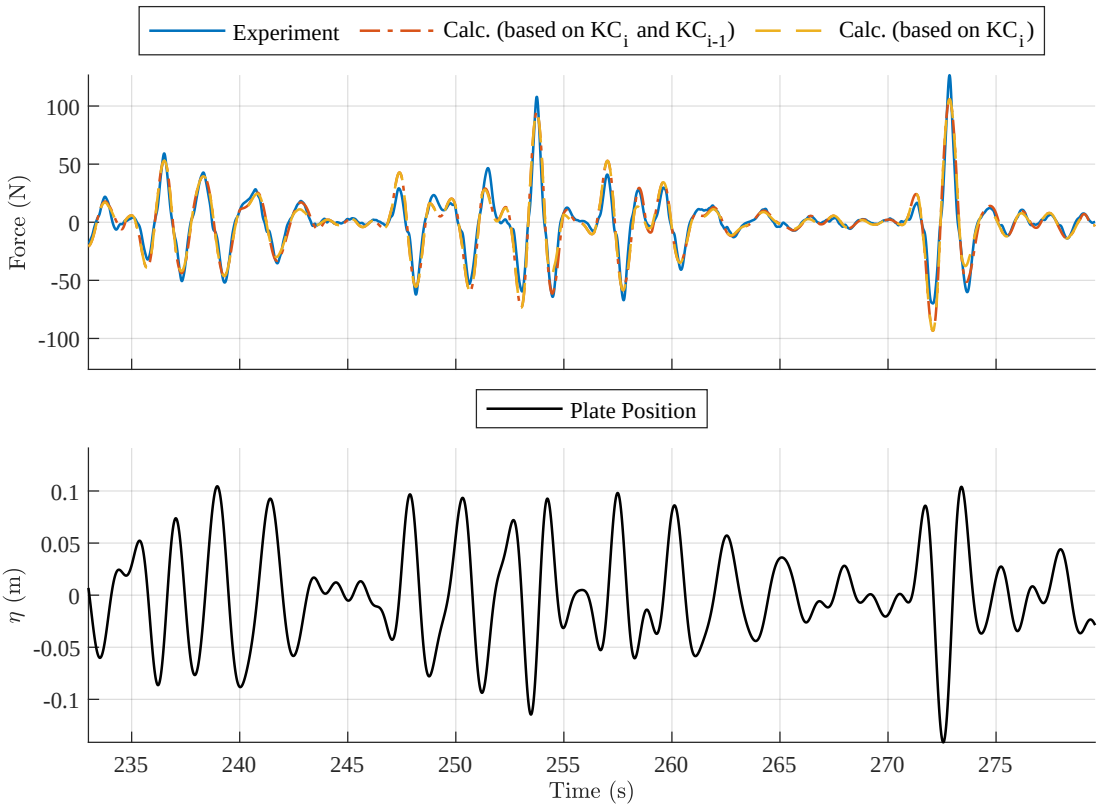

Figure 7.2: Plate: S28. Method that is compared: Method were the normalized damping coefficient C_B is chosen based on the KC value for the present half-cycle.

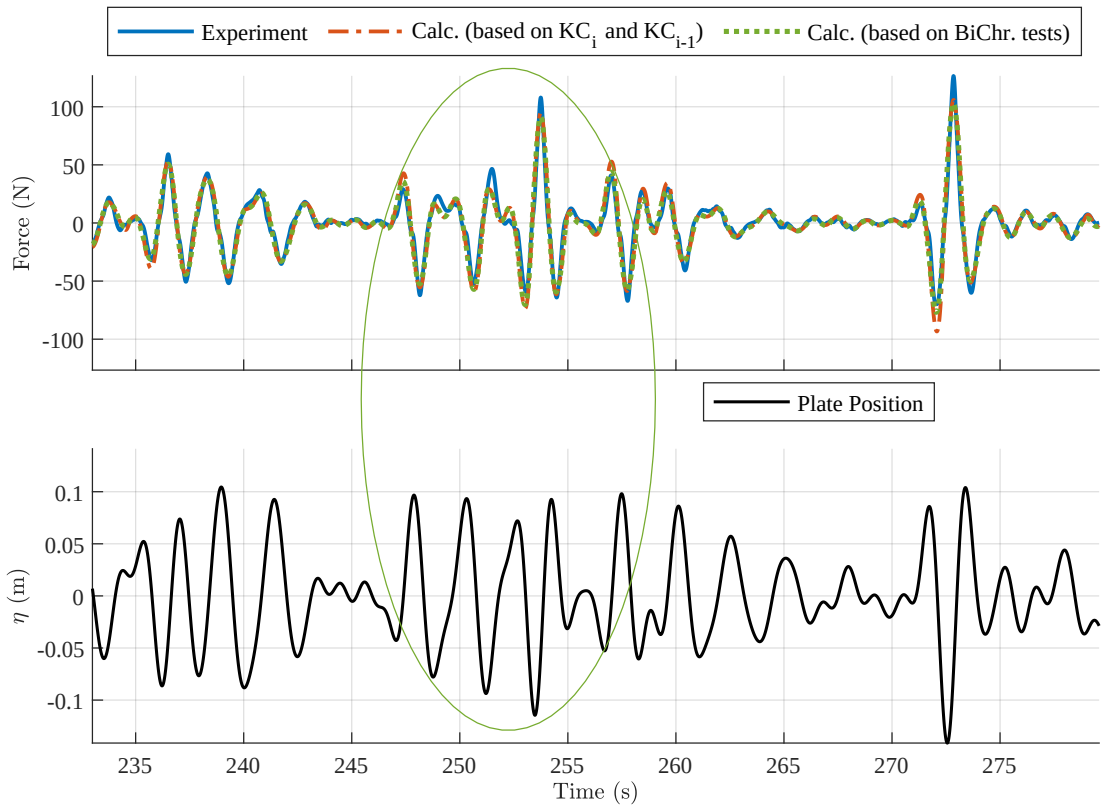

Figure 7.3: Plate: S28. The method that is compared is the improved method where the normalized damping coefficient C_B is chosen based on the bi-chromatic tests' data. The event in the green circle is discussed in Section 7.2.2.

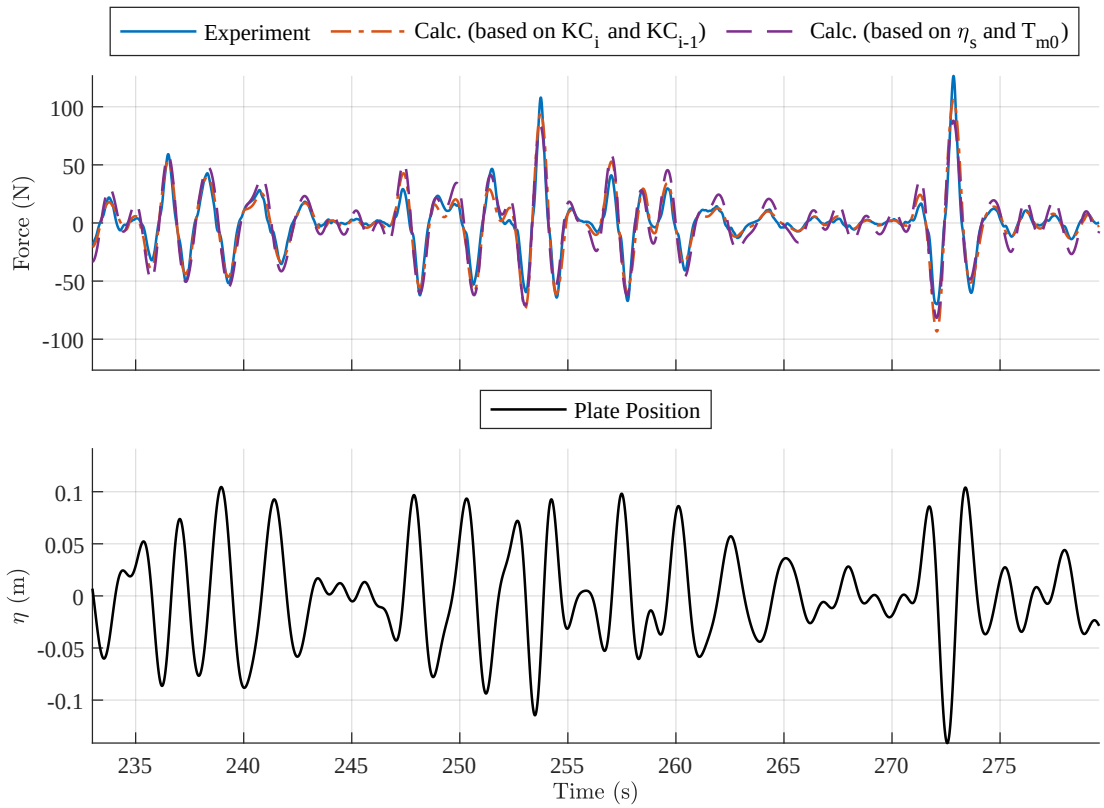

Figure 7.4: Plate: S28. Method that is compared: Method were the normalized damping coefficient C_B is constant and chosen based on the statistical data.

7.2.2 Discussion of Half-Cycles with Three Zero Crossings in the Acceleration.

The event that is marked with a green circle in Figure 7.3 requires some attention. The half-cycles have a saddle-like shape of the position signal. This means that the half-cycle has three zero crossings in the acceleration. In this situation, the forces are underpredicted by the methods and are seen in Figure 7.6. The reason for this is not known, but since we know when it happens, it can be corrected if necessary. However, these situations never lead to the largest forces in the time series, since the three zero crossings of the acceleration flatten the force curve. This effect is not discussed any further, but it is worth mentioning if a conservative force prediction is needed in the whole time-domain.

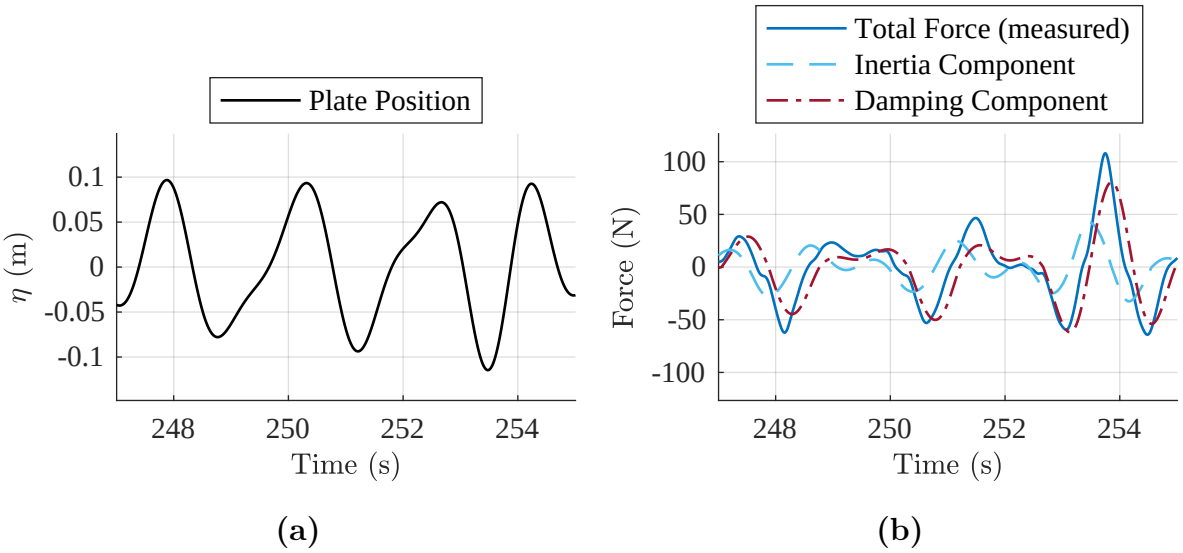

(a) **(b)**

Figure 7.5: (a) Position time series in the area of interest shown with a green circle in Figure 7.3. The curve of the position signal has a decrease in the derivative in some half-cycles, followed by an increase. This means that the acceleration has three zero-crossings for one half-cycle. (b) Added mass and damping computed with the improved method based on the bi-chromatic tests.

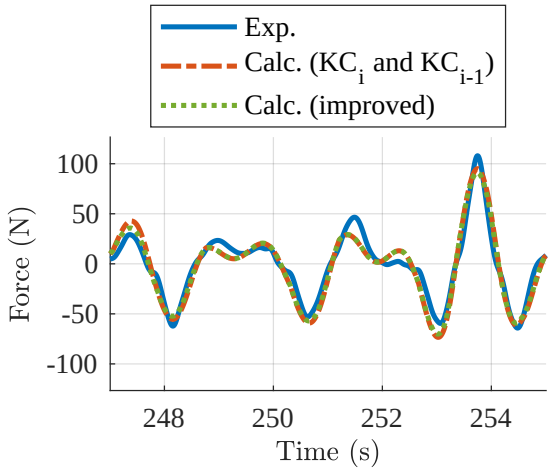

Figure 7.6: Plate: S28. The figure shows that the force gets underpredicted by the calculations at Time=251.5 s. This happens when the acceleration has three zero crossings in one half-period. Calc. (improved) finds coefficients based on the Bi-Chromatic tests, and Calc. (KC_i and KC_i) refers to the method were the hydrodynamic coefficients chosen based on if the amplitude of the previous half cycle is larger or smaller than the present half-cycle.

7.2.3 Irregular Force Time Series for Plate S19

In this section, a part of the time series for model S19 is presented for KC_s=1.75. The methods that are discussed in Section 7.1 are compared to each other. Note that all figures contain the measured force from the experiments and the calculated force from the method in Section 7.1.3. The methods that are compared are given in the figure texts.

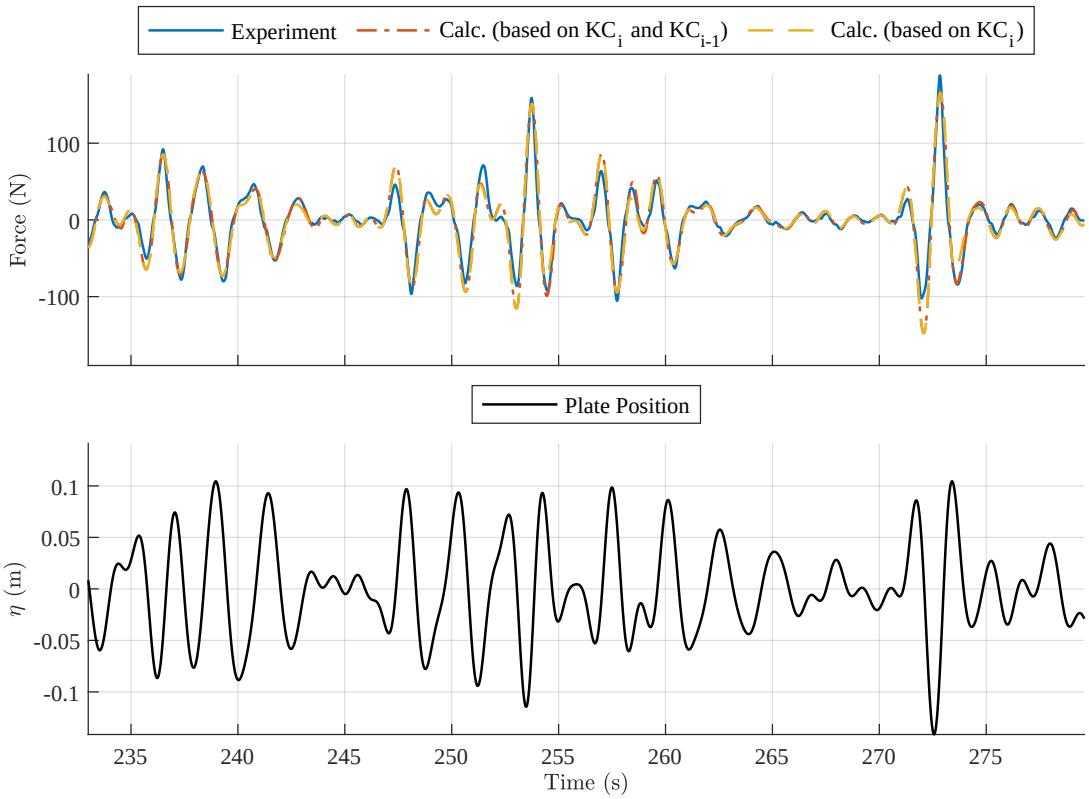

Figure 7.7: Plate: S19. The method that is compared: Method were the normalized damping coefficient C_B is chosen based on the KC value for the present half-cycle.

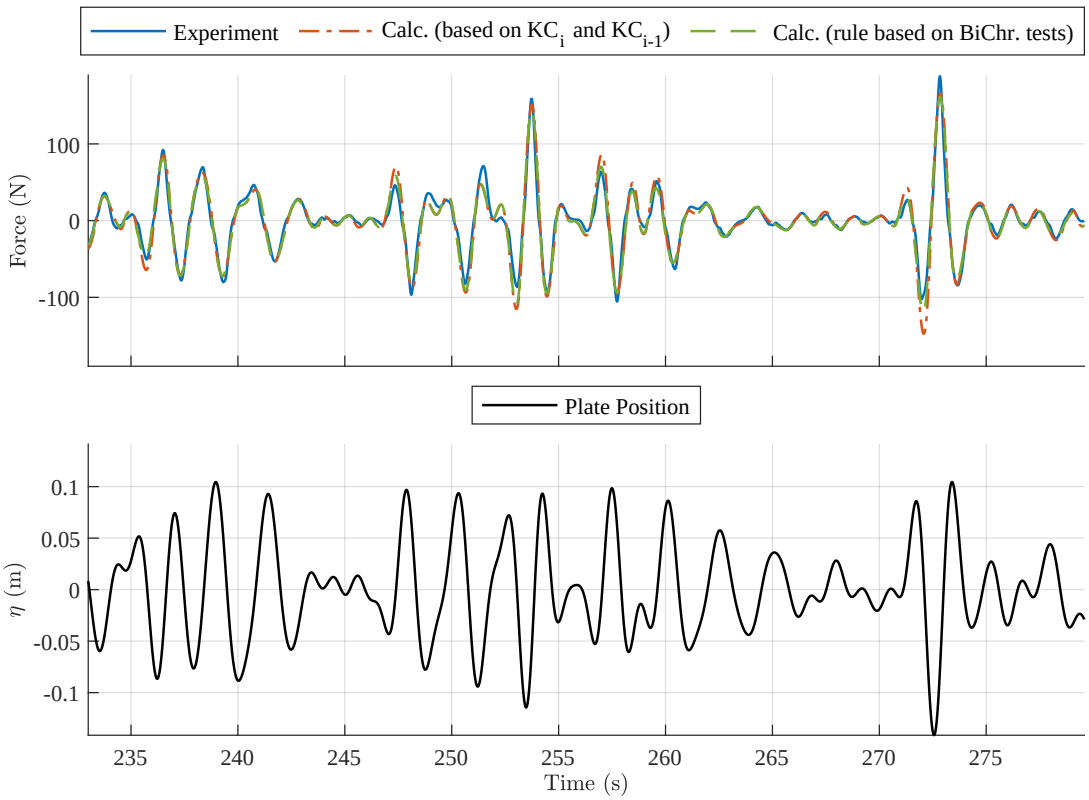

Figure 7.8: Plate: S19. The method that is compared: Improved method where the damping coefficient C_B is chosen based on the data for the Bi-Chromatic tests.

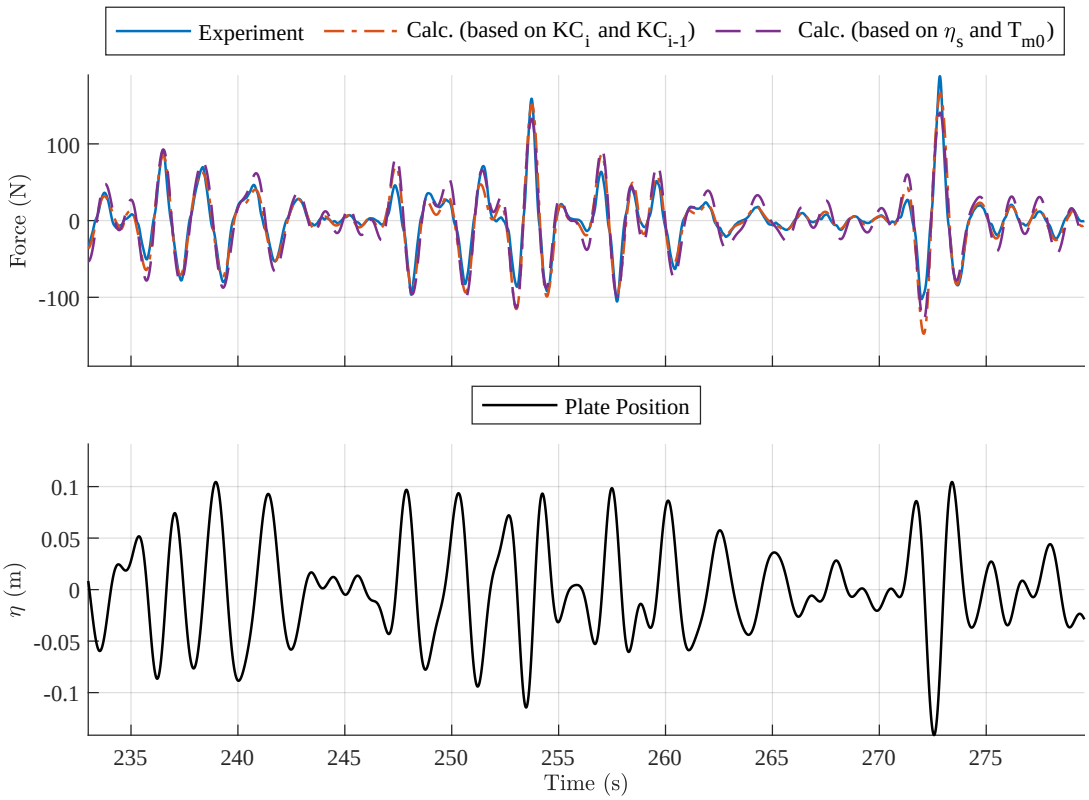

Figure 7.9: Plate: S19. The method that is compared: Method where the damping coefficient C_B is constant and chosen based on the statistical data.

7.3 Discussion of an Event with Large Changes in Motion Amplitudes

The time series for S28 is chosen to be studied further. The time series for S19 is shows a similar behavior as for S28, which can be seen in Section 7.2.1 and Section 7.2.3 .

Three events are of special interest and are studied further in this section. The three events for the half-cycles are:

- When the amplitude increases
- When the amplitude decreases
- Large amplitudes

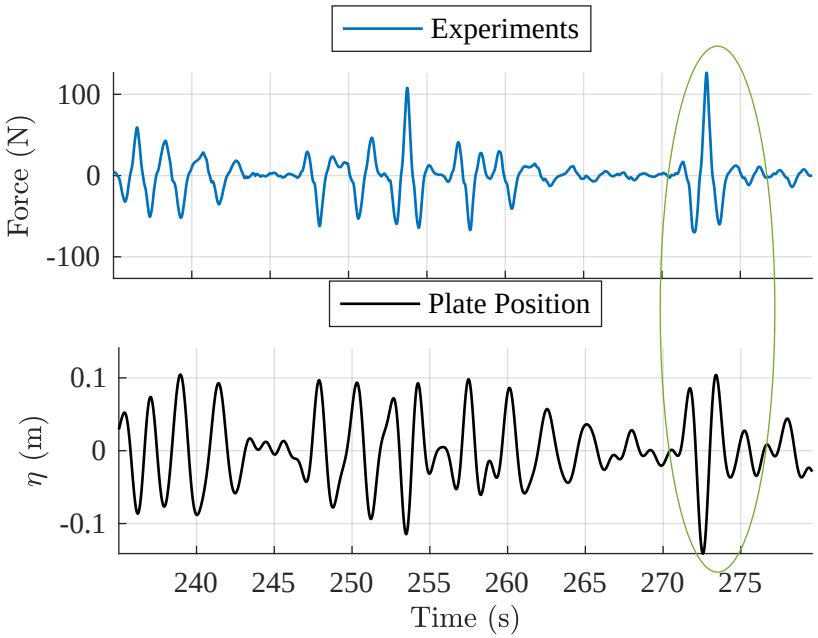

Figure 7.10: The figure shows a part of the irregular time series for plate S28. The green circle shows the area of interest that is studied further in this section.

Figure 7.10 shows the area of interest that has all these events. Figure 7.11 (b) shows that the method where the coefficients are held constant and based on the significant KC from η_s, overpredicts the forces when the motion amplitude increases and under predicts for the largest amplitude. The method that is based on the present KC number overpredicts the force when the amplitude increases and underpredicts it when it decreases from one half-cycle to another. It predicts the maximum well, and the difference between the experimental and calculated force is because the third-harmonic force is not taken into account. However, the third-harmonic force has a limited contribution to the force impulse because the peak is narrow. For offshore operations, the force impulse is the critical parameter. Figure 7.12 (a) shows that the method based on both the previous and the present KC number, corrects the underprediction when the half-cycle amplitude

decreases from one half-cycle to the next, but it does not fix the overshoot when the KC number increases. Figure 7.12 (b) shows that the overprediction of the forces can be corrected by using the improved method, where the hydrodynamic coefficients are chosen based on the bi-chromatic tests. However, due to its added complexity, the improved method is not regarded as the best method for a simplified analysis. The method where the coefficients are based on KC_i and KC_{i-1} is considered to be the best due to its simplicity, and due to that it computes conservative, but most of the time, accurate results. Figure 7.13 shows the decomposed forces plotted against the measured force. The damping dominates the forces, and thus the most important component to calculate accurately is the damping for the KC values in this part of the time series.

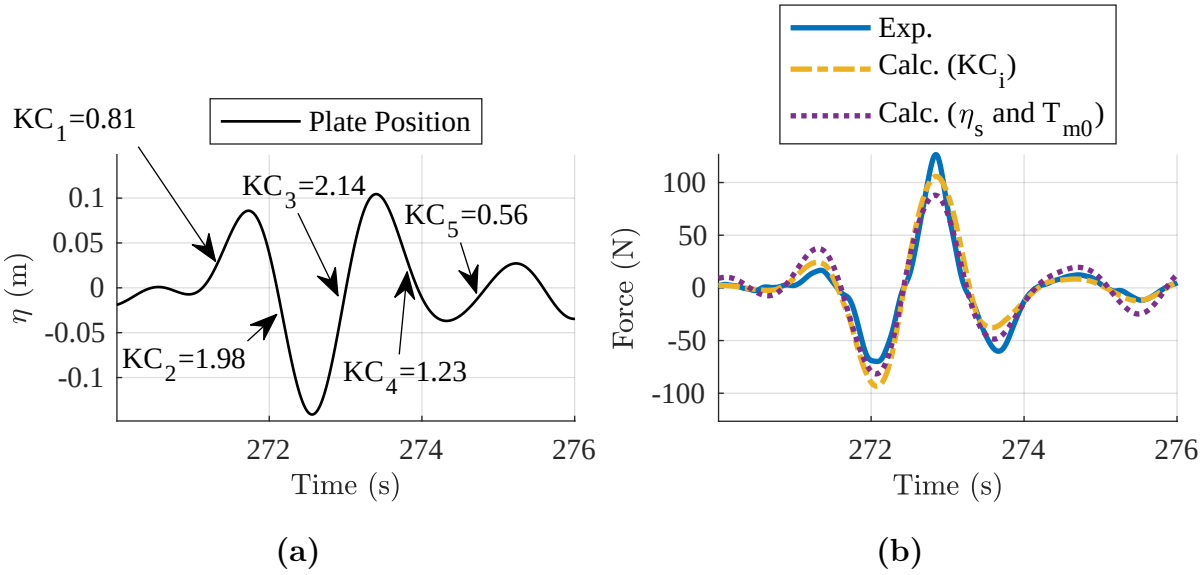

Figure 7.11: (a) Position in the area of interest shown in Figure 7.10. The value of each half amplitude is shown. The maximum KC number is 2.14. (b) Force time series measured from experiments, calculated force based on the present amplitude KC_i, and calculated force where the hydrodynamic coefficients are constant and chosen based on statistical data. η_s is significant amplitude and T_{m0} is the zero moment period in the Pierson-Moskowitz spectrum.

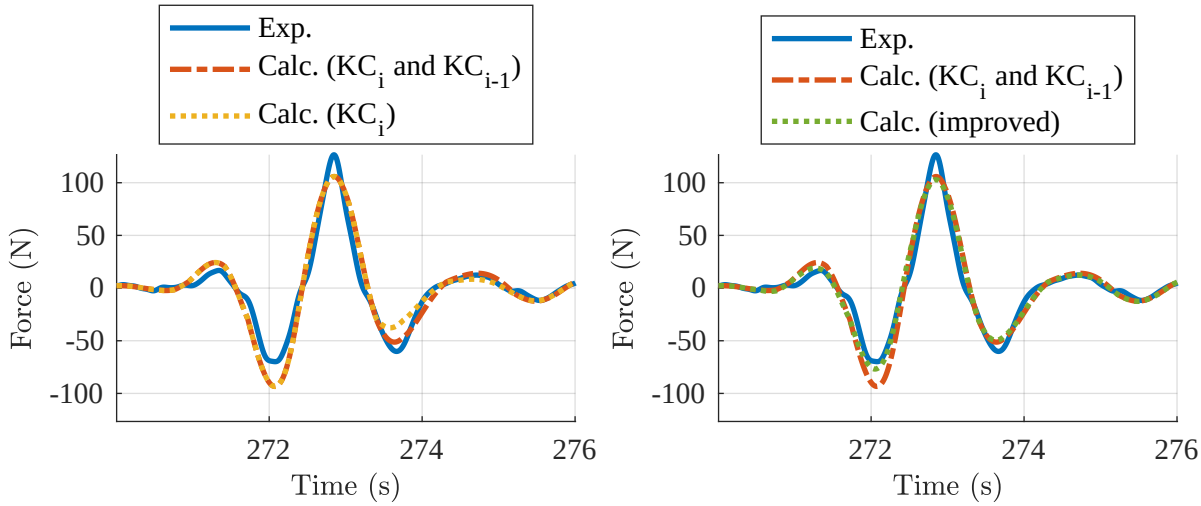

Figure 7.12: (a) Close up view of force-time series measured from experiments, calculated force based on the previous and present amplitude, KC_i, and KC_{i-1}. These are plotted against calculated force based on the present amplitude, KC_i. (b) The improved method refers to the method were the coefficients come from the bi-chromatic experiments .

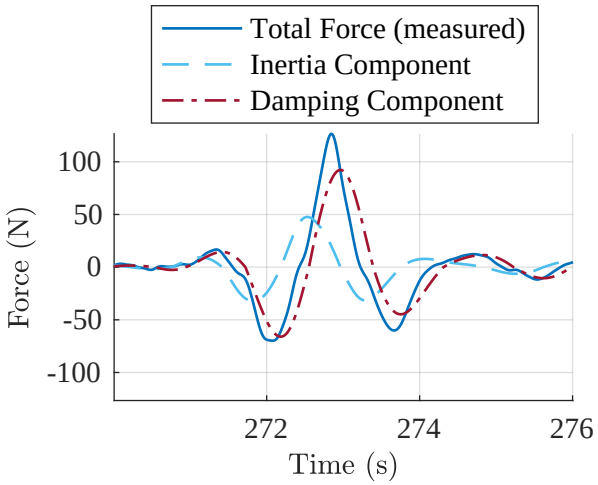

Figure 7.13: Measured force compared to the calculated inertia force component and damping force component. The damping force is almost twice as large as the added mass force for the largest force amplitude in the figure. The inertia force component (F_A) is calculated by choosing the added mass coefficient based on the present amplitude and by using the added mass curve found by the regular tests. The damping force component (F_B) is calculated by choosing the damping coefficient with the method that is made based on the bi-chromatic experiments. Thus, $F = F_A + F_B$ is the green curve in Figure 7.12 (b).

7.4 Mentzoni and Kristiansen's Semi-Analytical Method Applied on the Time Series

In this section the semi-analytical method of Mentzoni and Kristiansen (2019) is used to find the hydrodynamic coefficients for the irrigular time series. The semi-analytical method is described in section Section 2.2.3. The perforated plates that the method is based on are thinner than the models in the present study, and thus some variations are expected, especially for the added mass since the zero amplitude added mass is different when the plate thickness is increased.

The hydrodynamic coefficients can be easily obtained by a code programmed in Matlab, as in Figure 7.14.

```
function res=findMentzoniCoeff(tau,KC)

    %returns normalized added mass and damping
    %tau:perforation ratio (area_ventilated/area_total)
    %KC=2*pi*eta_ai/D. (eta_a:position amplitude, D: plate width)

    %table:
    mentzoniTab=[0.00 1.000 0.216 10.1;
    0.05 0.748 0.230 10.1;
    0.10 0.498 0.252 9.58 ;
    0.15 0.281 0.271 8.72 ;
    0.20 0.132 0.261 7.67 ;
    0.25 0.055 0.222 6.57 ;
    0.30 0.017 0.181 5.48 ;
    0.35 0.000 0.156 4.44 ;
    0.40 0.000 0.120 3.49 ;
    0.45 0.000 0.087 2.69 ;
    0.50 0.000 0.057 2.04 ];

    %vector of perforations:
    tau_tab=mentzoniTab(:,1);

    %coefficients:
    a0_tab=mentzoniTab(:,2);
    a1_tab=mentzoniTab(:,3);
    b1_tab=mentzoniTab(:,4);

    %interpolating in the table
    a0=interp1(tau_tab,a0_tab,tau);
    a1=interp1(tau_tab,a1_tab,tau);
    b1=interp1(tau_tab,b1_tab,tau);

    %calculating the normalized added mass and damping:
    C_A=a0+a1*KC^(2/3);
    C_B=b1/(pi^2)*KC^(2/3);

    res=[C_A,C_B];

end
```

Figure 7.14: Example of a code that finds the hydrodynamic coefficients from the semi-analytical method of Mentzoni and Kristiansen (2019)

Figure 7.15 and Figure 7.16 compares the semi-analytical method with the results obtained from the regular experiments. The figures show that the added mass is under-predicted. This is expected since the semi-analytical method is based on thin perforated plates, while in our experiments, the plates are thicker. A candidate for the larger added mass for S19 and S28 compared to the semi-analytical method is that the added mass in potential theory is higher when the thickness is increased. The figures also show that the damping is well predicted, and since the forces are damping dominated for higher KC

numbers, the most important for the force amplitude is the damping. If the damping is twice the inertia force, the damping contributes to 89.4 % of the force amplitude. This is because the force amplitude is calculated as

$$F_a = A_0\omega^2\eta_a\sqrt{\left(\frac{A}{A_0}\right)^2 + \left(\frac{B}{A_0\omega}\right)^2} = A_0\omega^2\eta_a\sqrt{C_A^2 + C_B^2}. \tag{7.19}$$

Figure 7.15 and Figure 7.16 shows that damping is more than twice the added mass force if $KC > 1.5$ for both plates, S28 and S19. Figure 7.11 shows that the largest amplitude is equivalent to a KC number of 2.14 for this part of the time series. Thus the force is damping dominated for both plates for the larges amplitudes in the time series. The damping force alone will contribute to almost 90% on the maximum force when it is twice the added mass force.

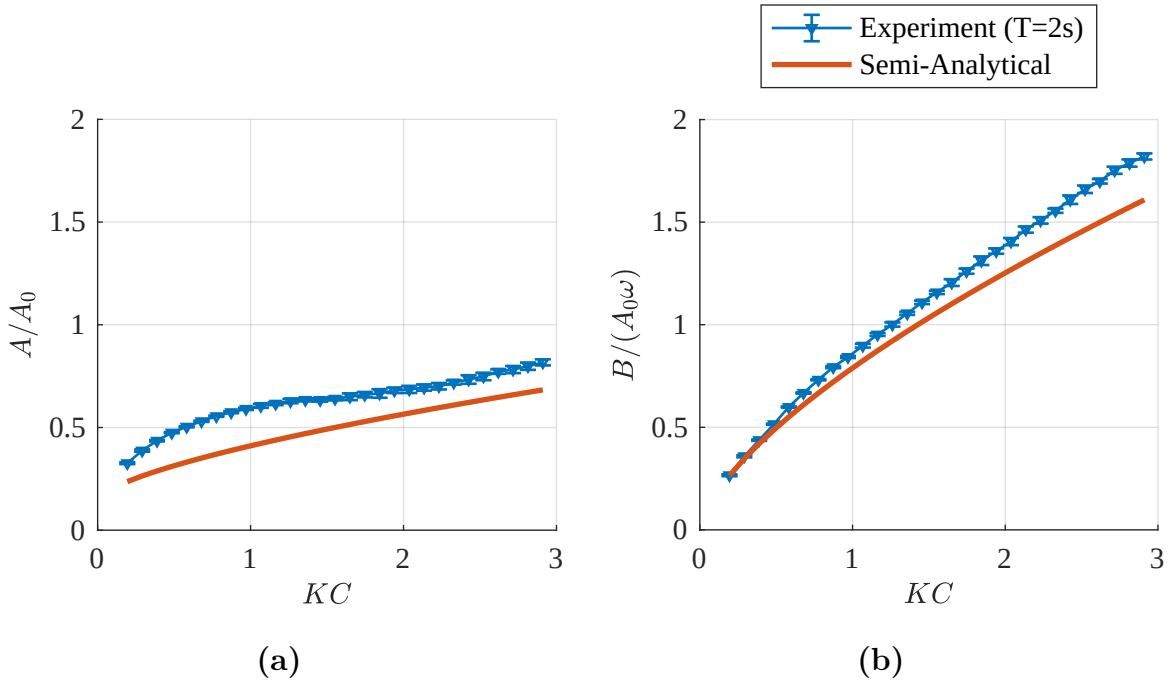

Figure 7.15: Comparison of the experiments and the semi-analytical method for plate S19. The plots show (a) the normalized added mass, C_A, and (b) damping C_B. The figure also shows that the damping force is twice the added mass force when KC number is approximate 2.

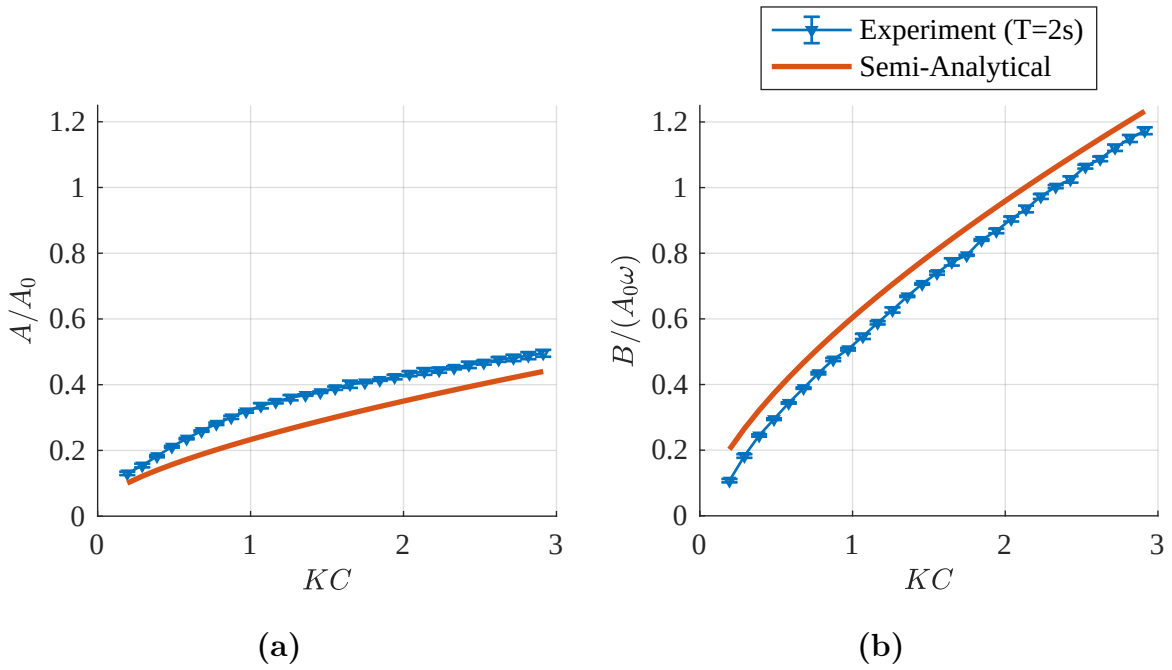

Figure 7.16: Comparison of the experiments and the semi-analytical method for plate S28. The plots show (a) the normalized added mass, C_A, and (b) damping C_B. The figure also shows that the damping force is twice the added mass force when KC is approximate 1.5.

The choice of coefficients (C_A and C_B) is based on the present and previous KC number, which is presented in Section 7.1.3. The hydrodynamic coefficients are obtained either from the regular experiments or the semi-analytical method, for comparison. Figure 7.17 and Figure 7.18 shows a part on the time series for S19 and S28 respectively. A closer view for both plates is seen in Figure 7.19 at the same event that is discussed in Section 7.3. Figure 7.19 shows that the semi-analytical method is well suited to predicting the forces in a time series generated by a Pierson-Moskowitz spectrum with a significant KC_s=1.75 for both plates. The forces on both models are dominated by damping for this value of KC_s. For a hatch cover with 7.5 meters width, $K_s = 1.75$ corresponds to a significant half-cycle amplitude of 4.18 meters. For a 10 meters wide hatch cover, this corresponds to a significant half-cycle amplitude of 5.57 meters, which is large amplitudes in the context of marine operations. However, the KC values are realistic for smaller structures.

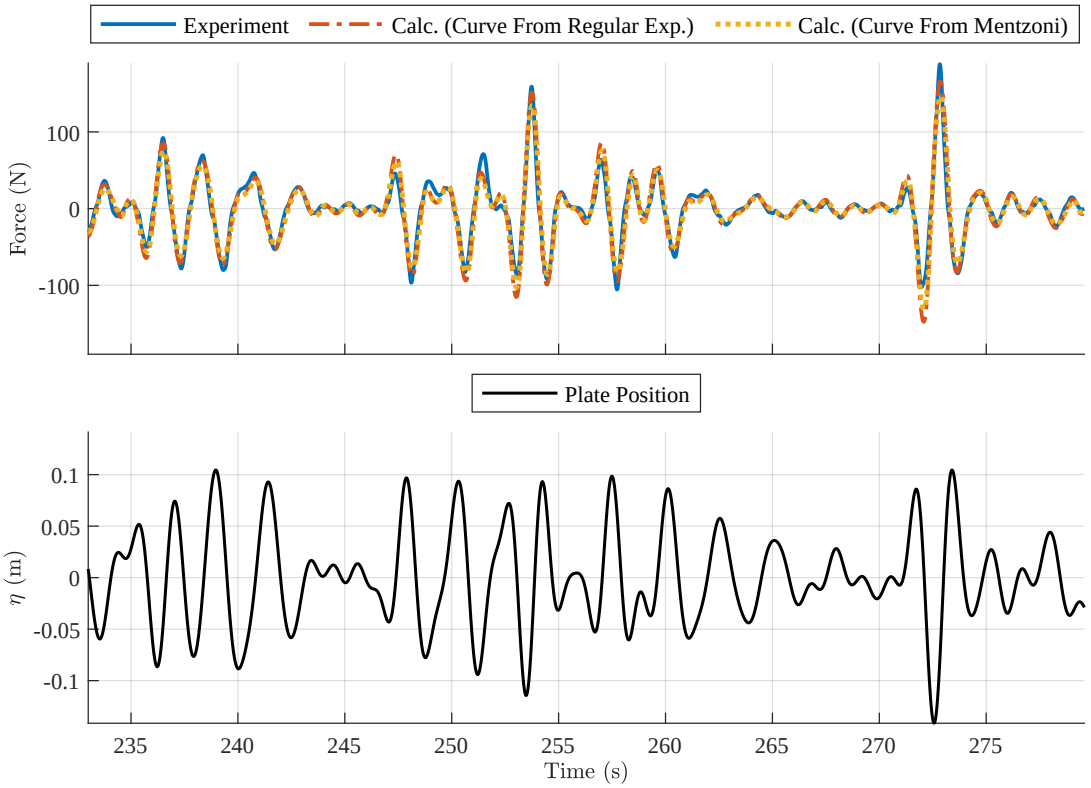

Figure 7.17: Plate: S19. Comparison of hydrodynamic coefficients obtained from the regular experiments and the semi-analytical method by Mentzoni and Kristiansen (2019).

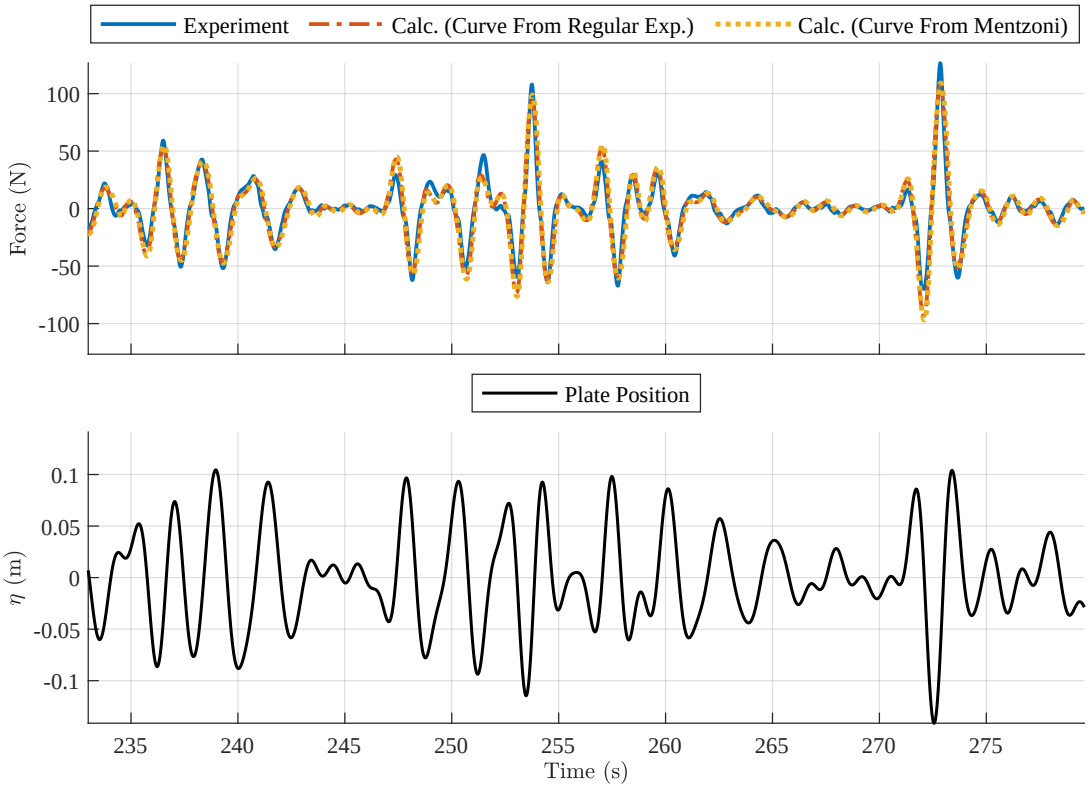

Figure 7.18: Plate: S28. Comparison of hydrodynamic coefficients obtained from the regular experiments and the semi-analytical method by Mentzoni and Kristiansen (2019).

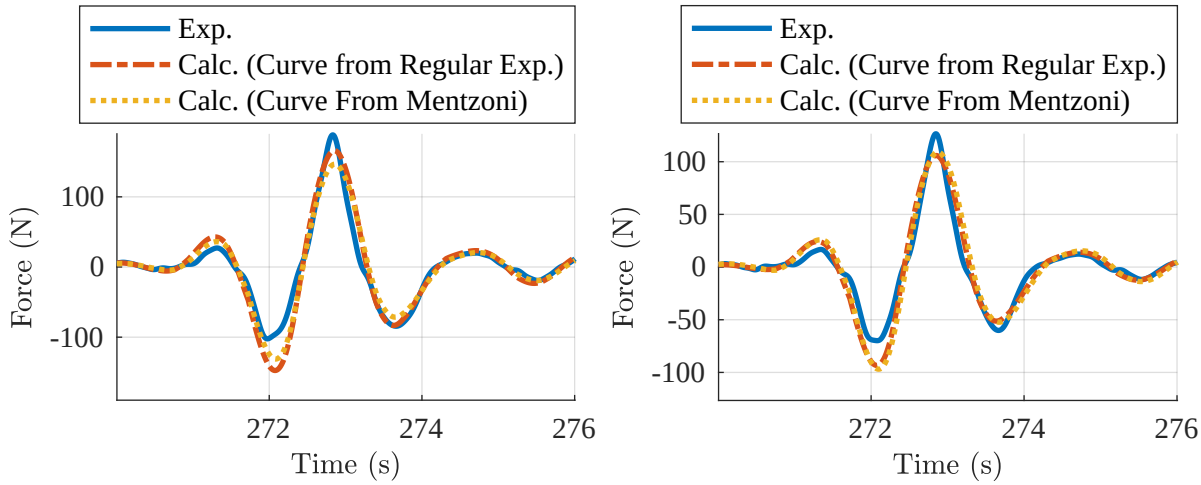

Figure 7.19: A closer view of the comparison between hydrodynamic coefficients from the regular experiments and the semi-analytical method by Mentzoni and Kristiansen (2019). Time series for (a) plate S19 and (b) plate S28.

7.5 Semi-Analytical Method Applied on Irregular Time Series in the Inertia-Damping Range

Plate S19 was chosen to look more into because the added mass relative to the damping is slightly higher than for S28. The same time realization is used as before, but with $KC_s = 0.87$. This KC number corresponds to a significant amplitude of motion of 2.1 meters for a 7.5 meters wide hatch cover. For a 10 meters wide hatch cover, this corresponds to a significant amplitude of motion of 2.79 meters in still water. The time series for the position for the zoomed-in forces is the same as Figure 7.11 (a), but the KC values and η is divided by two, such that the maximum KC value, KC_3 is 1.07.

Figure 7.20 (a) shows the damping and added mass term plotted against the measured force from the experiment. The damping and added mass are calculated based on the improved method based on the Bi-Chromatic tests. It is described in Section 7.1.4, and the added mass and damping curves are obtained from the regular tests. The figure shows that the damping and added mass term amplitude values are close in magnitude.

Figure 7.20 (b) shows the calculated force, which is based on the method that takes into account the present and previous KC numbers, as described in Section 7.1.3. The only difference between the two curves is that the hydrodynamic coefficients are taken either from the semi-analytical method or the regular experiments for (T=2s). As discussed in Section 6.4.2, the force amplitude is not affected by a start-up situation. Thus the force is calculated as in Section 7.1.3.

Figure 7.20 (b) and Figure 7.21 shows that the method also works in the smaller KC range if the coefficients are taken from the regular experiments. The figure also shows that the semi-analytical method computes smaller forces compared to when the coefficients

are taken from the experiments. The reason for this can be explained by that the semi-analytical method of Mentzoni and Kristiansen (2019) underestimates the added mass because it is based on thin plates. When added mass and damping terms have similar amplitudes, the semi-analytical method should be used with caution if the plate has some thickness. This difference can probably be accounted for in the semi-analytical method by adding a constant term for the added mass, such that it can be used for other structures than thin plates. This is an area of further research. The zero-amplitude added mass (potential-flow) is smaller for thin perforated plates compared to thicker perforated plates, and it looks like this increases the added mass for all tested KC numbers, which can be seen in Figure 7.15 (a) and Figure 7.16 (a).

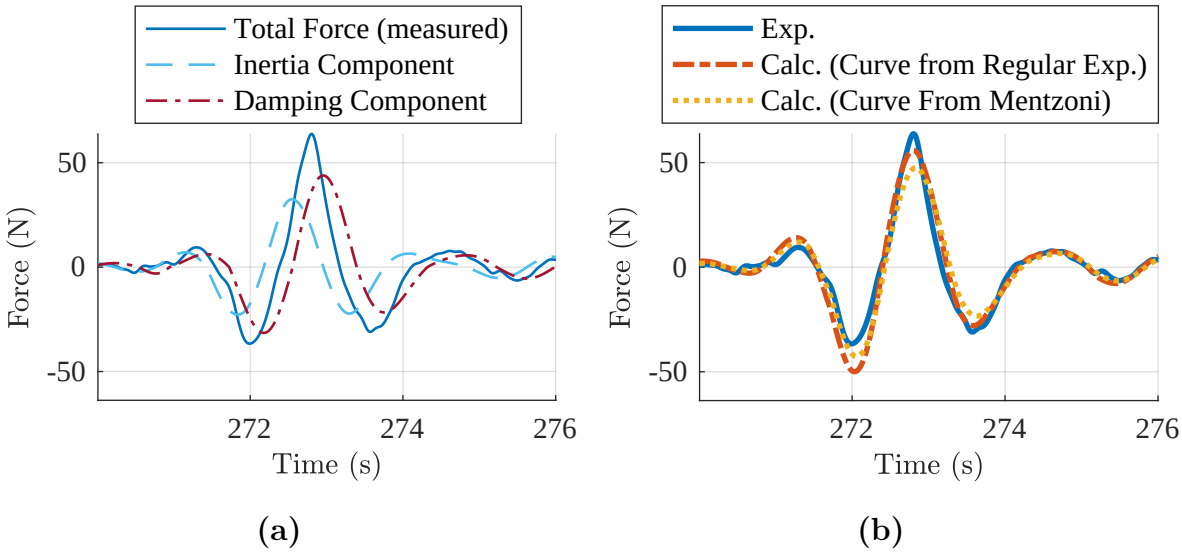

Figure 7.20: (a) Added mass and damping force plotted against the measured force. (b) Comparison between force time series with coefficients from the regular experiments and the semi-analytical method by Mentzoni and Kristiansen (2019) for plate S19.

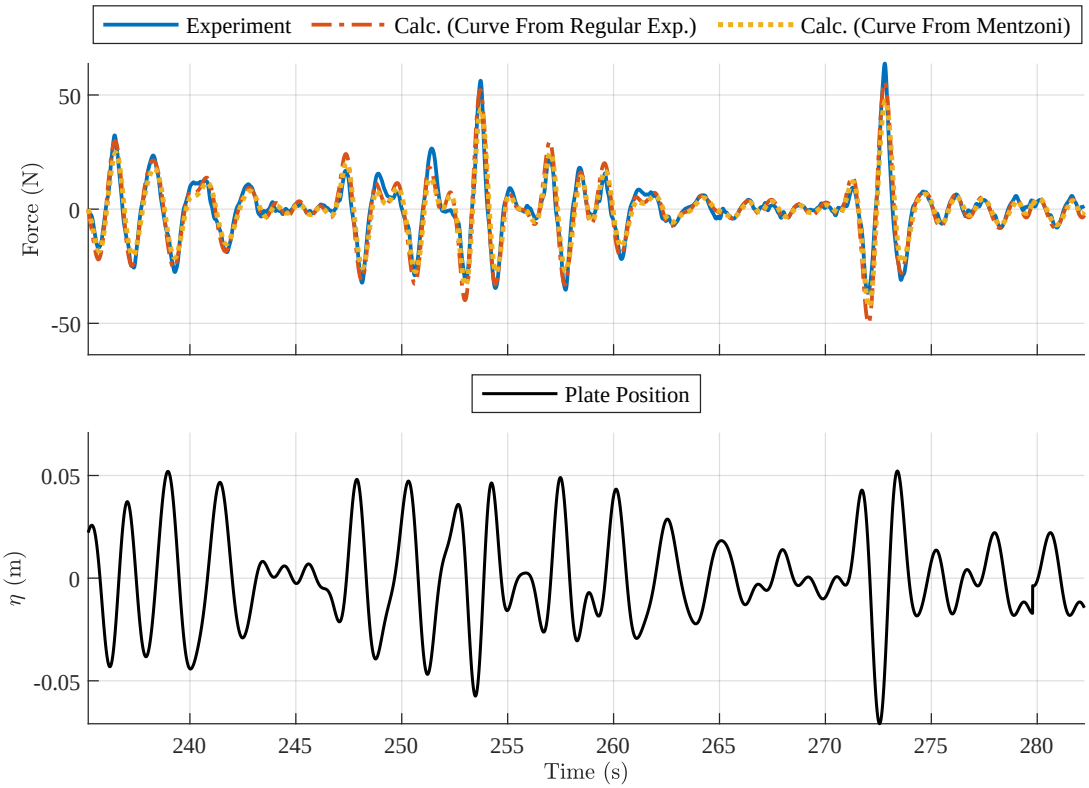

Figure 7.21: Comparison of force time series when the hydrodynamic coefficients are obtained either from the regular experiments or the semi-analytical method by Mentzoni and Kristiansen (2019). The model is plate S19.

7.6 Proposed Method for Force Calculation in Long Crested Irregular Seas with Long Wave Length for Damping Dominated Forces far from the Free Surface

This proposed method calculates the forces in long-crested irregular seas with long-wavelength components, for damping dominated perforated plates far from the free surface and the seafloor. In this context, "far away from the free surface and seafloor" means that the mean position of the plate is more than 1.39D under the free surface or 1.39D above the seafloor for KC numbers up to 2.5. This distance is based on the findings of the conducted experiments.

In waves in combination with forced oscillations in heave, the KC_i number should be based on the relative velocity between the water and the plate. We call it the relative KC_r value. The relative velocity is

$$u_{rel} = \frac{d\eta(t)}{dt} - w(t) \tag{7.20}$$

According to Faltinsen (1990) w in Equation 7.20 can be generalized to irregular long crested sea as

$$w(t) = \sum_{m=1}^{M} w_{Am} \sin(\omega_m t + \epsilon_m). \tag{7.21}$$

A relative position can be found by taking the integral of the relative velocity.

$$\eta_r(t) = \int_0^t u_{rel} dt. \tag{7.22}$$

w_{Am} is the vertical velocity amplitude component at the water depth that is evaluated. Then the relative KC number for the half cycle becomes

$$KC_{ri} = 2\pi \frac{\eta_{rai}}{D}. \tag{7.23}$$

and the relative oscillation frequency is

$$\omega_{ri} = \frac{2\pi}{T_{ri}}. \tag{7.24}$$

This is the same as we did in Section 4.2, but instead of using η and T we now use η_r and T_r.

If the water is oscillating, as in waves, the Froude-Krylov force must be added. This is because of the pressure gradient that is present in an accelerating fluid. If we assume that all wave components in Equation 7.21 are long relative to the plate width, we can assume an uniform acceleration field. The Froude-Krylov force simplifies to

$$F_{fk} = \rho V \dot{w}. \tag{7.25}$$

V is the volume of the solid members of the perforated plate, and ρ is the density of the fluid. The pressure gradient due to the accelerating fluid is only dependent on the fluid acceleration. The total force for the relative half-cycle "i" becomes

$$F_i(t) = -C_A(KC_{ri}) A_0 \dot{u}_{rel} - C_B(KC_{rj}) \omega_{ri} A_0 u_{rel} + \rho V \dot{w}. \tag{7.26}$$

Note that C_A and C_B are functions of the KC number and taken from the curves from the regular tests. Equation 7.26 is based on equation 9.43 in the book "Sea Loads on Ship and Offshore Structures" (Faltinsen, 1990) but modified with KC dependent hydrodynamic coefficients. The hydrodynamic coefficients can be taken from the semi-analytic method of Mentzoni and Kristiansen (2019) or from experiments with regular forced oscillations. The subscript "i" refers to the present half-cycle, and the subscript j varies as $j = i$ if $KC_{ri} > KC_{r(i-1)}$ and $j = i - 1$ if $KC_{ri} < KC_{r(i-1)}$. This method of choosing KC numbers for the hydrodynamic coefficients is discussed in Section 7.1.3, and time series showed that this way of choosing the hydrodynamic coefficients was good in the case of no waves.

Equation 7.26 is a simplification of the effects of waves in combination with forced oscillations. In waves, there is also a horizontal velocity component that affects the vertical forces on the plate. Mentzoni and Kristiansen (2020) did experiments on perforated plates in waves. They also did CFD calculations in orbital flow and in a numerical wave tank. They found that in orbital flow, and in waves, there are created unsymmetrical plate-end vortices. This asymmetry reduced the forces on the plate in the vertical direction. One can argue by this that Equation 7.26 yields conservative results. However, numerical calculations or experiments must be performed in order to confirm Equation 7.26 yields conservative results when waves and oscillations are present.

What is meant by "far from the free surface and seafloor " can be discussed. In the present experiments, the plate was positioned 1.39D under the free surface, and 1.39D above the tank floor. For the KC range that was tested in the experiments of this thesis, this submergence is sufficient to avoid most of the free surface interaction. For a 7.5-meter wide hatch cover plate, this corresponds to 10.4 meters under the free surface. Vottestad (2020) studied perforated plates close to the free surface. She did experiments in waves, and experiments were the plate was forced to oscillate in heave. She found that that added mass decreased and goes towards zero and even negative values when the plate is forced to oscillate close to the free surface. The KC numbers were chosen such that water exit and entry were avoided. The total damping increased when the plate was closer to the free surface (viscous and wave radiation). Since the forces are changed close to the free surface, further research is needed to find simple methods of estimating the hydrodynamic coefficients, when the plate oscillates close to the free surface.

The semi-analytical method by Mentzoni and Kristiansen (2019) could be used if the forces are damping dominated. If we are in the inertia dominated region, one should be careful with the added mass coefficient from the semi-analytical method if the perforated plate has some thickness, because the method is based on thin perforated plates.

In a real marine lifting operation, the flow is allowed to separate from all corners. Mentzoni and Kristiansen (2019) compared results from 2D CFD simulations with results from An and Faltinsen (2013), which used a 3D setup were the flow was allowed to separate from all four edges of the perforated plate. The damping was predicted higher in the 2D simulations than for the 3D experiments, and they differ by approximately 10-15%. The added mass was close for $KC<1$ for both tested perforation ratios (τ=0.08 and τ=0.16). More research is needed in this area, but this suggests that coefficients from simplified 2D simulations give reasonable estimates for the forces in real marine lifting operations as well.

8 Concluding Remarks and Further Research

8.1 Regular Forced Oscillations

Experiments for regular forced oscillations were done to establish KC dependent curves for the added mass and damping for two perforated structures. The structures were screens consisting of square cylinders. The models are named S19 and S28, with perforation ratio 0.19 and 0.28, respectively. A laminar 2D viscous flow solver developed by Mentzoni (2020) was used to validate the lab results for the screen with the highest perforation ratio. The numerical and experimental results agreed well. This strengthens the validity of the present lab results. Some period dependence on the added mass was seen. The free surface of the water and the lab setup were pointed out as possible explanations for this. However, the dependence of the period was small compared to the dependence of the KC number, and the conclusion is that both the added mass and damping showed negligible period dependence. However, there was a strong KC dependence on the added mass and the damping, which agrees well with previous results by Mentzoni (2020) and Molin (2011). The third-harmonic force was also studied to see if the Morrison load model with a quadratic damping term was appropriate for perforated plates. It was found that in the KC range of 0.2 and 3, the Morrison load model should not be used uncritically. For small KC numbers, a larger part of the third-harmonics was in phase with the acceleration than with the velocity, especially for the model with the highest perforation. Since the third harmonics have a small contribution of the force impulse compared to the first harmonics, the Morrison load model was not used to calculate the forces in this thesis.

The semi-analytical method by Mentzoni and Kristiansen (2019) for perforated plates was compared to the present experiments, and there was found good agreement for the damping for the highest perforation ratio for the KC range of 0.2 to 3. The damping was predicted well for the lowest perforation ratio for KC numbers between 0.2 and 2. The added mass was underestimated by the semi-analytical method for both models, but the relative difference decreased as the KC number is increasing. It was pointed out that the semi-analytical method was developed for thin perforated plates, while in the experiments conducted in conjunction with this thesis, models with larger thickness are used. However, the semi-analytical method provides coefficients that calculate the force time-series well when the forces are damping dominated when $KC < 3$ for S28 and $KC < 2$ for S19.

8.2 Bi-Chromatic Motions

Several bi-chromatic tests were done to provide data for the irregular tests. There was a strong dependency on the KC number from the previous half-cycle, together with the KC number from the present half-cycle for the damping. The damping was larger if the previous half-cycle had a larger amplitude than the present. The damping was smaller if the previous half-cycle had a smaller amplitude than the present.

There was not found any particular pattern for the added mass, but the coefficient was

distributed lower or close to the curve for the regular test. An increase in the added mass compared to the regular steady-state oscillations was found in start-up situations, with an increase in the added mass of 25 %. CFD calculations showed the same trend. This was identified as a start-up phenomenon and was also reported by Ikeda et al. (1988) for solid plates. For $KC > 11$, they found an increase in the added mass of up to 75 % when the plate was forced to oscillate from rest, compared to regular steady-state forced oscillations. In our experiments, the increase in added mass occurs for all tested KC numbers. CFD was also done for a solid plate at $KC = 0.78$ in the bi-chromatic motion where the start-up situation occurred. The increase in added mass was only 5 % compared to the added mass for regular steady-state forced oscillations for $KC = 0.78$ for a solid plate. Thus, this increase in the added mass in a start-up situation is more important for a perforated plate than for a solid plate for $KC < 3$. However, the damping is smaller in a start-up situation compared to regular steady-state forced oscillations, which results in equal or smaller force amplitudes for the start-up situation compared to regular steady-state forced oscillations. For problems were the force amplitude is the important parameter, as in marine lifting operations, the start-up phenomenon is negligible for all tested KC numbers for both models.

8.3 Irregular Motions

The data from the bi-chromatic motions were used to calculate the forces from time series with irregular motions generated by a Pierson-Moskowitz spectrum. There was close agreement between the calculated forces and the measured forces from the experiments. This confirms that bi-chromatic tests are appropriate to provide hydrodynamic coefficients for irregular time series.

Since the damping coefficient depends on the KC number of the present and the previous half-cycle, a simple rule is proposed to use together with the hydrodynamic coefficients provided by the semi-analytical method by Mentzoni and Kristiansen (2019) in order to calculate the time-series. The rules for the damping are:

- Use the KC number from the previous half-cycle if the KC number of the present is smaller than the previous half-cycle.
- Use the KC number from the present half-cycle if the KC number of the present is larger than the previous half-cycle.

The added mass was found by only considering the KC number of the present half-cycle. The calculated forces are in close agreement with the measured, as long the largest KC numbers in the time series is in the damping dominated regime. When the coefficients are based on the semi-analytical method, the forces are underestimated if the largest KC numbers are in the range where the damping and inertia terms are close in magnitude. This is because the semi-analytical method underestimates the added mass. After all, the semi-analytical method is based on thin plates, while in this thesis, hydrodynamic loads on thicker plates are investigated. Since the calculations based on the semi-analytical method yielded results close to the experiments, Equation 9.43 in the book "Sea Loads

on Ships and Offshore Structures" by Faltinsen (1990) is modified with KC dependent added mass and damping when the forces are damping dominated. However, this equation should be tested with experiments, as we do not know well how the waves interact with plate motions.

8.4 Further Research

The interaction effects of an oscillating perforated plate in waves is a subject of further research. The discussed equation of Faltinsen (1990) with KC dependent coefficients and a perforated plate with regular heave motions and in regular waves could be used as a start for further investigations.

More research on perforated plates where the flow is allowed to separate from all edges would be preferable, i.e. a 3D experimental setup, as this is the case for a real marine operation. Scaling effects for structures in oscillating flows is an area of further research, as the effect of turbulence in the returning wake may influence the structure's forces. It is not recommended to do more research on irregular motions, as the crucial parameters used to predict the forces in a time-series come from the hydrodynamic coefficients in regular steady-state forced oscillations. Thus, further research should focus on finding simple methods for finding KC dependent hydrodynamic coefficients, as the semi-analytical method by Mentzoni and Kristiansen (2019). More research would be favorable to expand the semi-analytical method to be valid also for thicker perforated plates, especially regarding the added mass.

9 Bibliography

An, S. and Faltinsen, O. M. (May 1, 2013). An experimental and numerical study of heave added mass and damping of horizontally submerged and perforated rectangular plates. In: *Journal of Fluids and Structures,* 39, pp. 87–101. ISSN: 0889-9746. DOI: 10.1016/j.jfluidstructs.2013.03.004.

Chorin, A. J. (1968). Numerical solution of the Navier-Stokes equations. In: *Mathematics of Computation,* 22.104, pp. 745–762. ISSN: 0025-5718, 1088-6842. DOI: 10.1090/S0025-5718-1968-0242392-2.

DNV-GL (2017). DNV-RP-H103: Modelling and Analysis of Marine Operations.

Faltinsen, O. M. (1990). Sea Loads on Ships and Offshore Structures. Cambridge: Cambridge University Press.

Graham, J. M. R. (Mar. 1980). The forces on sharp-edged cylinders in oscillatory flow at low Keulegan–Carpenter numbers. In: *Journal of Fluid Mechanics,* 97.2. Publisher: Cambridge University Press, pp. 331–346. ISSN: 1469-7645, 0022-1120. DOI: 10.1017/S0022112080002595.

Ikeda, Y., Osa, K., and Tanaka, N. (May 1, 1988). Viscous Forces Acting on Irregularly Oscillating Circular Cylinders and Flat Plates. In: *Journal of Offshore Mechanics and Arctic Engineering,* 110.2. Publisher: American Society of Mechanical Engineers Digital Collection, pp. 140–147. ISSN: 0892-7219. DOI: 10.1115/1.3257042.

Keulegan, G. H. and Carpenter, L. H. (1958). Forces on cylinders and plates in an oscillating fluid. In: *Journal of Research of the National Bureau of Standards,* 60.5. Publisher: Department of Commerce, National Bureau of Standards, pp. 423–440.

Kristiansen, T. and Faltinsen, O. M. (Feb. 1, 2008). Application of a vortex tracking method to the piston-like behaviour in a semi-entrained vertical gap. In: *Applied Ocean Research,* 30.1, pp. 1–16. ISSN: 0141-1187. DOI: 10.1016/j.apor.2008.02.003.

Mentzoni, F. (2020). *Hydrodynamic Loads on Complex Structures in the Wave Zone.* Accepted: 2020-05-08T11:05:57Z ISSN: 1503-8181. URL: https://ntnuopen.ntnu.no/ntnu-xmlui/handle/11250/2653724 (visited on 07/18/2020).

Mentzoni, F., Abrahamsen-Prsic, M., and Kristiansen, T. (Sept. 25, 2018). Hydrodynamic Coefficients of Simplified Subsea Structures. In: ASME 2018 37th International Conference on Ocean, Offshore and Arctic Engineering. American Society of Mechanical Engineers Digital Collection. DOI: 10.1115/OMAE2018-78315.

Mentzoni, F. and Kristiansen, T. (June 2019a). A Semi-Analytical Method for Calculating the Hydrodynamic Force on Perforated Plates in Oscillating Flow. In: DOI: 10.1115/OMAE2019-95093.

Mentzoni, F. and Kristiansen, T. (Mar. 1, 2019b). Numerical modeling of perforated plates in oscillating flow. In: *Applied Ocean Research,* 84, pp. 1–11. ISSN: 0141-1187. DOI: 10.1016/j.apor.2018.12.016.

Mentzoni, F. and Kristiansen, T. (Apr. 1, 2020). Two-dimensional experimental and numerical investigations of perforated plates in oscillating flow, orbital flow and incident waves. In: *Applied Ocean Research,* 97, p. 102078. ISSN: 0141-1187. DOI: 10.1016/j.apor.2020.102078.

Molin, B. (Feb. 1, 2011). Hydrodynamic modeling of perforated structures. In: *Applied Ocean Research,* 33, pp. 1–11. DOI: 10.1016/j.apor.2010.11.003.

Morison, J. R., Johnson, J. W., and Schaaf, S. A. (May 1, 1950). The Force Exerted by Surface Waves on Piles. In: *Journal of Petroleum Technology,* 2.5. Publisher: Society of Petroleum Engineers, pp. 149–154. ISSN: 0149-2136. DOI: 10.2118/950149-G.

Newman, J. N. (1977). Marine Hydrodynamics. Cambridge: MIT Press. ISBN: 978-0-262-14026-3.

Pullin, D. I. (Oct. 1978). The large-scale structure of unsteady self-similar rolled-up vortex sheets. In: *Journal of Fluid Mechanics,* 88.3. Publisher: Cambridge University Press, pp. 401–430. ISSN: 1469-7645, 0022-1120. DOI: 10.1017/S0022112078002189.

Sandvik, P. C., Solaas, F., and Nielsen, F. G. (Jan. 1, 2006). Hydrodynamic Forces On Ventilated Structures. In: The Sixteenth International Offshore and Polar Engineering Conference. International Society of Offshore and Polar Engineers.

Sarpkaya, T. (Jan. 1, 1976a). In - Line And Transverse Forces, On Cylinders In Oscillatory Flow At High Reynolds Numbers. In: Offshore Technology Conference. Offshore Technology Conference. ISBN: 978-1-55563-589-3. DOI: 10.4043/2533-MS.

Sarpkaya, T. (Feb. 2, 1976b). Vortex Shedding and Resistance in Harmonic Flow about Smooth and Rough Circular Cylinders at High Reynolds Numbers. Section: Technical Reports. NAVAL POSTGRADUATE SCHOOL MONTEREY CA.

Singh, S. (1979). Forces on bodies in oscillatory flow. Ph.D. thesis University of London.

Tennekes, H. and Lumley, J. L. (1972). A First Course in Turbulence. The MIT Press. ISBN: 9780262200196.

Vottestad, K. (2020). Experimental Study of Hydrodynamic Loads on Ventilated Plates Near the Free Surface. Master thesis. Norwegian University of Science and Technology.

A Bi-Chromatic Motions

This appendix shows the time series for the bi-chromatic motions that was tested. More data can be found in Table 3.2. The names of the series is given in the title of each plot, and corresponds to the names in Table 3.2. η is the position and X_0 is defined by Equation 3.2.

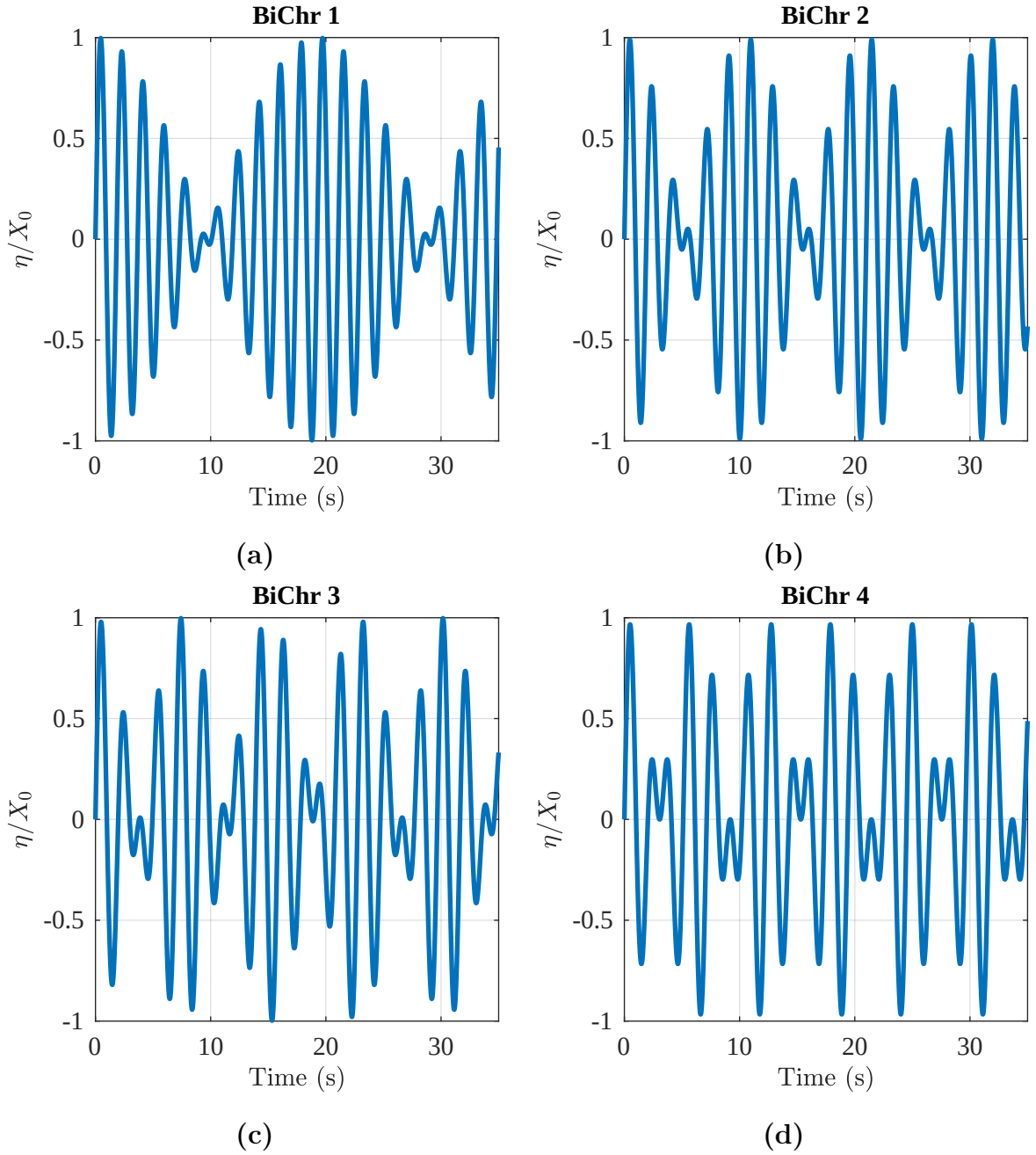

Figure A.1

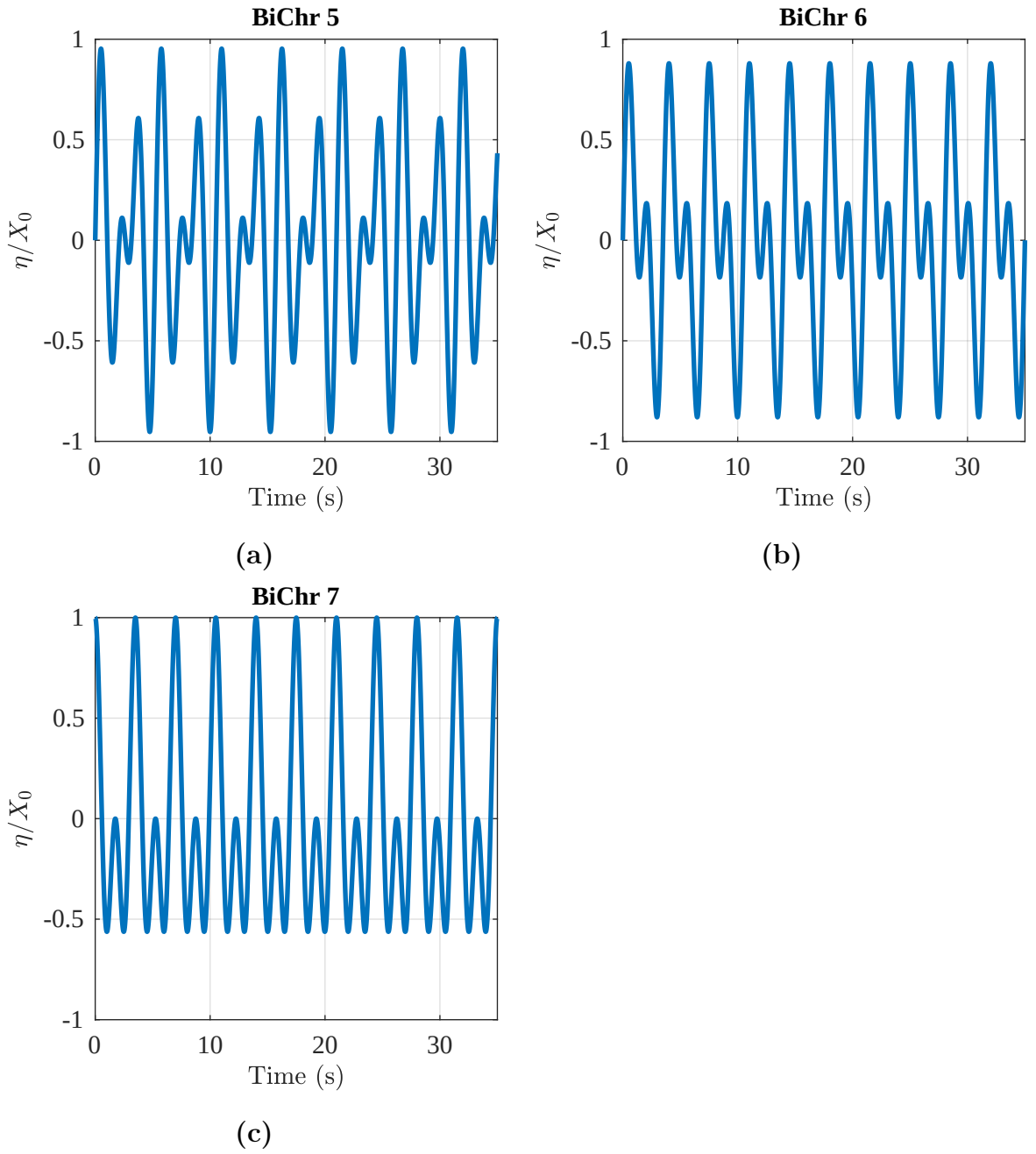

(a) **(b)**

(c)

Figure A.2

B Full Size Figures of Normalized Force Amplitude

In this appendix larger figures of Figure 6.11 (a) and (b) is presented. This appendix is included to show that the yellow star markers (BiChr 7), which is identified as a start up situation, are close to the regular curve, even though the added mass is larger for this particular half cycle. This is because the damping is correspondingly smaller. The legend for these figures is found in Figure 6.8.

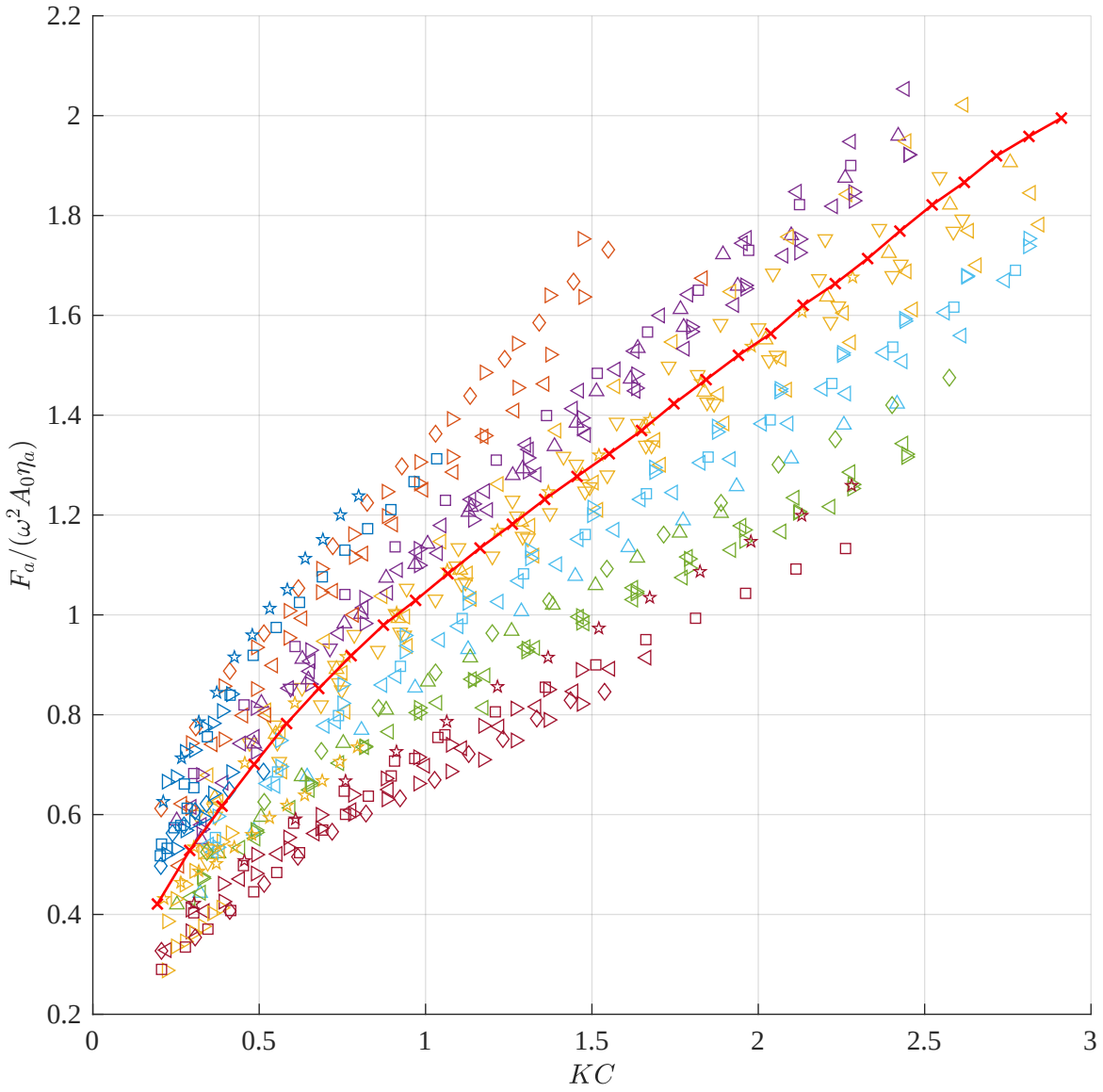

Figure B.1: Normalized force amplitude coefficients for S19.

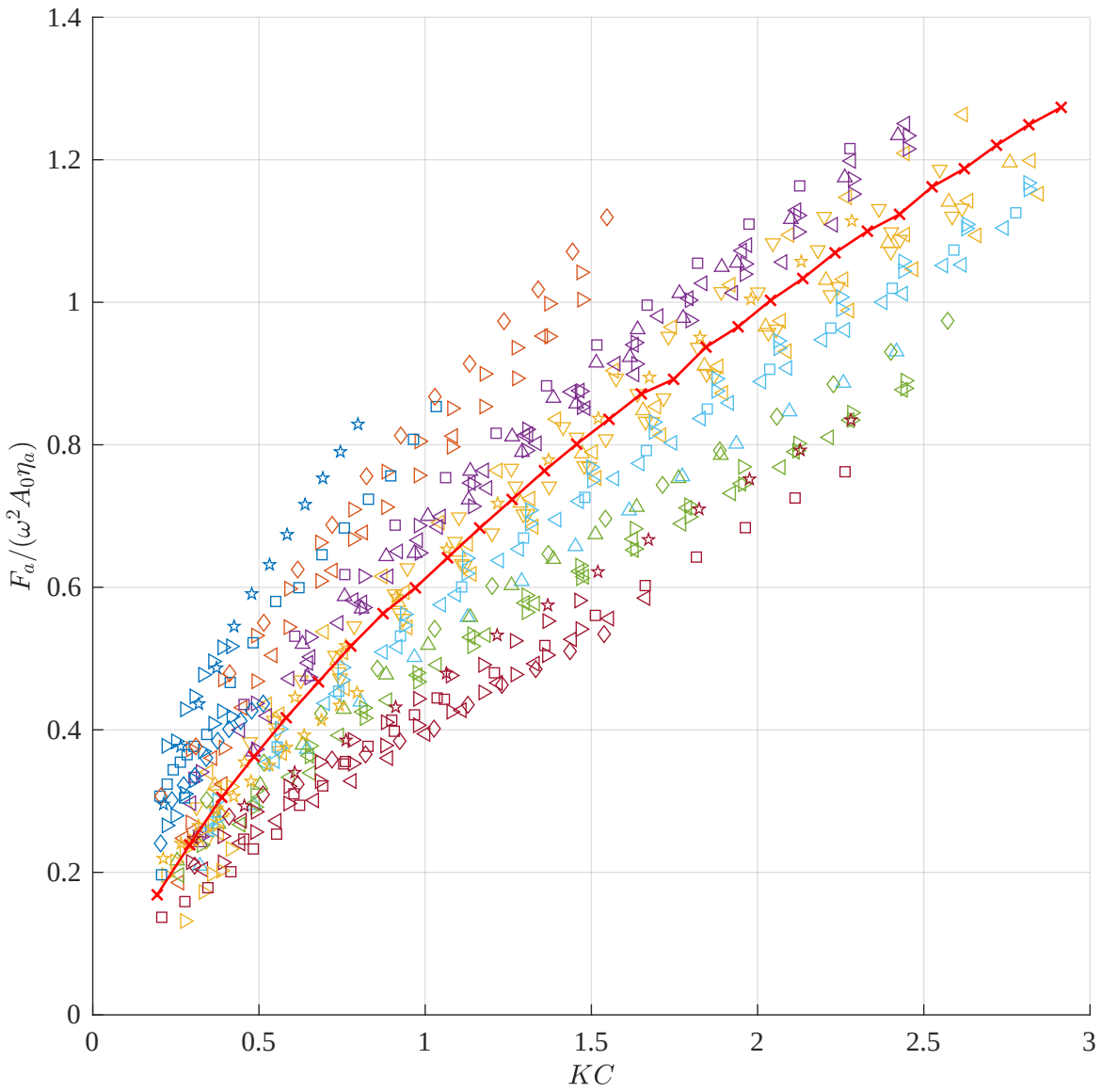

Figure B.2: Normalized force amplitude coefficients for S28.

Jon Kristian Voster

Hydrodynamic Loads on Perforated Plates Subjected to Irregular Forced Oscillations

NTNU
Norwegian University of
Science and Technology